Abstract

Measurement of the Decays $D^0 \to \pi^-\pi^+$ and $D^0 \to K^-K^+$

William Robert Ross
Yale University
1992

Using data from Fermilab photoproduction experiment E691, the ratio of branching fractions between the Cabibbo-suppressed modes $B(D^0 \to K^-K^+)/B(D^0 \to \pi^-\pi^+)$ is measured to be $1.95 \pm 0.34 \pm 0.22$. Branching fractions for the modes $D^0 \to K^-K^+$ and $D^0 \to \pi^-\pi^+$ relative to the Cabibbo-allowed decay $D^0 \to K^-\pi^+$ are also determined. Furthermore, an upper limit of 0.45 at the 90% C.L. on the CP violating asymmetry in $D^0 \to K^-K^+$ versus $\overline{D^0} \to K^-K^+$ decays is determined.

Measurement of the Decays $D^0 \to \pi^-\pi^+$ and $D^0 \to K^-K^+$

A Dissertation
Presented to the Faculty of the Graduate School
of
Yale University
in Candidacy for the Degree of
Doctor of Philosophy

by
William Robert Ross
June, 1992

The E691 Collaboration

J.C. Anjos,[3] J.A. Appel,[6] A. Bean,[1] S.B. Bracker,[11]
T.E. Browder,[1] L.M. Cremaldi,[7] J.E. Duboscq,[1] J.R. Elliott,[5]
C.O. Escobar,[10] M.C. Gibney,[5] G.F. Hartner,[11] P.E. Karchin,[12]
B.R. Kumar,[11] M.J. Losty,[8] G.J. Luste,[11] P.M. Mantsch,[6]
J.F. Martin,[11] S. McHugh,[1] S.R. Menary,[11] R.J. Morrison,[1]
T. Nash,[6] J. Pinfold,[2] G. Punkar,[1] M.V. Purohit,[9]
W.R. Ross,[12] A.F.S. Santoro,[3] A.L. Shoup,[4] K. Sliwa,[6]
M.D. Sokoloff,[4] M.H.G. Souza,[3] W.J. Spalding,[6] M.E. Streetman,[6]
A.B. Stundžia,[11] M.S. Witherell[1]

[1]University of California, Santa Barbara, California, 93106
[2]Carleton University, Ottawa, Ontario, Canada K1S5B6
[3]Centro Brasileiro de Pesquisas Fisicas, Rio de Janeiro, Brazil
[4]University of Cincinnati, Cincinnati, Ohio, 45221
[5]University of Colorado, Boulder, Colorado, 80309
[6]Fermi National Accelerator Laboratory, Batavia, Illinois, 60510
[7]University of Mississippi, Oxford, Mississippi, 38677
[8]National Research Council, Ottawa, Ontario, Canada K1A0R6
[9]Princeton University, Princeton, New Jersey, 08544
[10]Universidade de São Paulo, São Paulo, Brazil
[11]University of Toronto, Toronto, Ontario, Canada M5S1A7
[12]Yale University, New Haven, Connecticut, 06511

Acknowledgements

My experience in graduate school here at Yale was molded and influenced by a variety of people, most of which have preceded me in obtaining a degree. I would like to thank that select group of people who managed to put up with me for a few years: Robert Topper, Chris Darling & co, Karen Ohl, ZhongXin Wu, Melissa Hui & Orsola Russello, without whom the last few years would have been significantly less "enjoyable".

Academically, I was privileged in being able to interact with some of the best that this field has to offer, both at Yale and at Fermilab. First and foremost, let me thank Paul Karchin for showing me exactly what it means to be a professional physicist. Just about everybody from E691 and E769, but in particular Lee Lueking and Steve Takach (& co.), were a pleasure to work and play with, as was Professor Edward McCliment at the FNAL test beam.

The list of people who helped me, made me smile (or sometimes think) goes on and on, but a few are the following: the secretaries on the 5^{th} floor of Gibbs, Jean Belfonti, Sara Batter, Abhay Deshpande, Ram Ben-David & co, Jeff Snyder, Frank Rotondo, Clark Landis, Elliott "Piyar" Wolin, Barbara Karchin, Jon & Jen, Rikki Abzug, Ricardo, Dick Majka and John Sinnott. Special credit goes to my friends from the Lyçée, Philippe Rapaccioli, Ricardo Ortiz, André Castaybert & Mauro Gabriele, and from Cornell, chiefly Eric Ren and Christopher Nantista. Special thanks to Dave Kaplan for many fruitful discussions.

Thanks to my family, for providing the love and attention it took to get this far, and to Peter Martin, for putting it all together.

Contents

1 Theoretical Considerations **5**

1.1 Charm Decays 5

1.1.1 The Effective Hamiltonian 11

1.1.2 Final State Interactions 15

1.2 CP Violation in the D^0-$\overline{D^0}$ system 17

1.2.1 D^0-$\overline{D^0}$ mixing 17

1.2.2 Direct CP violation in D^0 decays 26

1.3 Charm Production and Detection 29

1.3.1 Charm Photoproduction 30

1.3.2 Experiment E691 at Fermilab 30

2 Apparatus **33**

2.1 The Tevatron 33

2.2 The Beam Line 35

2.3 The Tagged Photon Spectrometer 37

2.3.1 The Target 37

2.3.2 The Silicon Microstrip Detector 37

2.3.3 The Drift Chambers 42

2.3.4 The Magnets 45

2.3.5 The Čerenkov Counters 46

2.3.6 Electron Calorimetry 52

2.3.7 Hadronic Calorimetry 55

2.3.8 Muon Detection 57

2.3.9 The Triggers 57
2.3.10 The Data Acquisition and Monitoring Systems 60

3 Reconstruction **63**
3.1 Hardware 63
3.2 Software 64
3.2.1 Pass 1 64
3.2.2 Pass 2 66
3.2.3 Data Summary Tapes 71

4 Analysis and Results **73**
4.1 Definitions of Fundamental Physical Parameters 73
4.2 The Monte Carlo 77
4.3 The Vertex Strip 79
4.4 Analysis Cuts and Sub-Strips 79
4.4.1 All Combination Event Selection 79
4.4.2 Higher Level Analysis Cuts 80
4.5 Efficiencies 90
4.5.1 Geometrical Acceptance and Reconstruction Efficiencies . . 90
4.5.2 Čerenkov Efficiencies 96
4.6 Analysis for Relative Branching Fractions 111
4.6.1 $D^0 \rightarrow \pi^-\pi^+$ Analysis 111
4.6.2 $D^0 \rightarrow K^-K^+$ Analysis 121
4.6.3 $D^0 \rightarrow K^-\pi^+$ analysis 122
4.7 Results on Branching Ratio Fractions 125
4.7.1 Study of Systematic Effects 125
4.7.2 Ratios of Branching Fractions 127

4.8 Analysis for CP violation study 128
4.8.1 The D^* Cut 129
4.8.2 Mass and Lifetime analysis: a_{KK} 131
4.8.3 Time-Integrated Asymmetry: A' 137

5 Conclusions **138**
5.1 Comments on Branching Fraction Ratios 138
5.2 Comments on CP Violation 139

A Decay Rate Calculations **140**

Bibliography **144**

List of Figures

1.1	Feynman diagrams for Single Quark Decay	7
1.2	Feynman diagrams for W-exchange and Annihilation	8
1.3	Spacelike and Timelike Penguin Diagrams	9
1.4	Box diagrams contributing to $D^0 - \overline{D^0}$ mixing	24
1.5	Intermediate state (long distance) contribution to $D^0 - \overline{D^0}$ mixing	25
1.6	First order Feynman Diagram for Photon-Gluon Fusion	32
2.1	Fermilab Accelerators and Beamlines	34
2.2	Diagram of P-east beamline	35
2.3	Distribution of γ energies in E691 beam	36
2.4	The Tagged Photon Spectrometer	38
2.5	Diagram of the Silicon Microstrip Detector	41
2.6	Cutaway of a drift chamber and wire setup	44
2.7	Photon production for C1 and C2	49
2.8	C1 and C2 Čerenkov counters	51
2.9	Cutaway view of the SLIC and layering diagram	54
2.10	Cutaway view of the Hadrometer	56
2.11	Logic diagrams for the $TAGH$ and E_t triggers	59
2.12	Logical Organization of the E691 DA System	61
2.13	Logical Organization of the E691 Online Monitoring System	62
3.1	Track reconstruction regions at TPL	66
3.2	Vertices in a charm event	72
4.1	Illustration of Significance of Detachment in Z (SDZ)	75
4.2	Illustration of Distance of Impact Parameter (DIP)	76
4.3	Illustration of Ratio	77
4.4	Invariant Mass distribution for $D^0 \to \pi^-\pi^+$ + C.C. for all two-track combinations from events in vertex strip	82
4.5	Invariant Mass distribution for $D^0 \to K^-K^+$ + C.C.	83
4.6	Invariant Mass distribution for $D^0 \to K^-\pi^+$ + C.C.	84
4.7	Čerenkov probability distributions for pions	85

4.8	Čerenkov probability distribution for kaons	86
4.9	θ for pions in 1000 $D^0 \rightarrow \pi^-\pi^+$ + C.C. MC decays	90
4.10	θ for kaons in 1000 $D^0 \rightarrow K^-K^+$ + C.C. MC decays	91
4.11	Comparison of Čerenkov ϵ for pions between MC and real data	97
4.12	Comparison of Čerenkov ϵ for kaons between MC and real data	98
4.13	$D^0 \rightarrow K^-\pi^+$ + C.C. mass distribution for $56 \leq p(D^0) \leq 66$ GeV/c	102
4.14	True P distribution for D^0 particles from $D^0 \rightarrow K^-\pi^+$ data	103
4.15	Ratios between $D^0 \rightarrow K^-\pi^+$ + C.C. and MC populations	104
4.16	Illustration of $cos(\theta)$ in the CMS	107
4.17	$cos(\theta)$ distribution for $D^0 \rightarrow K^-\pi^+$ + C.C. events	108
4.18	$cos(\theta)$ distribution for MC $D^0 \rightarrow K^-\pi^+$ + C.C. events	109
4.19	$D^0 \rightarrow \pi^-\pi^+$ + C.C. mass distribution	113
4.20	$D^0 \rightarrow K^-K^+$ + C.C. mass distribution	114
4.21	$D^0 \rightarrow K^-\pi^+$ + C.C. analyzed as $D^0 \rightarrow \pi^-\pi^+$ decays from 18,000 MC events	115
4.22	$D^0 \rightarrow \pi^-\pi^+$ + C.C. mass distribution from 18,000 MC events	116
4.23	$D^0 \rightarrow K^-\pi^+\pi^0$ + C.C. analyzed as $D^0 \rightarrow \pi^-\pi^+$ decays from 18,000 MC events	118
4.24	$D^0 \rightarrow K^-\pi^+\pi^0\pi^0$ + C.C. analyzed as $D^0 \rightarrow \pi^-\pi^+$ decays from 18,000 MC events	119
4.25	$D^0 \rightarrow K^-\pi^+$ + C.C. analyzed as $D^0 \rightarrow K^-K^+$ decays from 18,000 MC events	122
4.26	$D^0 \rightarrow K^-\pi^+$ + C.C. mass distribution	123
4.27	$\Delta m = m_D - m(D,\pi)$ distribution	129
4.28	$D^0 \rightarrow K^-K^+$ invariant mass distribution at SDZ ≥ 5.0	131
4.29	$\overline{D^0} \rightarrow K^-K^+$ invariant mass distribution at SDZ ≥ 5.0	132
4.30	$D^0 \rightarrow K^-K^+$ lifetime distribution for $(m_D - 1.865) \leq 28.8\, MeV/c^2$	133
4.31	$\overline{D^0} \rightarrow K^-K^+$ lifetime distribution for $(m_D - 1.865) \leq 28.8\, MeV/c^2$	134
4.32	$\overline{D^0} \rightarrow K^-K^+$ lifetime distribution. There are 10 curves plotted for a_{KK} ranging from 0.0 to 2.0.	135

List of Tables

1.1	Characteristics of the three "charmed" mesons	6
1.2	BSW Theoretical Branching Fraction predictions	16
1.3	Amplitudes for three D^0 decay modes	27
2.1	Parameters of the E691 silicon microstrip system	39
2.2	Parameters of the E691 drift chamber system	42
2.3	Parameters of the E691 magnets	45
2.4	Parameters of the E691 Čerenkov counters	48
2.5	Parameters of the SLIC	53
2.6	Parameters of the Hadrometer	55
4.1	MC data tapes used in the geometrical efficiency study	93
4.2	Comparison of Basic event parameters for MC tapes used	93
4.3	Reconstruction effciencies and acceptances for $D^0 \to \pi^-\pi^+$, $D^0 \to K^-K^+$ and $D^0 \to K^-\pi^+$	94
4.4	Čerenkov efficiencies for various momenta for π and K	96
4.5	Ratios for given p ranges between $D^0 \to K^-\pi^+$ data and MC populations	101
4.6	Momentum "cells" used in weighted efficiency calculation	106
4.7	Effect of different background parametrizations on $D^0 \to \pi^-\pi^+$ signal strength	125
5.1	Comparison of ratios of branching fractions	137

Chapter 1 Theoretical Considerations

The branch of physics dealing with elementary particles possesses a theoretical framework known as the Standard Model. This edifice, having as its foundation the product of gauge groups $SU(3)_c \otimes SU(2)_L \otimes U(1)$, has been successful in predicting and describing many experimentally observed strong and weak interaction phenomenon.

1.1 Charm Decays

$SU(2) \otimes U(1)$ and the Weak Hamiltonian

If one considers the minimal $SU(2)_L \otimes U(1)$ electroweak model formulated by Weinberg, Salaam and Glashow, then all short-distance interactions are mediated by charged currents (a review of this is found in [1]), the gauge bosons being the $W^{\pm}$. Under the assumption that the W mass is greater than all quark and lepton masses, and within the standard model of three lepton and quark families, these interactions are described by the following Weak Hamiltonian:

$$H_W = (G_F/\sqrt{2})(J^{\mu}_{+} J_{-\mu} + J^{\mu\dagger}_{-} J^{\dagger}_{+\mu})$$

where the current

$$J^{\mu}_{-} = (\overline{u}\ \overline{c}\ \overline{t})\gamma^{\mu}(1-\gamma_5)V \begin{pmatrix} d \\ s \\ b \end{pmatrix} + (\overline{\nu}_e\ \overline{\nu}_{\mu}\ \overline{\nu}_{\tau})\gamma^{\mu}(1-\gamma_5) \begin{pmatrix} e^- \\ \mu^- \\ \tau^- \end{pmatrix}$$

represents the left-handed components of quarks and leptons, and

$$J^{\mu}_{+} = (J^{\mu}_{-})^{\dagger}$$

is the hermitian conjugate current.

In the above, note that the $-\frac{1}{3}$ quark mass eigenstates are related to the weak eigenstates by the Cabibbo-Kobayashi-Maskawa matrix V. The Hamiltonian describes weak interactions to first order. Strong corrections, as will be shown below, alter the form of H. These include gluon radiative corrections to purely weak diagrams, and the whole class of "penguin" diagrams.

Charmed Mesons and their Decay

There are three "charmed" $J = 0$ mesons possible within the framework of the standard model. By "charmed" is meant that the heaviest valence quark is a c or $\bar{c}$. These are the charged D^+ (D^-), neutral D^0 ($\overline{D^0}$) and strange D_s^+ ($\overline{D_s^-}$) mesons. The quark content of these mesons, as well as isospin, spin-parity, mass and lifetime, are shown in the following table [2]:

Meson	Quark Content	$I(J^P)$	Mass (GeV/c^2)	τ (10^{-13} sec)
D^+	$c\bar{d}$	$1/2(0^-)$	1.8694 ± 0.0005	10.62 ± 0.28
D^0	$c\bar{u}$	$1/2(0^-)$	1.8645 ± 0.0010	4.21 ± 0.10
D_s^+	$c\bar{s}$	$0(0^-)$	1.9691 ± 0.0012	4.45 ± 0.3

Table 1.1: Characteristics of the three "charmed" mesons.

In addition, there exist three corresponding vector mesons: D^{*0}, D^{*+} and D_s^{*+} (all with appropriate antiparticles). The spin-1 particles have a slightly higher mass than the pseudoscalars, due in part to spin-spin interactions, and can decay strongly (i.e. $D^{*+} \rightarrow D^0\pi^+$) into spin-0 mesons. The pseudoscalar mesons decay weakly into two-body final states in several ways, illustrated in Figures 1.1 to 1.3.

Six Feynman diagrams describe these decays. These are quark decay (both external and internal spectator mechanisms, types A and B), W-exchange (type C), quark annihilation (type D), and spacelike and timelike penguin diagrams (types E and F). Note that the leading order QCD corrections are not shown in Figures 1.1-1.3.

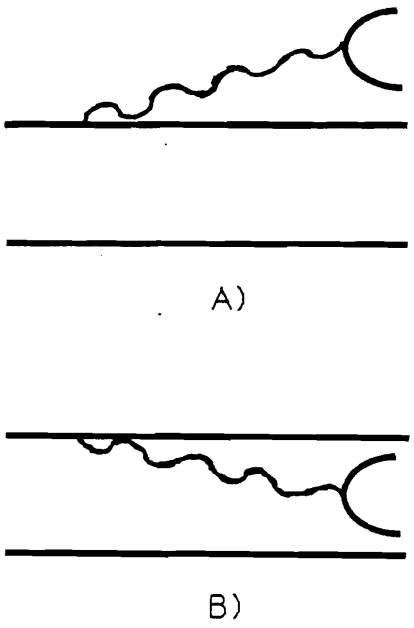

Figure 1.1: Feynman diagrams for Single Quark Decay: A) External and B) Internal Spectator Diagrams.

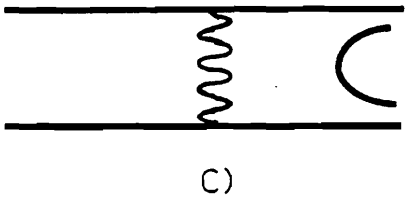

C)

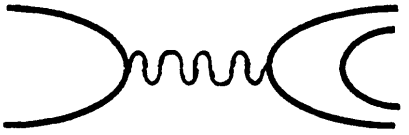

D)

Figure 1.2: Feynman diagrams for C) W-exchange and D) Annihilation.

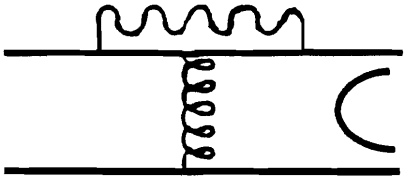

E)

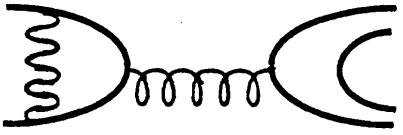

F)

Figure 1.3: E) Spacelike and F) Timelike Penguin Diagrams.

Only charged mesons can decay via $q - \overline{q}$ annihilation. Of the other decay schemes mentioned above, quark decay into a $W - q$ pair (specifically external W emission) is expected to be the dominant mechanism for heavy quarks. Internal W-emission can naïvely be expected to be suppressed because one of the internally produced quarks has to be of the same color as the spectator, while the other internal quark has to color-match the daughter from charm decay. This results in a suppression factor of 1/9. However, soft gluon exchange between the internal quarks lessens this effect, by enabling a suitable color rearrangement, so that color-suppression is not important in D decays. In B decays, however, the situation is different. Given the much greater mass of the bottom quark (mass of $B^0 \sim 5$ GeV/c^2), the internally produced quarks have much higher momentum, making gluon exchange (and thus color rearrangement) less likely. Thus, color-suppression is important for bottom mesons.

Both external and internal W-emission can be Cabibbo-suppressed, however, by the fact that the W couples to weak eigenstates, which are linear combinations of mass eigenstates. As an example, consider, in the four quark model, the decay

$$c \rightarrow W^+ s'$$

where

$$s' = s \cos(\theta_C) + d \sin(\theta_C)$$

In the above, θ_C is the Cabibbo mixing angle, with $\sin(\theta_C) \sim 0.2$. Hence, the decay to an s-quark is favored relative to a decay to a d-quark by a factor of $\tan^2(\theta_C)$. This is termed Cabibbo-suppression. The W decays in a similar manner:

$$W^+ \rightarrow u\overline{d}'$$

where

$$\overline{d}' = -\overline{s} \sin(\theta_C) + \overline{d} \cos(\theta_C)$$

Here, the decay to a d-quark is favored. Applied to the allowed decay $D^0 \to K^-\pi^+$ (which proceeds mostly by external W-emission), where the D^0 is composed of a c and a $\bar{u}$, the first form of suppression described above leads to the decays $D^0 \to \pi^-\pi^+$, while the second leads to $D^0 \to K^-K^+$.

The W-exchange process is helicity-suppressed, and so is not important compared tp spectator decays. Penguin diagrams, being a first order in the strong interaction and second order in the weak, are not expected to play a significant role in charm decays. Naïvely, however, one expects that penguin diagrams will contribute slightly more to $D^0 \to \pi^-\pi^+$ decays than to the $D^0 \to K^-K^+$ channel, since gluon conversion to a $u\bar{u}$ pair is more likely to occur than to a $s\bar{s}$ pair.

1.1.1 The Effective Hamiltonian

The Hamiltonian given in section 1.1 describes only charged weak currents. Over the past decade, several phenomenological attempts to include first order strong corrections to weak interaction processes have been developed [3, 4]. In these, terms are added to the purely weak Hamiltonian in order to include effective neutral weak currents made possible by strong effects. Furthermore, the terms describing weak currents are multiplied by factors intended to take into account strong corrections.

The inclusion of strong factors in H_W leads to the formulation of a new, "effective" Hamiltonian. For non-leptonic charm decays, this effective weak Hamiltonian, neglecting penguin operators is given by [3]:

$$H_W^{eff} = (G_F/\sqrt{2}) \sum_{j,k,l} V_{cj}^* V_{kl} [c_1(\bar{k}l)(\bar{j}c) + c_2(\bar{k}c)(\bar{j}l)]$$

In the above, j, k, l are flavor indices and c_1 and c_2 are linear combinations of the QCD short-distance coefficients:

$$c_1(\mu) = \frac{1}{2}[c_+(\mu) + c_-(\mu)]$$

$$c_2(\mu) = \frac{1}{2}[c_+(\mu) - c_-(\mu)]$$

at energy μ. Note that c_1 and c_2 are defined below. The V_{ij} are elements of the CKM matrix, the pairs (c,k) and (j,l) being $+\frac{2}{3}$ and $-\frac{1}{3}$ charged quarks respectively. The quark currents are of the $V-A$ form:

$$(\overline{k}l) \equiv [\overline{k}_a \gamma_\mu (1-\gamma_5) l_a],$$

a being a color index. As can be seen, the first term in the above describes the standard charged weak current. The second term represents an effective neutral current interaction produced by short-distance QCD effects (hard gluon exchange). Note that when such effects are absent, one has $c_+ = c_- = 1$, causing the second term to disappear.

The short-distance coefficients in the leading logarithmic approximation are written as:

$$c_\pm = \left(\frac{\alpha_5(m_b^2)}{\alpha_4(\mu^2)}\right)^{-d_\pm/2b_4} \left(\frac{\alpha_6(m_t^2)}{\alpha_5(m_b^2)}\right)^{-d_\pm/2b_5} \left(\frac{\alpha_6(M_W^2)}{\alpha_6(m_t^2)}\right)^{-d_\pm/2b_6}$$

where

$$d_- = -2d_+ = 8.$$

The α_n in the above equation are the running QCD coupling constants for a theory based on n flavors:

$$\alpha_n(Q^2) = \frac{4\pi}{b_n \log(Q^2/\Lambda_n^2)}$$

$$b_n = 11 - \frac{2}{3}n$$

In the above, the Λ_n are the QCD scale parameters in the instance of n flavors. These are related in the following manner:

$$\Lambda_5 = \Lambda_4 \left(\frac{\Lambda_4}{m_b}\right)^{2/23}$$

$$\Lambda_6 = \Lambda_5 \left(\frac{\Lambda_5}{m_t}\right)^{2/21}$$

in order to insure the continuity of the α_n as n increases. As can be seen from the values of d_+ and d_-, one has:

$$c_- c_+^2 = 1.$$

Once an effective Hamiltonian has been formulated, actual calculation of the amplitudes of the processes it describes can be simplified if one or more approximation schemes are employed. Buras *et al.* [3] have limited their calculations uniquely to Feynman diagrams which are first order in the $1/N$ expansion, where N is the number of colors. Bauer, Stech and Wirbel [4, 5] have used the Factorization method in their calculations, which have predicted various branching fractions for non-leptonic modes with a high degree of success. A comparison between theoretical estimates and actual measurements can be found in [4].

The Factorization Approach

The factorization method [3, 4, 5] has been employed by Bauer, Stech and Wirbel (BSW) in order to simplify calculation of various exclusive decay amplitudes. This approximation entails expressing a matrix element as a product of simpler matrix elements of effective quark currents. In the case of external spectator diagrams, for instance, this requires neglecting gluon contributions between W-decay products and any other quark lines to first order and only determining matrix elements of long-distance quark currents, thereby reducing one process into two sub-processes.

The advantage of using this scheme lies in the fact that pre-existing form factors determined from previously calculated semi-leptonic decays may be employed in the calculation. Given that the currents are proportional to quasi-stable hadron fields, the further approximation can be made: for one current of the current product in the Hamiltonian, only the asymptotic part of the hadron field is retained.

In this way, the weak amplitude factorizes into two terms.

As an example, consider the $D^0 \rightarrow K^-\pi^+$ mode. This decay proceeds mainly via external W-emission. Taking the matrix element of the above Hamiltonian between the states $|D^0\rangle$ and $\langle K^-\pi^+|$ and after performing all possible factorizations (by means of Fierz transformations), what is left is:

$$\langle K^-\pi^+|H_W^{eff}|D^0\rangle = \frac{1}{\sqrt{2}} G_F V_{cs}^* V_{ud} [a_1 \langle \pi^+|(\overline{u}d)_L|0\rangle \langle K^-|(\overline{s}c)_L|D^0\rangle + a_2 \langle K^-\pi^+|(\overline{s}d)_L|0\rangle \langle 0|(\overline{s}c)_L|D^0\rangle]$$

As can be seen in the above equation, the term proportional to a_1 (charged current interaction) is the product a factor describing π formation and a hadron matrix element.

The effective Hamiltonian describing two-body charm decays can now be written in the following manner:

$$H^{eff} = (G/\sqrt{2}) \cos^2(\theta) : [a_1(\overline{u}d)_H(\overline{s}c)_H + a_2(\overline{s}d)_H(\overline{u}c)_H] :$$

where the : [...] : represent Wick ordering. The subscripted H is meant to indicate that these are now hadron currents. a_1 and a_2 are real factors related to the QCD short-distance coefficients c_+, c_-, at a given renormalization energy μ, by:

$$a_1 = c_1(\mu) + \xi c_2(\mu), \quad a_2 = c_2(\mu) + \xi c_1(\mu)$$

where $\xi = 1/3$ is the color suppression factor. μ is on the order of the charm or bottom mass.

There are thus 3 classes of decays which can be observed: modes dominated by a_1 (class 1), those dominated by a_2 (class 2), and modes where a_1 and a_2 interfere (class 3). This organization provides a fertile testing ground for factorization, provided the appropriate hadron current matrix elements are known with

some confidence. These have been calculated by Bauer, Stech and Wirbel at zero momentum transfer using relativistic harmonic oscillator wavefunctions.

One aspect of this formalism is that the relative signs of a_1 and a_2 can be determined from class 3 decays. For $D \to PP$ decays (P is a member of the pseudoscalar nonet), the interference takes the general form $a_1 + x a_2$, where $x = +1$ in the $SU(3)$ flavor symmetry limit. For D^0 decays, however, the width depends only upon either a_1 or a_2. In particular, for the decays $D^0 \to K^-\pi^+$, $D^0 \to \pi^-\pi^+$ and $D^0 \to K^-K^+$, BSW have predicted that $\Gamma(D^0 \to K^-\pi^+) = 9.92\ a_1^2 \times 10^{10}$ s^{-1}, $\Gamma(D^0 \to \pi^-\pi^+) = 0.52\ a_1^2 \times 10^{10}\ s^{-1}$ and $\Gamma(D^0 \to K^-K^+) = 0.75\ a_1^2 \times 10^{10}$ s^{-1} [4].

Once the various matrix elements have been determined, the central values for a_1 and a_2 are obtained from experimental data.

1.1.2 Final State Interactions

The effective Hamiltonian detailed in the past two sections only describes quark decay. However, once final state hadronization has occurred, the decay products may still rescatter by strong processes, thereby changing the nature of the outgoing mesons (altering the decay amplitudes as well). Since the D lies in a resonance region, this effect will be more pronounced than in heavier meson decay, i.e. B decays. The final amplitude, after rescattering, can be written [4]:

$$A = S^{1/2} A^0$$

$$A = |A| e^{i\delta}$$

where A^0 is the "bare" amplitude (i.e. before final state interactions) and S is the strong interaction S-matrix for hadron-hadron scattering. This matrix will induce phase factors and mixings between channels having the same overall quantum

numbers. Given the large number of possible channels, however, S cannot be estimated.

Nevertheless, isospin analysis can reveal information about the relative phases of amplitudes to $I = 1/2$ and $I = 3/2$ final states. BSW have found that [4]:

$$|A_{1/2}| \simeq (3.35 \pm 0.19) \times 10^{-6} \text{ GeV}$$

$$|A_{3/2}| \simeq (0.99 \pm 0.38) \times 10^{-6} \text{ GeV}$$

$$\delta_{1/2} - \delta_{3/2} \simeq (77 \pm 11)^\circ$$

Based on these values, and using the factorization approximation to calculate the bare amplitudes A^0, a_1 and a_2 are found to be:

$$\frac{a_2}{a_1} \simeq -0.4 \pm 0.1$$

$$a_1 \simeq 1.3 \pm 0.1$$

$$a_2 \simeq -0.55 \pm 0.1$$

where the errors in the individual estimates are correlated.

Based on these values, the following branching ratios have been determined:

Mode	Branching Fraction (%) Theory
$D^0 \to K^-\pi^+$	5.8
$D^0 \to K^-K^+$	0.56
$D^0 \to \pi^-\pi^+$	0.39

Table 1.2: Theoretical Branching Fraction predictions (from [4]).

The lifetime of the D^0 was taken to be $\tau = (4.4 \pm 0.4) \times 10^{-13}$ sec. Of note is the prediction for the ratio of branching fractions between the Cabibbo-suppressed modes $D^0 \to K^-K^+$ and $D^0 \to \pi^-\pi^+$. This ratio is

$$R(K^-K^+/\pi^-\pi^+) \equiv \frac{BR(D^0 \to K^-K^+)}{BR(D^0 \to \pi^-\pi^+)} = 1.44$$

Evidently, as this result depends heavily on assumptions made for factorization, experimental results which concur within error with this result lend credence to such models. In comparison, another model, promulgated by Terasaki and Oneida [6], includes intermediate state contributions of the form $[qq][\overline{qq}]$. This model was formulated in an attempt to account for the MARK II [7] and MARK III [8] results of $R(K^-K^+/\pi^-\pi^+)_{\text{MARKII}} = 3.4 \pm 1.8$ and $R(K^-K^+/\pi^-\pi^+)_{\text{MARKIII}} = 3.7 \pm 1.4$. This model predicts a ratio of branching fractions of:

$$R(K^-K^+/\pi^-\pi^+) = 2.71$$

significantly higher than the BSW estimate.

1.2 CP Violation in the D^0-$\overline{D^0}$ system

CP violation was first detected in the $K^0 - \overline{K}^0$ system in 1964 by Cronin and Fitch, when it was observed that the decay $K_L^0 \to \pi^+\pi^-$ has a small probability of occurring (approximately 2×10^{-3} less often than $K_S^0 \to \pi^+\pi^-$). The kaon mass is small enough to limit the number of final states available to it when decaying. This serves to maximize the effects (mass splitting and lifetime difference, etc.) predicted by the formalism developed to explain this phenomenon, as interference between decay processes will be clearly observable. Heavier meson systems, which possess a greater number of decay channels, are not expected to display a large Δm or $\Delta\Gamma$.

1.2.1 D^0-$\overline{D^0}$ mixing

Eigenstates and time evolution

Mixing between particle and antiparticle occurs when mass eigenstates differ from the corresponding strong eigenstates (in this instance the D^0 and $\overline{D^0}$). Particle states produced by strong processes (such as occur in hadron-hadron collisions, for example) need not be eigenstates of the weak Hamiltonian, even though they diagonalize the strong contribution. The complete Hamiltonian, including strong, weak and electromagnetic terms, will therefore have off-diagonal terms in a basis formed of weak eigenstates.

This can be stated more formally in the following way, in complete analogy with the kaon system description found in [9]. Consider the initial $D^0 - \overline{D^0}$ superposition states $|\psi\rangle = |D^0\rangle$ and $|\overline{\psi}\rangle = |\overline{D^0}\rangle$ produced at time $t = 0$. At time t, one has:

$$|\psi(t)\rangle = a(t)|D^0\rangle + b(t)|\overline{D^0}\rangle$$

$$|\overline{\psi}(t)\rangle = \overline{a}(t)|D^0\rangle + \overline{b}(t)|\overline{D^0}\rangle$$

where the $|D^0\rangle$ and $|\overline{D^0}\rangle$ states are strong eigenstates. The time evolution functions a and b must satisfy the Schrödinger equation:

$$H|\psi\rangle = i\frac{\partial}{\partial t}|\psi\rangle$$

where H is the Hamiltonian governing the decay process, and similarly for $\overline{a}$ and $\overline{b}$. The Hamiltonian is not hermitian in this case, since the particles decay. However, H can be expressed as the sum of two hermitian operators M and Γ: $H = M - i\Gamma$. In a matrix formulation, this becomes:

$$i\frac{\partial}{\partial t}\begin{pmatrix} a \\ b \end{pmatrix} = [M - i\Gamma]\begin{pmatrix} a \\ b \end{pmatrix}$$

In general, if the states did not decay, one would have $\Gamma = 0$. Given that strong eigenstates are not weak ones as well, M and Γ will have off-diagonal elements, describing $D^0 - \overline{D^0}$ mixing. Assuming CP invariance, $M_{11} = M_{22}$ and $\Gamma_{11} = \Gamma_{22}$. The previous equation becomes:

$$i\frac{\partial}{\partial t}\begin{pmatrix} a \\ b \end{pmatrix} = \begin{pmatrix} M_{11} - i\Gamma_{11} & M_{12} - i\Gamma_{12} \\ M_{12}^* - i\Gamma_{12}^* & M_{22} - i\Gamma_{22} \end{pmatrix}\begin{pmatrix} a \\ b \end{pmatrix}$$

Switching to a basis that diagonalizes H_w, one gets the following eigenvectors [21]:

$$|D^0_{\alpha,\beta}\rangle = \frac{1}{\sqrt{2(1+\delta^2)}}\left[(1+\delta)|D^0\rangle + (1-\delta)|\overline{D^0}\rangle\right]$$

where δ is a measure of CP violation. The eigenvalues are:

$$\omega_\alpha = -im_\alpha - \frac{\gamma_\alpha}{2}$$

$$\omega_\beta = -im_\beta - \frac{\gamma_\beta}{2}$$

where

$$m_{\alpha,\beta} = M_{11} \pm \mathrm{Re}\left\{\sqrt{M_{12} - \frac{1}{2}i\Gamma_{12}}\sqrt{M_{12}^* - \frac{1}{2}i\Gamma_{12}^*}\right\}$$

$$\gamma_{\alpha,\beta} = \Gamma_{11} \pm \mathrm{Im}\left\{\sqrt{M_{12} - \frac{1}{2}i\Gamma_{12}}\sqrt{M_{12}^* - \frac{1}{2}i\Gamma_{12}^*}\right\}$$

and

$$\phi = \frac{1-\delta}{1+\delta} = \frac{M_{12}^* - i\Gamma_{12}^*/2}{\frac{1}{2}(\Delta m - i\Delta\Gamma/2)} - \frac{\frac{1}{2}(\Delta m - i\Delta\Gamma/2)}{M_{12} - i\Gamma_{12}/2}$$

where $\Delta m = m_\alpha - m_\beta$ and $\Delta\Gamma = \gamma_\alpha - \gamma_\beta$. The parameter δ, however, depends upon the choice of relative phase between the $|D^0\rangle$ and $|\overline{D^0}\rangle$ states. A phase independent measure of CP violation is:

$$\eta = \left|\frac{1-\delta}{1+\delta}\right| = \left|\frac{M_{12}^* - i\Gamma_{12}^*/2}{M_{12} - i\Gamma_{12}/2}\right|^{1/2}$$

CP nonconservation is reflected in η's departure from unity. Given all this, a state is therefore characterized by a time evolution of the sort (from the Schrödinger equation):

$$|\psi(t)\rangle = e^{-\omega_\alpha t}|D^0_\alpha\rangle + e^{-\omega_\beta t}|D^0_\beta\rangle$$

in the eigenvector basis. In the strong eigenstate basis, the time evolution functions are given by:

$$a(t) = e^{im_\alpha t - \gamma_\alpha t/2} + e^{im_\beta t - \gamma_\beta t/2}$$

$$\overline{a}(t) = e^{im_\alpha t - \gamma_\alpha t/2} - e^{im_\beta t - \gamma_\beta t/2}$$

$$b(t) = \frac{1-\delta}{1+\delta}[-e^{im_\alpha t - \gamma_\alpha t/2} + e^{im_\beta t - \gamma_\beta t/2}]$$

$$\overline{b}(t) = \frac{1-\delta}{1+\delta}[-e^{im_\alpha t - \gamma_\alpha t/2} - e^{im_\beta t - \gamma_\beta t/2}]$$

Thus a ratio of time-integrated "transition" probabilities can be defined between the D^0 and $\overline{D^0}$ states:

$$r = \frac{(D^0 \to \overline{D^0})}{(D^0 \to D^0)} = \int_0^\infty |b(t)|^2 \mathrm{d}t \Big/ \int_0^\infty |a(t)|^2 \mathrm{d}t = \eta^2 \Theta$$

and

$$\overline{r} = \frac{(\overline{D^0} \to D^0)}{(\overline{D^0} \to \overline{D^0})} = \int_0^\infty |\overline{b}(t)|^2 \mathrm{d}t \Big/ \int_0^\infty |\overline{a}(t)|^2 \mathrm{d}t = \eta^{-2} \Theta$$

Introducing the dimensionless variables:

$$x = \frac{\Delta m}{\Gamma}$$

$$y = \frac{\Delta \Gamma}{2\Gamma}$$

Θ is defined to be:

$$\Theta = \frac{x^2 + y^2}{2 + x^2 - y^2}$$

Also, as a result of these time evolution equations, the lifetime distribution of a meson created as a flavor eigenstate will not be purely exponential in character.

Calling $A(D^0 \to f) = A$ and $A(\overline{D^0} \to f) = \overline{A}$ for decays into a given final state f, one has [10, 11, 12]:

$$Rate(D^0 \to f) \propto e^{-\Gamma t}[(1 + \cos(\Delta m t)|A|^2 + (1 - \cos(\Delta m t)|\phi|^2|\overline{A}|^2 \\ -2\sin(\Delta m t)\mathrm{Im}(\phi\overline{A}A^*)]$$

Similarly,

$$Rate(\overline{D^0} \to f) \propto e^{-\Gamma t}[(1 + \cos(\Delta m t)|\overline{A}|^2 + (1 - \cos(\Delta m t)|\phi|^2|A|^2 \\ +2\sin(\Delta m t)\mathrm{Im}(\phi\overline{A}A^*)]$$

Details of this derivation are rather tedious and can be found in the appendix. The above expressions were obtained by assuming that $y = 0$. Since mixing is known to be much less than maximal in the D system, the additional assumption that $x \ll 1$ further simplifies them to:

$$Rate(D^0 \to f) \propto e^{-\Gamma t}|A|^2[1 - \frac{\mathrm{Im}(\phi AA^*)}{|A|^2}\sin(\Delta m t)]$$

and

$$Rate(\overline{D^0} \to f) \propto e^{-\Gamma t}|\overline{A}|^2(1 - \frac{\mathrm{Im}(\phi AA^*)}{|\overline{A}|^2}\sin(\Delta m t))$$

The following asymmetry Δ can then be defined:

$$\Delta = \frac{\Gamma(D^0 \to f) - \Gamma(\overline{D^0} \to f)}{\Gamma(D^0 \to f) + \Gamma(\overline{D^0} \to f)} \simeq \frac{2}{1 + |\rho_f|^2}\frac{x}{1 + x^2}\mathrm{Im}(\phi\rho_f)$$

where

$$\rho_f = \frac{A(\overline{D^0} \to f)}{A(D^0 \to f)}$$

by time integration of the above rates.

Theoretical Expectations and Possibilities

The Standard Model, as such, provides a mechanism for CP violation in the context of $D^0 - \overline{D^0}$ mixing, although predicted effects are much less than maximal. Large particle-antiparticle mixing, and consequently CP violation, can therefore be the signature of physics outside the established framework.

Standard Model predictions are based on calculating amplitudes from short-distance box diagrams, shown in Figure 1.4, and from long-distance intermediate state contributions. Short distance calculations predict very small values for Δm_D. In fact, $SU(3)$ flavor symmetry implies that Δm must vanish, although this symmetry is known to be broken. Using the $\Delta C = 2$ box diagrams, and considering only four quarks, the following estimate for Δm has been obtained [13]:

$$\frac{\Delta m_D}{\Delta m_K} = \left(\frac{M_s}{M_c}\right)^2 \left(\frac{f_D}{f_K}\right)^2 \frac{m_D}{m_K}$$

Using $M_s = 150$ MeV/c^2 and setting $f_D = f_K$, this amounts to:

$$\Delta m_D = 1.3158 \times 10^{-16} \quad \text{GeV/c}^2 \qquad x = 10^{-4}$$

Another calculation [13], using the more realistic strange mass $M_s = 500$ MeV/c^2, yields:

$$\Delta m_D = 1.3158 \times 10^{-15} \quad \text{GeV/c}^2 \qquad x = 10^{-3}$$

If external momenta are taken into account, one obtains:

$$\Delta m_D = 1.3158 \times 10^{-18} \quad \text{GeV/c}^2 \qquad x = 10^{-6}$$

Evidently, all these values are far from maximal. The resulting values for y are all also extremely small. It has been pointed out, however, that short-distance methods are inadequate for calculating mass and width splittings [14]. Long-distance

contributions, meaning virtual intermediate hadronic states, are between 1 and 2 orders of magnitude more important than effects from second order weak processes such as the above-mentioned box diagrams. Calculations where the intermediate states are limited to pairs of charged pseudoscalar particles (*i.e.* $\pi\pi$, KK and $K\pi$) yield [15]:

$$\Delta m_D^{int} \simeq 0.7 \times 10^{-15} \ \text{GeV/c}^2 \qquad x = 5.3 \times 10^{-6}$$

compared to the box diagram value of:

$$\Delta m_D^{box} \simeq 2.5 \times 10^{-17} \ \text{GeV/c}^2 \qquad x = 2 \times 10^{-7}$$

This is still much smaller than experimental results from E691 [16]:

$$|\Delta m_D^{expt}| \leq 1.5 \times 10^{-13} \ \text{GeV/c}^2 \qquad x \leq 10^{-1}$$

Presumably, other states besides charged pseudoscalar pairs contribute to long-distance mixing. These contributions, however, cannot be treated with any degree of confidence at present. Nevertheless, a clear consequence of these estimates is that values of x greater than around the 1% level are a hallmark of physics beyond the Standard Model.

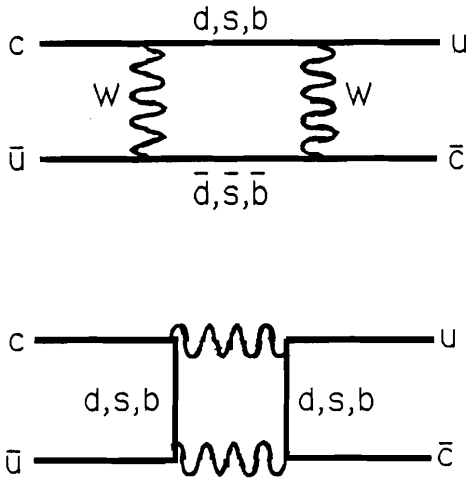

Figure 1.4: Box diagrams contributing to $D^0 - \overline{D^0}$ mixing.

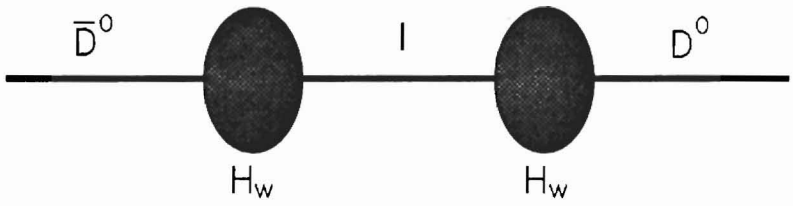

Figure 1.5: Intermediate state (long distance) contribution to $D^0 - \overline{D^0}$ mixing (from [15]).

1.2.2 Direct CP violation in D^0 decays

Particle-antiparticle mixing is one source of CP violations among neutral mesons, but not the only means by which such phenomenon can occur. Interference between different processes leading to the same final state will produce similar effects as mixing. In the case of charged mesons, this is in fact the only way in which CP violation can occur.

In the following, only heavy quark decays to two pseudoscalar mesons will be considered in order to simplify the discussion.

Interference between Amplitudes

In general, the decay $D^0 \to PP$, where P denotes some pseudoscalar meson (K or π), can proceed by all six Feynman diagrams shown in the previous section. The plentiful, Cabibbo-allowed decay $D^0 \to K^-\pi^+$ may proceed via W-emission (external spectator diagram) or by W-exchange. Since the latter is helicity-suppressed, almost all of the decays occur by W-emission. There is therefore little or no interference between diagrams, and CP symmetry is not violated.

It is perhaps evident that CP violating effects are most readily observed in suppressed modes, as these have a greater likelihood of proceeding via diagrams which have comparable amplitudes. An example are the decays $D^0 \to K^-K^+$ and $D^0 \to \pi^-\pi^+$. Both final states can be reached by four diagrams. These are external W-emission (spectator), W-exchange and both regular and timelike penguin diagrams. Of note is that all processes are Cabibbo-suppressed. The overall amplitudes can be summarized in the following table [9]:

Mode	Amplitude
$D^0 \to K^-\pi^+$	$V_{ud}V_{cs}^*(A+C)$
$D^0 \to K^-K^+$	$V_{us}V_{cs}^*(A+C+E+2F)+V_{ud}V_{cd}^*(E+2F)$
$D^0 \to \pi^-\pi^+$	$V_{us}V_{cs}^*(E+2F)+V_{ud}V_{cd}^*(A+C+E+2F)$

Table 1.3: Amplitudes for three D^0 decay modes.

where the capitals refer to the processes presented in Figures 1.1-1.3. In order to obtain the amplitudes for the CP conjugate process, one must replace V_{ij} by V_{ij}^*. Interference between two processes, for instance, can be understood by considering the matrix element [12]:

$$M_f = \langle f|H|D^0\rangle = \langle f|H_1|D^0\rangle + \langle f|H_2|D^0\rangle$$

where H_1 and H_2 denote the parts of the Hamiltonian describing a given diagram. Explicitly factoring out the strong phase shifts θ_i, this can be rewritten as:

$$M_f = g_1 M_1 e^{i\theta_1} + g_2 M_2 e^{i\theta_2}$$

where M_i, g_i are the matrix elements for the H_i with weak parameters g_i (CKM matrix elements). For the CP conjugate decay, one has:

$$\overline{M}_f = \langle f^{CP}|H|\overline{D^0}\rangle = g_1^* M_1 e^{-i\theta_1} + g_2^* M_2 e^{-i\theta_2}$$

thus

$$\Gamma - \overline{\Gamma} \propto \mathrm{Im}(g_1^* g_2)\sin(\theta_1 - \theta_2) M_1 M_2$$

A concrete example is given by a decay to two pseudoscalars. For instance, for the decay $D^0 \to K^-K^+$, one has:

$$A(\overline{D^0} \to K^-K^+) = V_{us}^* V_{cs}(A+C+E+2F) + V_{ud}^* V_{cd}(E+2F)$$

As for CP violation via mixing, the quantity Δ can be defined:

$$\Delta = \frac{\Gamma - \overline{\Gamma}}{\Gamma + \overline{\Gamma}} = \frac{|A|^2 - |\overline{A}|^2}{|A|^2 + |\overline{A}|^2}$$

Writing $A(D^0 \to K^-K^+) = V_{us}V_{cs}^*\alpha + V_{ud}V_{cd}^*\beta$ and $A(\overline{D^0} \to K^-K^+) = V_{us}^*V_{cs}\alpha + V_{ud}^*V_{cd}\beta$, Δ is readily found to be:

$$\Delta = \frac{-4\mathrm{Im}(V_{us}V_{cs}^*V_{ud}^*V_{cd})\mathrm{Im}(\alpha\beta^*)}{|A|^2 + |\overline{A}|^2} = \frac{4s_1^2s_2s_3s_\delta c_1c_2c_3\mathrm{Im}(\alpha\beta^*)}{|A|^2 + |\overline{A}|^2}$$

where the elements of the CKM matrix have been expressed in the Kobayashi-Maskawa parametrization and α and β include strong phases. From this, it is evident that an asymmetry exists only if α and β have a relative complex phase. This is true if a phase shift is generated by the strong interaction (i.e. $\theta_1 \neq \theta_2$). Bigi and Sanda [12] have pointed out that, given that two amplitudes will in general differ in their isospin structure, non-trivial strong phase differences will occur, although there is at present no reliable way of estimating these.

The usefulness the decay $D^0 \to PP$

Based on the discussion above, the useful nature of PP states which are also CP eigenstates is obvious. The Cabibbo-suppressed decays $D^0 \to K^-K^+$ and $D^0 \to \pi^-\pi^+$ produce a pair of kaons and pions in a CP $= +1$ state, respectively. Given this Cabibbo suppression, CP violating effects are more readily observed in these modes than in the allowed decay $D^0 \to K^-\pi^+$. At first, obtaining enough statistics may seem a problem, however these channels command branching ratios of order $BR(D^0 \to K^-K^+) \simeq 0.5\%$ and $BR(D^0 \to \pi^-\pi^+) \simeq 0.2\%$, thereby enabling a high statistics charm experiment to gather a fairly large event sample.

Due to the strong D^* decay, there exists a straightforward way to determine the flavor content of the parent D. The decays

$$D^{*+} \to D^0\pi^+$$

$$D^{*-} \rightarrow \overline{D^0}\pi^-$$

reveal, by the charge of the "bachelor" pion, whether the heavy quark is charm or anticharm. In this way, one can obtain separate samples of $D^0 \rightarrow K^-K^+$ and $\overline{D^0} \rightarrow K^-K^+$, thereby simplifying the measurement of such quantities as Δ, which only reveal global CP violation, or detecting non-exponential lifetime distributions, a signature of $D^0 - \overline{D^0}$ mixing.

Physics beyond the Standard Model

Several schemes involving physics outside the standard model have been put forward in order to raise the theoretical estimate of Δm_D, thereby making it commensurate with the experimental limit. These include SuperSymmetric (SUSY) [17] additions to the Standard Model, an extended Higgs sector, or non-minimal Supergravity [10].

Minimal SUSY additions will not enhance $D^0 - \overline{D^0}$ mixing. It has been pointed out, however, that non-minimal models [17, 10] can be constructed where flavor changing neutral currents are unrelated to the CKM matrix. Given this, it seems possible that theoretical estimates will reach the experimental bound.

1.3 Charm Production and Detection

Although its existence was postulated in order to eliminate the existence of quark flavor-changing neutral currents via the Glashow-Iliopoulos-Maiani (GIM) mechanism as early as 1964, charm was not detected experimentally until ten years later, when in November 1974, the J/ψ was discovered in e^+e^- annihilations, as well as in $p - p$ collisions. This particle, a $c - \overline{c}$ quarkonium state, had an invariant mass of 3.1 GeV/c^2. Shortly afterwards, another resonance, the ψ', was discovered at 3.7 GeV/c^2.

1.3.1 Charm Photoproduction

Initially, charm production and detection experiments were limited to e^+e^- environments, such as SPEAR. The major advantages of $e^+e^- \rightarrow \gamma \rightarrow c\bar{c}$ (virtual photon) processes are the high charm fraction ($\sim 40\%$) and low multiplicities (thus low background) per event. The main problem is the low cross-section for e^+e^- collisions, severely limiting signal statistics at current luminosities. Fixed target experiments, using either photon or hadron beams, provide much higher interaction rates, but this advantage is mitigated by the much greater backgrounds produced by hadron-hadron or photon-hadron collisions.

Of the two options mentioned above, photon beams, in fixed target environments, provide the greater fractional charm yield ($\sim 1\%$), compared to hadron beams, where the level of charm production is an order of magnitude lower [18]. Charm-anticharm production in γ beams is expected to proceed via photon-gluon fusion [19]. The first order Feynman diagram for this process is shown in Figure 1.6. As will be discussed in the next chapter, γ beams are created by using the photons produced during Bremsstrahlung processes, and will display the appropriate energy distribution. Given the spread in beam γ energies, the entire charmed meson invariant mass spectrum will be produced, in contrast with e^+e^- machines, where the beam energy typically is set to some resonant mass. Given the technology involved, high energy photon beams can be produced with relative ease.

1.3.2 Experiment E691 at Fermilab

Fermilab experiment E691, though not the first experiment to make use of photon beams, is the first to detect large numbers of charmed particles. Several factors enabled the collaboration to amass high statistics signals. The first is the choice of

photoproduction over hadroproduction as the means for charm creation. As was stated above, this improved the fractional charm content by an order of magnitude.

Although the Tagged Photon Spectrometer's basic design, discussed in the next chapter, is that of a traditional magnetic spectrometer (hardly new in fixed target charm physics experiments) augmented by both Čerenkov counters for particle identification and calorimeters, the inclusion of a silicon microstrip detector for particle tracking permitted the reconstruction of both interaction and decay points with the resolution necessary to identify charmed particles.

This ability to separate charm production from decay is in principle acheivable with bubble chambers and emulsion techniques. However, these devices do not have the rapid SMD cycling (readout) time which would allow high data acquisition rates. This, coupled with a fairly "open" trigger, allowed a large number of interactions to be written to tape. The Tagged Photon Spectrometer therefore combined an efficient means of $c - \overline{c}$ production with the apparatus necessary to detect charmed mesons, thereby providing a charmed meson sample large enough to measure the ratio of branching fractions $BR(D^0 \rightarrow K^-K^+)/BR(D^0 \rightarrow \pi^-\pi^+)$ as well as to search for evidence of CP violation.

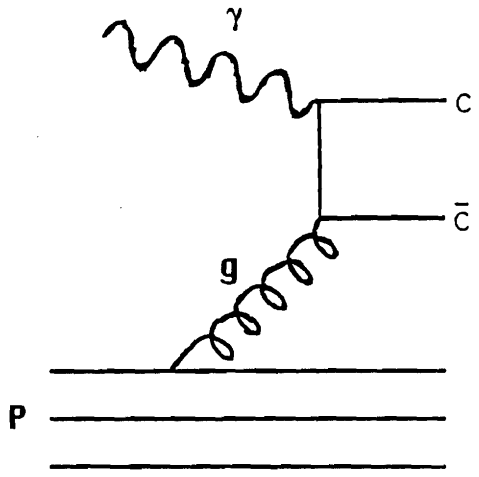

Figure 1.6: First order Feynman diagram for Photon-Gluon Fusion.

Chapter 2 Apparatus

The E691 collaboration took data over a five month period ending in September 1985 at the Tagged Photon Laboratory at Fermilab. This fixed target run marked the first time the new superconducting Tevatron had operated over a sustained period of time, providing primary proton beams of energy 800 GeV or greater.

2.1 The Tevatron

The Tevatron, sometimes referred to as the Saver, is the final acceleration stage for protons (and antiprotons) at the Fermi National Accelerator Laboratory. An alternating gradient synchrotron (AGS), its superconducting magnets allow p and $\overline{p}$ particles to reach energies of $\sim$ 0.8 to 1 TeV.

Protons for the Tevatron are produced by ionizing hydrogen gas. The H^+ ions are accelerated in a Cockroft - Walton electrostatic generator to approximately 750 - 800 keV. Following this, the protons are injected into a 160 m linac, raising their energy to 200 MeV. The next step is a booster ring, which brings the protons to 8 GeV. At this point, they are injected into the Main Ring, a traditional (*i.e.* non-superconducting) AGS, accelerating the protons to 150 GeV. After this, the protons are sent into the Tevatron, for a final boost to 800 - 1000 GeV, and then extracted for use in the various fixed target areas.

In the Tevatron, the protons are "bunched" by the ring's radiofrequency cavities into groups (termed buckets) approximately 2×10^{-9} s long, separated by 19×10^{-9} s. Given the process by which the E691 beam is produced, one finds the same structure in the photons arriving at TPL. The protons are extracted from the Tevatron roughly each minute, during a 20 s "spill", during which $\sim$ 25% of the

available protons are sent to the P-east beamline.

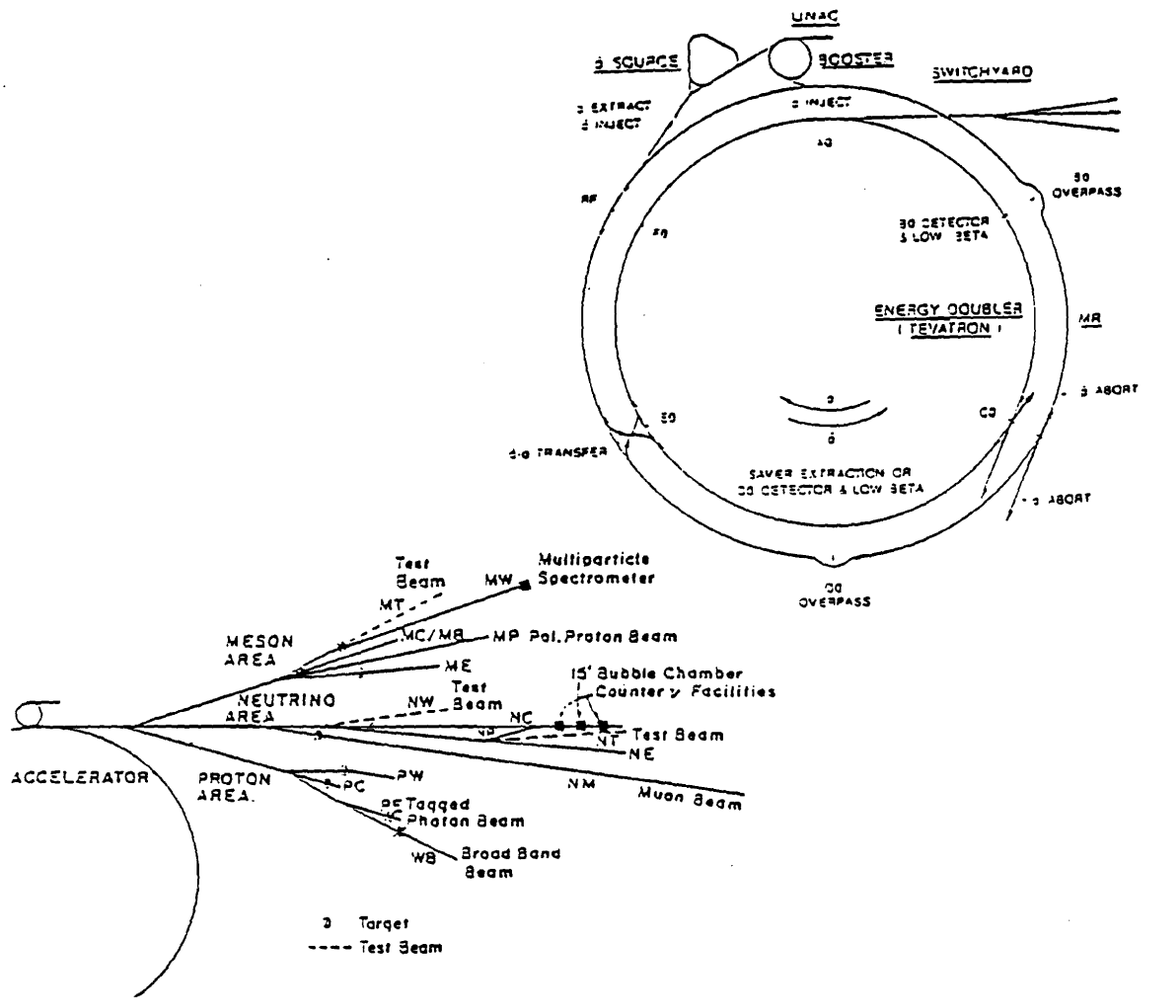

Figure 2.1: Fermilab Accelerators and Beamlines.

2.2 The Beam Line

The photons used for charm production at TPL form a quaternary beam, the result of a three-step process. The initial protons extracted from the Tevatron ring are focused onto a 30 cm beryllium target. All of the charged secondaries resulting from this collision are filtered out by a magnetic field, leaving only neutrals (*i.e.* π^0s and other neutrals) and photons in the beam. These strike a 0.32 cm lead target, where the photons convert to e^+e^- pairs. The negative component is magnetically selected and transported through a series of focusing quadrupoles (both in the horizontal and vertical directions), bending dipoles and collimators. By controlling the p_t kick of each dipole, the beam is made fairly monoenergetic (260 $\pm$ 18 GeV) and pion free, since pions have higher average transverse momentum than electrons.

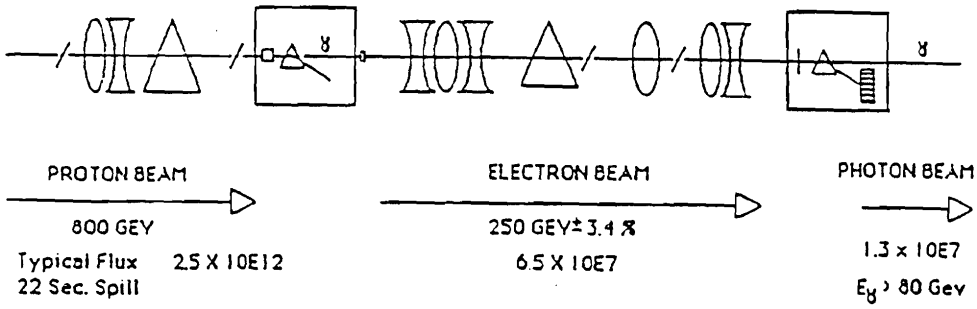

Figure 2.2: Diagram of P-east beamline.

The electron beam then strikes a tungsten block (0.2 radiation lengths thick) and radiates bremsstrahlung photons. As the electron beam reaches the radiator, it contains less than 1% pions [20]. The electrons themselves are bent out of the way by a magnet into a tagging hodoscope, which serves to measure the γ energy, the distribution of which is shown in Figure 2.3. The resulting photon beam is tightly collimated ($\theta \sim \frac{1}{\gamma}$, $\gamma = \frac{E_e}{m_e} \sim 10^3$), with a mean energy of 145 GeV. It then proceeds into the experimental hall before interacting with a 5 cm beryllium target, described below. There is a small scintillation counter (B-counter) located behind the target to record the passage of interaction products. The resulting particles are tracked by the Tagged Photon Spectrometer.

A coordinate system was established in the following way: +z is in the beam direction, pointing downstream; +y points upwards; +x points west. The coordinate system is right-handed. The $z = 0.0$ point is the interaction (B-) counter located behind the target.

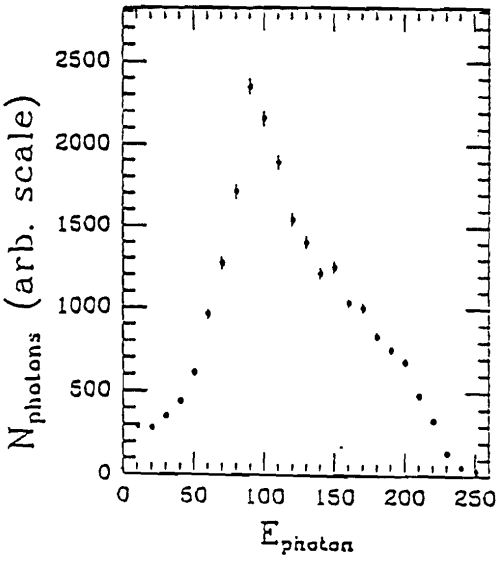

Figure 2.3: Distribution of γ energies in E691 beam.

2.3 The Tagged Photon Spectrometer

The Tagged Photon Spectrometer (TPS) is a large acceptance general-purpose spectrometer composed, in rough order of appearance to a particle, a silicon microstrip position detector, thirty-five drift chamber planes, two high-field bending magnets, Čerenkov detectors, electromagnetic and hadronic calorimeters, and muon detectors. These allow precise particle tracking and identification. Figure 2.4 depicts the TPS as it appeared in E691. The discussion to follow will be limited to an overview of these detectors. More detailed descriptions can be found in various references [20, 21, 22].

2.3.1 The Target

The target used during the E691 run consisted of a small block of beryllium, approximately 1.25 cm (x) $\times$ 2.5 cm (y) $\times$ 5 cm (z). The transverse dimensions were large enough to completely contain the beamspot, whose extent was $\Delta x \sim 0.8$ cm and $\Delta y = 1.8$ cm. In order to avoid toxicity problems, the target was coated with plastic and could thus be safely handled.

Beryllium was chosen as the material since it provided a happy medium between the need for a low enough density to avoid pair production and multiple scattering (requiring low Z), and the desire for high hadronic cross sections and good spectrometer acceptance. Be is the lightest element available in solid form.

2.3.2 The Silicon Microstrip Detector

The silicon microstrip detector proved to be perhaps the most important component of the TPS. The high resolution achievable with silicon planes allowed the full reconstruction of secondary (decay) vertices, as well as the separation of these last from the interaction point, enabling a drastic reduction in the amount

of combinatoric background.

The detector itself is composed of nine planes, grouped in clusters of three. A schematic of the system is shown in Figure 2.5.

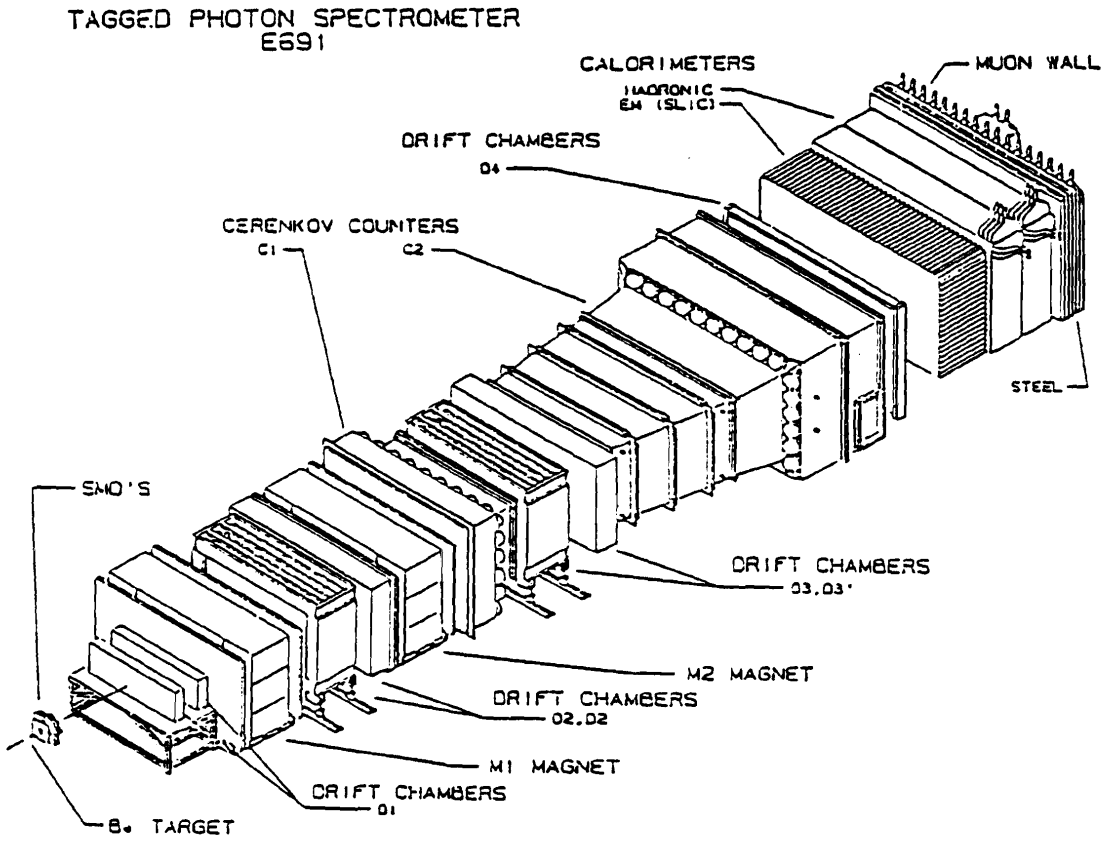

Figure 2.4: The Tagged Photon Spectrometer.

The first plane is located 2.7 cm behind (downstream of) the beryllium target, and the intergroup spacing is 8 cm. The first three planes were produced by Enertec-Schlumberger, while the remaining six were built by Micron Semiconductor. Each cluster contained x, y and v measuring planes, where v is tilted at 20.5° relative to x. Parameters of the SMD system are listed in the following table:

Group	1	2	3
dimensions (cm)	2.6×2.6	5.0×5.0	5.0×5.0
strip pitch (μm)	50	50	50
# strips/plane	512	768	1000
view ordering	x, y, v	y, x, v	x, y, v
z position (cm)	1.931,3.015,6.684	11.046,11.342,14.956	19.915,20.254,23.876

Table 2.1: Parameters of the E691 silicon microstrip system (from [20]).

All silicon planes are $\sim$ 300 μm thick. The appropriate number of strips were instrumented in each in order to keep the angular acceptance of the SMD system constant at $\pm$ 100 mrad. The Enertec-Schlumberger (ES) planes were fully depleted at 90 V, while the Micron Semiconductor (MS) planes required 70 V to deplete.

The ES planes were connected to readout electronics via fanouts printed on kapton sheets. The strips were individually wire-bonded to the corresponding printed circuit fanout. The MS strips were bonded to circuit patterns on copper-coated G10 board, which in turn fan out to thin kapton sheets. In both cases, the kapton elements lead to preamplifiers. Both the ES and MS planes were mounted in light-tight RF cages to reduce noise (aluminum for ES planes, Cu-coated stesalite

for the MS planes). These boxes were mounted in the beamline using a special alignment system [21], insuring strip parallelism to less than 1 mrad.

All planes are readout using two-stage amplification. The first step is a "hybrid" preamplifier, consisting of both discrete surface-mounted components and thick-film resistors, designed by Jarron *et al.* [23], and manufactured by Laben (model MSD2). Each preamplifier has four channels, and they are grouped in clusters of 32 inside silver-plated aluminum housings, termed "card cages". These cages are mounted on the sides of the housings containing the planes themselves. In order to insure uniform response, each hybrid channel was individually tested and calibrated. Each channel had a current gain of $\sim$ 200, and a risetime of $\sim$ 3 ns. Typical preamp output for a minimum-ionizing particle was 1 mV.

The second stage of the readout consists of modified MWPC discriminator cards, model S710/810 manufactured by Nanosystems. Each card has eight channels, and were stacked in RF cages to minimize noise. The factory-raw models were modified by adding a transistor to invert the preamp output, and a potentiometer to adjust the discriminator level. The signals were brought from the preamps to the cards via nine-channel shielded ribbon cable, each cable having four signal lines interleaved with five ground wires, which were common with the grounds on both preamps and discriminators. The discriminator thresholds were set at 0.5 V. Once a channel had fired, the output was stored in a shift register, and read out serially by CAMAC scanners, also built by Nanosystems.

All SMD planes functioned well during the E691 run, the resolution being 16 μm, very close to the minimum of $\frac{50}{\sqrt{12}} = 14$ μm. The per-plane efficiency was around 95%, dead strips being the cause of the small inefficiency.

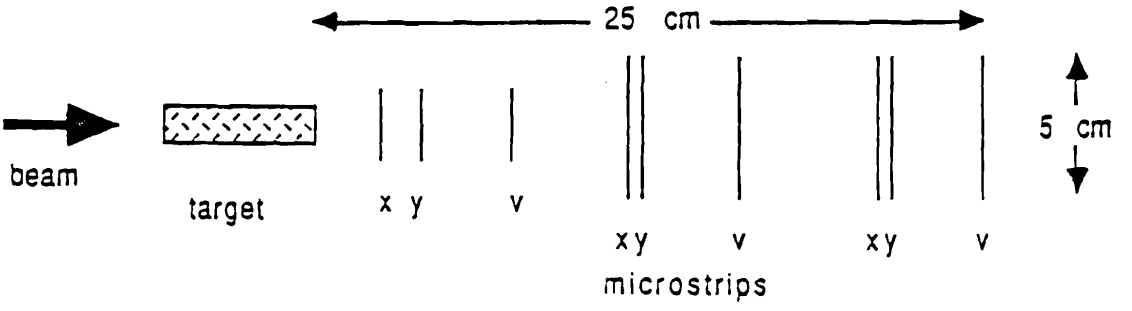

Figure 2.5: Diagram of the Silicon Microstrip Detector.

2.3.3 The Drift Chambers

Once out of the SMD region, tracking was accomplished by four drift chamber assemblies. The first, D1A and D1B, is located just behind the SMD detector and before the first magnet, M1. The second assembly, D2, is located between M1 and the second magnet, M2. The third set of drift chamber planes, D3, is located between the two Čerenkov counters, downstream of M2. The last chamber, D4, is located just upstream of the electromagnetic calorimeter (the SLIC). There is a total of 35 planes in all. Some drift chamber parameters are listed in the following table:

Assembly	D1	D2	D3	D4
dimensions (cm^2)	160 × 120	230 × 200	330 × 200	550 × 300
cell size x (cm)	0.476	0.953	1.588	3.18
cell size u,v (cm)	0.446	0.892	1.487	2.97
# of channels	1536	2400	1952	416
resolution (cm)	0.035	0.030	0.030	0.080

Table 2.2: Parameters of the E691 drift chamber system (from [20]).

The first stations, D1A and D1B, contain four sense planes each, measuring x, u, v, x′ (where u and v are tilted ±20.5° relative to x). The redundant x′ measurement resolves left-right hit ambiguities. Its location right behind the silicon provided additional hit information, enabling a more precise measurement of track parameters, as well as a means of discarding false tracks. The second station, D2, is composed of four x, u, v triplets. This station is located between the magnets, and therefore is very important in momentum measurements. D3, at the exit of M2, is similar in construction to D2, although with a larger cell size. D4, the last station, is also similar to D2 in construction.

All chambers share a similar structure: cathode planes separated by sense planes. All cathode planes are held at negative high voltage, typically -2.1 kV. The sense planes in chambers D1-D3 are composed of alternating field-shaping, held at -1.7 to -1.5 kV, and grounded sense wires. In D4, however, the sense wires are held at high voltage, while the cathode planes are grounded. This setup is illustrated in Figure 2.6. The gas mixture used in all chambers was approximately 50% argon and 50% ethane, with a small admixture of ethanol ($\sim$ 1.5%) for quenching purposes. The chambers were operated with the $Ar - CH_4$ mixture at slightly above 1 atm. Under these conditions, the gas gain was about 2×10^5 and the typical drift velocity was 40 μm/ns.

In every case, 16 channel Lecroy DC201 and Nanomaker N-227C amplifier-discriminator cards were mounted on top of the chambers. The output signals were carried to CAMAC Lecroy 4290 TDCs via twisted pair cables. The 4290 system has a crate controller for rapid formatting and transfer, as well as a 4000 16-bit word buffer. Time offsets due to varying cable lengths and the like are automatically subtracted by an external "autotrim" feature. A detailed discussion about calibration procedures and determination of the varying offsets can be found in [20].

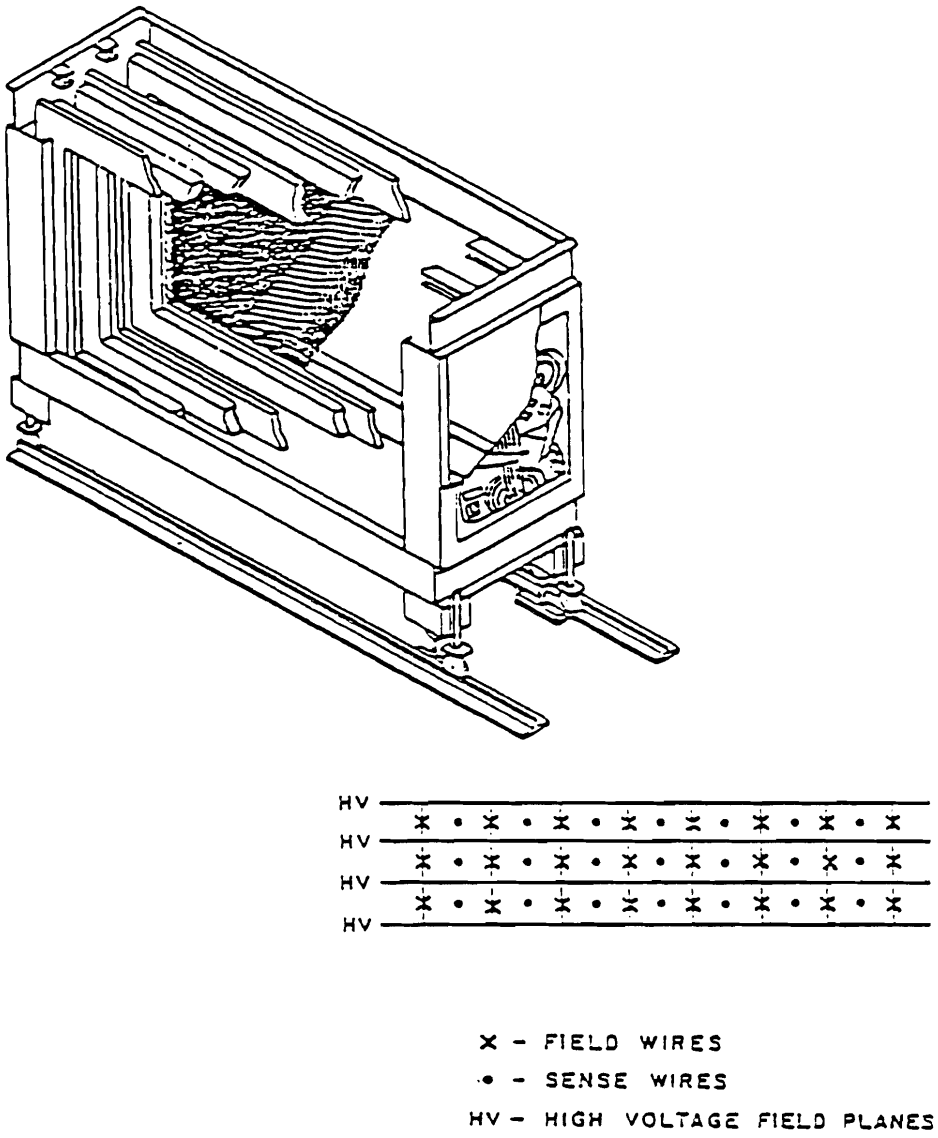

Figure 2.6: Cutaway of a drift chamber and wire setup (from [20]).

2.3.4 The Magnets

The TPS includes two magnets, providing a dual means of measuring momentum. The first, M1, is located behind the first drift chamber assembly, while the second, M2, is located downstream of D2. These large-aperture coils give a 530 MeV/c kick to charged particles passing through them. The fields of both point in the -y direction, deflecting negatives to the west. Physical parameters are given in the following table:

Magnet	M1	M2
entrance aperture (cm^2)	154 × 73	154 × 69
exit aperture (cm^2)	183 × 91	183 × 96
length (cm)	165	208
E691 current (A)	2500	1800
$\int B_y(0,0,z)dz$ (T-m)	-0.71	-1.07
p_T kick GeV/c	0.21	0.32

Table 2.3: Parameters of the E691 magnets (reproduced from [20]).

The deflection angle is given by

$$\theta \simeq \frac{\int B \cdot dl}{3.33p}$$

where B is in Tesla, p is in GeV/c, and l in meters. The momentum resolution. which is dependent upon the position resolution σ_x, is given by:

$$\left|\frac{\sigma_p}{p}\right| \simeq \frac{\sigma_x p}{0.03Bl^2}$$

where the same units apply. It is evident that momentum resolution improves with a corresponding increase in magnetic field strength. The error in x, σ_x, is just the quadrature sum of errors before and after the particles' trip through the magnet:

$$\sigma_x = \sqrt{\sigma_{x1}^2 + \sigma_{x2}^2}$$

The final momentum resolution, for tracks traversing both magnets, is $\frac{\sigma_p}{p} \simeq 0.05\%p + 0.5\%$. For tracks crossing only one magnet, this degrades to $\frac{\sigma_p}{p} \simeq 0.1\%p + 0.5\%$. The constant 0.5% error is due to uncertainties caused by multiple scattering. For particles only interacting in the fringe field of M1, this reduces further to $\frac{\sigma_p}{p} \simeq 0.6\%p$. The mass resolution, which is compounded by error on the opening angle θ between two particles, is given by:

$$\frac{\sigma_m}{m} \simeq \frac{1}{2}\sqrt{(\sigma_1/p_1)^2 + (\sigma_2/p_2)^2 + 4(\sigma_\theta/\theta)^2}$$

where $\sigma_\theta \propto \delta/L$, where L is the distance between measuring stations. At the J/ψ mass (3.1 GeV/c^2), this leads to a mass uncertainty of 27.4 MeV/c^2 for the dimuon decay $J/\psi \rightarrow \mu^+\mu^-$, and an uncertainty of 10.3 MeV/c^2 at the charm mass for the decay $D^0 \rightarrow K^-\pi^+$ [21].

2.3.5 The Čerenkov Counters

Particle identification at TPL is achieved in part with two Čerenkov counters, C1 and C2. The first, C1, is located just behind the first magnet, M1. The second detector is downstream of the third drift chamber assembly. Used in tandem, these provide particle ($\pi/K/p$) separation from 6 GeV/c to well over 70 GeV/c.

Both counters operate by reflecting the radiation produced by a particle off of spherical mirrors, arranged in an approximate plane, into a phototube assembly. The first counter, C1, due to space limitations, uses a "double-bounce" geometry. Radiation is produced when a particle's velocity exceeds that of light in a given medium:

$$v \geq \frac{c}{n}$$

where n is the medium's index of refraction. Photons are emitted in a cone whose

half-opening angle θ_c is given by:

$$\cos(\theta_c) = \frac{1}{\beta n}$$

The number of photons produced per unit wavelength per unit length, is proportional to the sine of this angle:

$$\frac{\partial^2 N_\gamma}{\partial\lambda\partial l} = \frac{2\pi\alpha}{\lambda^2}\sin^2(\theta_c) = \frac{2\pi\alpha}{\lambda^2}\left(1 - \frac{p_{th}^2}{p^2}\right)$$

where p_{th} is the momentum corresponding to threshold velocity. One can also write this quantity as:

$$p_{th} \simeq \frac{mc}{\sqrt{2(n-1)}}$$

Threshold momentum can therefore be "tuned" by selecting a radiating medium with an appropriate index of refraction. This choice must take into account other factors, such as the need to minimize multiple scattering. Given knowledge of p_{th}, if a particle's momentum is known, it provides bounds to the particle's mass: $p \geq p_{th}$, so $m \leq p\sqrt{2(n-1)}/c$ and $m \geq p_{th}\sqrt{2(n-1)}/c$, since the particle produced Čerenkov light. Note that by using two (or more) counters with distinct threshold momenta, it is possible to determine the nature of a particle by observing which counters detect light.

Some physical parameters of the two counters are given in the table on the following page.

Counter	C1	C2
length (cm)	370	660
Number of cells	28	32
gas	N_2	80% He + 20% N_2
refractive index	$1 + 3.09 \times 10^{-4}$	$1 + 0.901 \times 10^{-4}$
radius of radiation cone (max. in cm)	8.4	8.7
π threshold (GeV/c)	6.0	10.5
z of mirror plane (cm)	866	1653

Table 2.4: Parameters of the E691 Čerenkov counters (from [22]).

The numbers of photons produced as a function of particle momentum for both counters are shown in Figure 2.7. The intersection of the curve with the momentum axis is p_{th}. Based on these graphs, it is obvious that only pions radiate between 6 GeV/c and 20 GeV/c. Kaons are uniquely identified between 20 GeV/c and 37 GeV/c. Protons are separable between 37 GeV/c and 70 GeV/c. Beyond 70 GeV/c, all particles radiate in both counters, making more elaborate reconstruction schemes necessary in order to provide $\pi/K/p$ separation. The reconstruction algorithm which determines particle probabilities by making use of the recorded pulseheights is described in the next chapter.

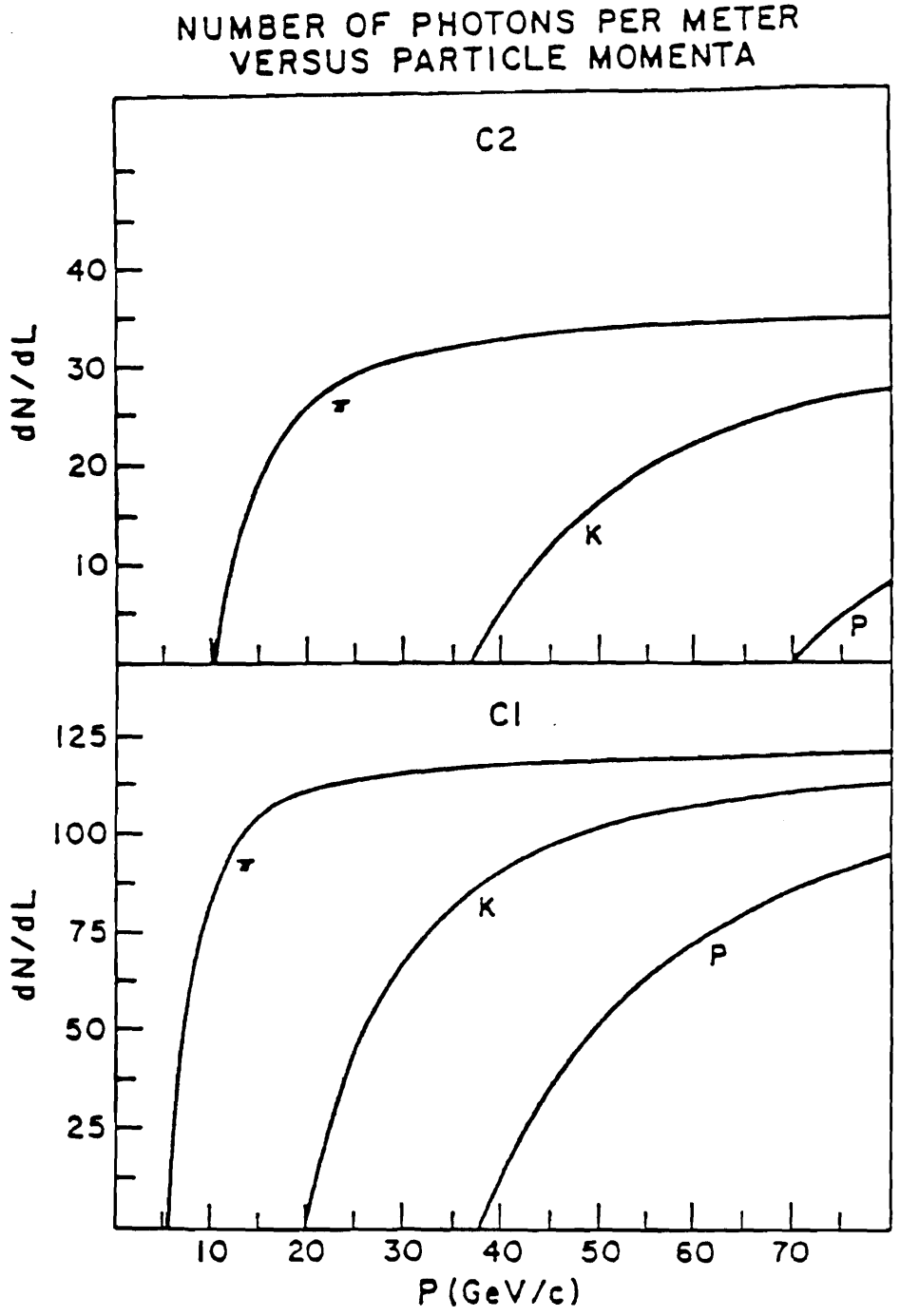

Figure 2.7: Photon production for C1 and C2 (from [22]).

The most upstream counter, C1, was located partially inside the second magnet, M2, in order to conserve space. In this counter, twenty-eight mirrors focused radiated light into a phototube assembly after two intermediate reflections (once again, in order to reduce the z dimension of the apparatus). The PMT system consisted of a 20° Winston cone attached by way of a short light pipe to a 5″ RCA 8854 photomultiplier tube. This tube had a very high-gain first dynode, rendering it capable of resolving single photo-electrons. The front faces of the tubes were coated with waveshifter to boost efficiency in the UV range. The phototube outputs were digitized using LeCroy 2249 ADCs. Stray magnetic fields from M2 were eliminated by shielding the phototubes with cast iron, and by coiling current-carrying wire around the tubes themselves.

The downstream counter, C2, is located between the third and fourth drift chamber assemblies. Here, the mirror plane is composed of thirty-two mirrors. The radiated light is only reflected once into phototube assemblies similar to those used in C1. The only difference is the greater shielding employed against the possibility of helium leaks (which would degrade the cathode of the tubes). To prevent this, the tubes were sealed behind clear windows, and the space between the Winston cones and tube faces flushed with dry nitrogen. The readout electronics were the same as those used in C1. The average number of photoelectrons collected per track was $\sim$ 11 in C1 and $\sim$ 13 in C2. Diagrams of both counters are shown in Figure 2.8.

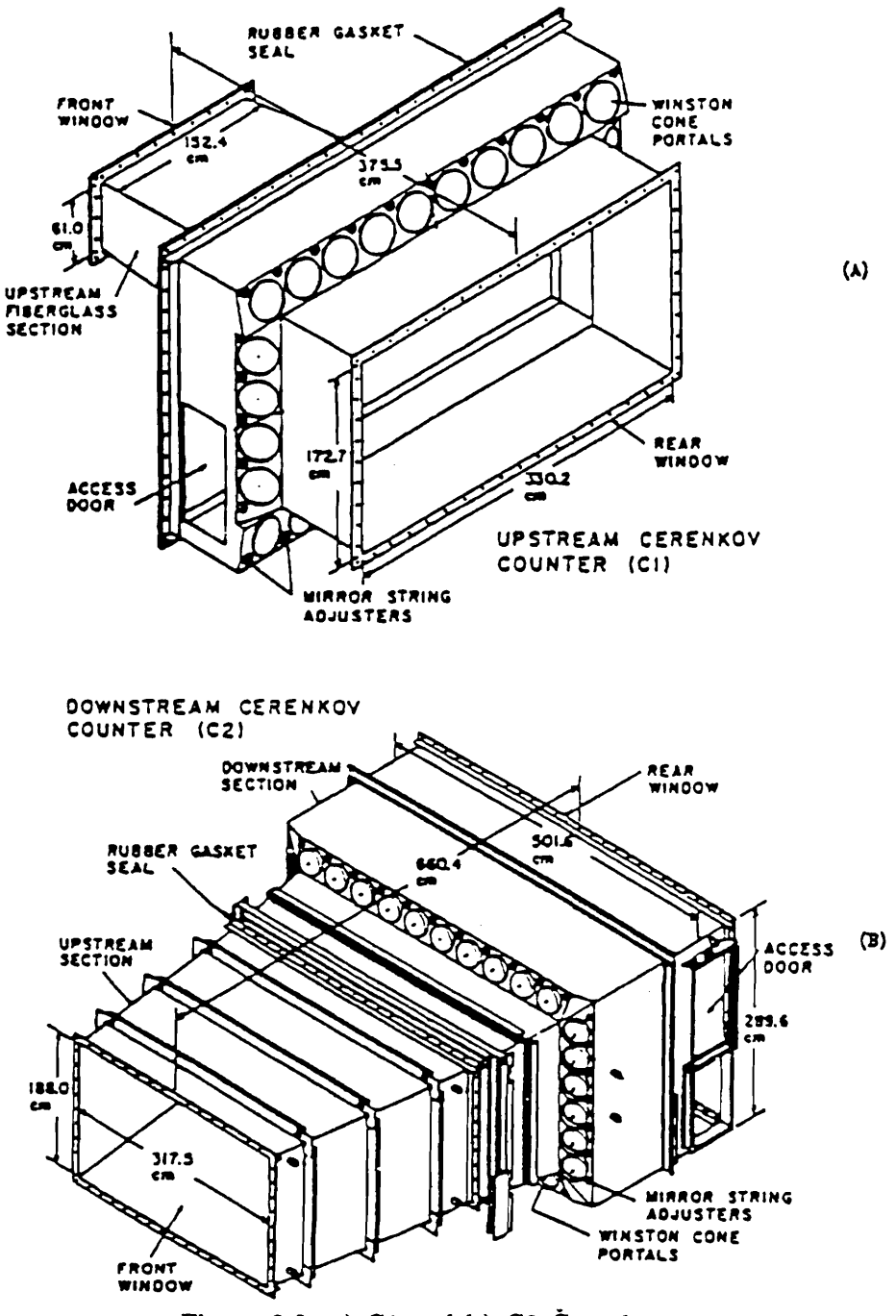

Figure 2.8: a) C1 and b) C2 Čerenkov counters.

2.3.6 Electron Calorimetry

The SLIC

Electromagnetic calorimetry was provided by the Segmented Liquid Ionization Calorimeter, or SLIC for short. Located behind the most downstream drift chamber assembly, D4, the SLIC measured energy deposition by electrons and photons in three views. The narrow shape characteristic of EM showers also gave a means of separating electrons and photons from charged hadrons.

The SLIC is composed of sixty layers of corrugated aluminum panels, coated with teflon, and separated by sheets of lead. The whole assembly resides in a tank filled with NE235A, a liquid scintillator. This is shown in Figure 2.9. Each corrugation is one channel. The twenty planes devoted to each view alternate in the order u, v, y. The light produced in a given channel by a particle crossing the SLIC propagates to the end of the corrugation by total internal reflection (the teflon having a lower index of refraction than the NE235A, any ray incident at $\geq 20°$ stays within the channel). At the end of each channel, the scintillator light is picked up by a waveshifter bar (doped with BBQ), which integrates the light output through the depth of the apparatus. This bar absorbs light in the blue-UV region, and emits in the green, a frequency range more suitable for the phototubes employed. The waveshifter bars themselves are 3.2 cm wide in the center of the SLIC, and 6.4 cm wide (two channels read out together) at the less densely populated outside regions. The center strips are read out using 2″ RCA 4902 phototubes, while the outside ones are read out by 3″ RCA 4900 tubes.

There are 116 y measuring strips, half of which are read out to either side of the SLIC. All 109 u channels are read out from the top. The 109 v strips are read out from the bottom. Various other physical parameters of the system are given in the following table:

width (cm)	487.7
height (cm)	243.8
depth (cm)	121.9
# of layers	60
# of channels/view	109 (u,v) 116 (y)
Thickness of Pb layer (cm)	0.317
Thickness of NE235A layer (cm)	1.27
Total # of radiation lengths	21.5
Total # of nuclear interaction lengths	2.1
vertical acceptance (mrad)	±66
horizontal acceptance (mrad)	±133

Table 2.5: Parameters of the SLIC (from [21]).

The PMT output was digitized by LeCroy 2280 12-bit ADCs. Calibration was done using muons from various sources, as well as e^+e^- pairs produced by photon conversion. It was found that one 3.2 cm channel contains $\sim$ 60% of the total shower energy for an electron, with the totality almost completely contained in 5 channels. Shower centroids can be resolved to within 3 mm. The energy resolution is approximately $21\%/\sqrt{E}$, where E is in GeV.

The Pair Plane

In order to protect the central region of the SLIC from beam photons and e^+e^- pairs (which would cause much background noise) an assortment of 19 lucite shower counters, designed in part to shield the electromagnetic calorimeter from these copious pairs produced from the γ beam, was mounted at beam level. The ones closest to the beam axis are tungsten-lucite, and are 6.35 cm wide. Ones farther out are lead-lucite, and are twice as wide. The total assembly is 12.5 cm high (since there is little y-dispersion) and 174 cm wide (to take into account the spread in x caused by the magnets).

This plane of counters is 20 radiation lengths thick. Another 10 radiation lengths are added by the presence of a plane of lead bricks stacked behind the counters. The pulse heights are digitized by 2249 ADCs, but are not included in the calorimetric reconstruction.

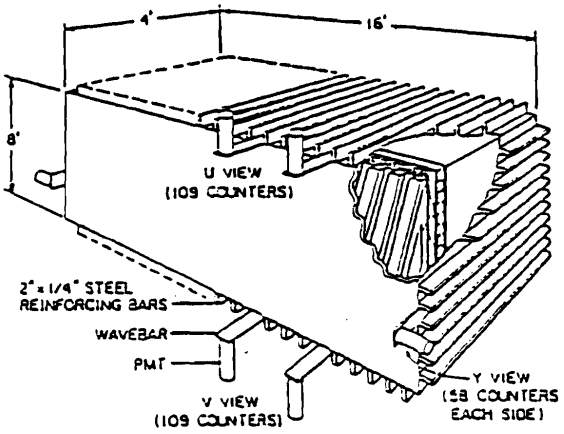

LEAD/LIQUID SCINTILLATOR SHOWER COUNTER (SLIC)
(SCHEMATIC)

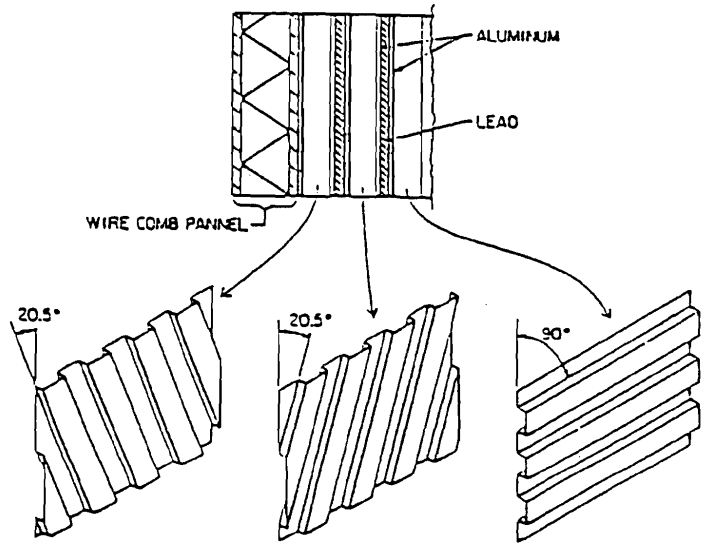

Figure 2.9: Cutaway view of the SLIC and layering diagram.

2.3.7 Hadronic Calorimetry

The Hadron Calorimeter, referred to as the Hadrometer, is located just downstream of the SLIC, and resembles it in some design and operation characteristics (such as its strip geometry and phototube readout). Divided into two sections in the z direction by a 5 cm air gap, each half consists of nine alternating layers of steel and scintillator. There are 33 channels in the x view, and 38 channels in the y view, all 14.5 cm wide. As in the SLIC, for a given strip, the output of the nine layers in each half are integrated by means of a light guide. The following table gives some other physical parameters:

width (cm)	270
height (cm)	490
# of layers	18
# of channels/view	66 (x) 76 (y)
Thickness of steel layers (cm)	2.54
Thickness of scintillator layers (cm)	0.95
Total # of radiation lengths	52.8
Total # of nuclear interaction lengths	5.9

Table 2.6: Parameters of the Hadrometer (from [21]).

A cutaway view of the Hadrometer is shown in Figure 2.10. The light produced by the scintillator was shifted into the visible region. Each acrylic light guide was attached to a EMI 9791KB phototube. The tube outputs were digitized by LeCroy 2280 ADCs, where the gains were calibrated to be 20 counts/GeV. The overall energy resolution of the Hadrometer was $75\%/\sqrt{E}$, with E in GeV, which did not allow for effective detection of hadronic neutrals. The Hadrometer did play a role in various triggers, however, as will be explained later.

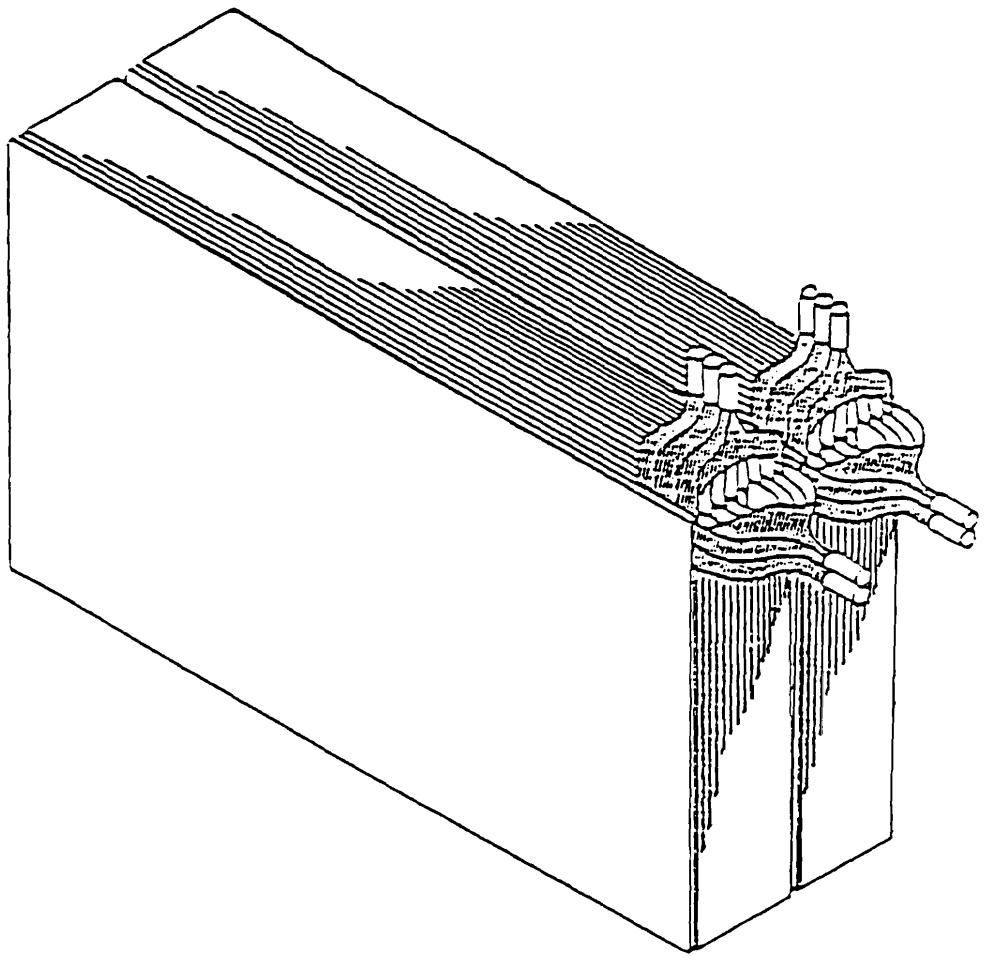

Figure 2.10: Cutaway view of the Hadrometer.

2.3.8 Muon Detection

There were two "walls" at the Tagged Photon Laboratory dedicated to observing muons. The most upstream one, the front muon wall, was located just inside the entrance to the experimental hall. It consisted of eight large scintillator slabs ($\sim$ 46 cm $\times$ 122 cm or $\sim$ 46 cm $\times$ 244 cm) with lucite light guides, and was insulated behind a concrete wall. The slabs were $\sim$ 46 cm thick.

At the rear of the hall, behind the Hadrometer, rested the back muon wall. This wall consisted of 15 slabs of scintillator (46 cm or 61 cm wide) measuring muon position in the x view only. The assembly was separated from the Hadrometer by $\sim$ 100 cm of steel. This sufficed to stop all hadrons completely as well as muons having energy less than 5 GeV. The scintillator light was guided via lucite lightpipes to 5″ EMI 9791KB phototubes. The outputs of these tubes were discriminated and latched. The discriminator output also stopped a TDC, by whose reading the y position of the muon could be determined. The anticoincidence of the two muon walls composed part of the trigger used for studying the decay $J/\psi \rightarrow \mu^-\mu^+$. The two walls in coincidence were used to provide triggers for drift chamber calibration.

The efficiency of the Back Wall was determined by demanding triple coincidence between a counter and two scintillators placed behind it. This efficiency averaged around 94%.

2.3.9 The Triggers

There were two types of triggers, E_t and $TAGH$, used to accumulate physics events during the E691 run, shown schematically in Figure 2.11. The outputs of the electron tagging hodoscope, the B-counter and the Hadrometer formed the inputs of both. The tagging hodoscope at the entrance of the TPL would produce a TAG if a high energy γ had been produced. The small B-counter located behind

the target produced a signal if an interaction had occurred. Energy deposition in the calorimeters (H) constituted the third component.

The hadronic tag trigger ($TAGH$) consisted solely of a logical AND between the interaction counter and a minimum energy deposition of 40 GeV (H_{lo}) in the calorimeters:

$$TAGH = B \bullet H_{lo}$$

Monte Carlo studies suggested, however, that charm content could be enhanced if high transverse energy were made a requirement. This lead to the development of the high transverse energy trigger (E_t). More sophisticated than $TAGH$, the E_t trigger required (if the data acquisition system was not BUSY), in addition to $\sim$ 2.2 GeV transverse energy, either a good $TAGH$ with a good TAG, or a $TAGH$ with a minimum energy deposition of 70 GeV (H_{hi}) in the calorimeters. Both of these combinations had to be accompanied by a pulse from the C1 Čerenkov counter dynodes, in order to eliminate false events caused by stray muons from neighboring beam lines. During the run, $TAGH$ was employed mainly to determine the efficiency of the E_t trigger. H_{hi} was used for high x_F charm where Feynman-x, or x_F, is the ratio of a particle's momentum in the beam direction to its total momentum: $x_F = p_z/p$.

The quantity H was obtained by performing a weighted sum of the SLIC and Hadrometer dynode signals. The SLIC outputs were attenuated by 12 dB relative to the hadronic calorimeter output. The weighting necessary in order to obtain the transverse energy was accomplished by varying the weights attributed to each input of LeCroy 628 fan-in/fan-out modules. The E_t output from the calorimeters was fed into a charge integrator, and this quantity was discriminated in order to get H.

The output of the B-counter was discriminated between one and two minimum

ionizing particles. Approximately 87% of the raw data was taken with the E_t trigger

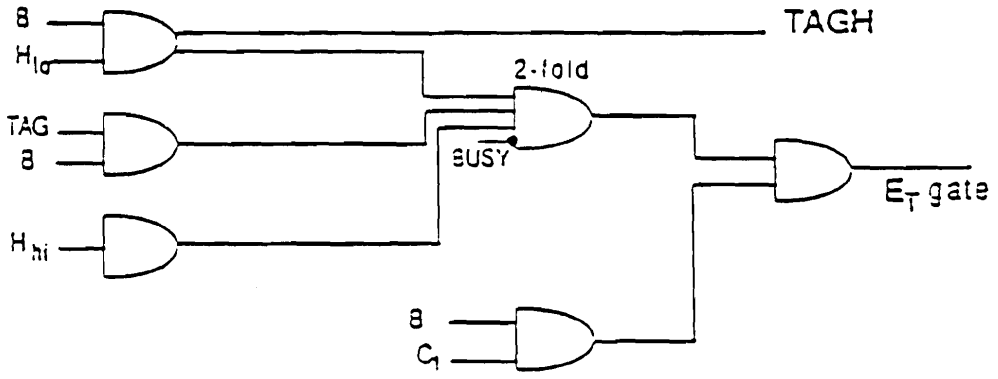

Figure 2.11: Logic diagrams for the $TAGH$ and E_t triggers.

2.3.10 The Data Acquisition and Monitoring Systems

Once a positive trigger had signaled a desirable event, the detector outputs had to be collected. This task, which entailed writing 10^8 events to tape over a period of five months, was handled by the E691 Data Acquisition (DA) system. An on-line monitoring system (OLMS) provided a check on the quality of the events being organized and written by the DA.

Two computers dedicated to acquisition and monitoring were located at TPL, a PDP 11/55 and a VAX 11/780. Actual data collection was handled by the PDP 11/55. All the CAMAC crates (containing all the ADCs, TDCs and latches responsible for digitizing the spectrometer output) were located on two branches, each with its own Jorway 411 branch driver. The drivers were connected to the PDP via a UNIBUS dataway. A Storage Technology Corporation (STC) 1921 tape drive (operating in 6250 bpi, 75 ips mode) and a bipolar memory unit were also on the dataway between the CPU and the Jorways. This is illustrated in Figure 2.12. The actual DA rate was $\sim$ 100 events/sec with a 30% deadtime.

The OLMS operated on the VAX 11/780. A DR11-W high-speed link between the PDP and the VAX provided a data transfer rate of hundreds of kbytes per second, allowing practically immediate on-line monitoring of 10-20% of the events acquired by the PDP. The OLMS depended on two aspects of VMS (the VAX operating system) in order to function. The first is the possibility of having a global section, an area of memory accessible to all processes running on the machine. The second is the existence of detached processes, which can exist and run independently of the log-in status of any particular user. The data obtained by the VAX from the PDP was placed in a global section called the "Event Pool". The Pool was assembled and updated by a detached process called the "Event Pool Builder" (EPB). The Event Pool was monitored and analyzed by various detached analysis

processes (DAPs) created by users. There existed control and display programs (CDPs) which provided an interface between users and DAPs. The advantage of this system is that any number of DAPs could be run independently and asynchronously, permitting monitoring of any of the detectors. This structure is shown in Figure 2.13. In this way, the spectrometer could be monitored in its entirety at all times.

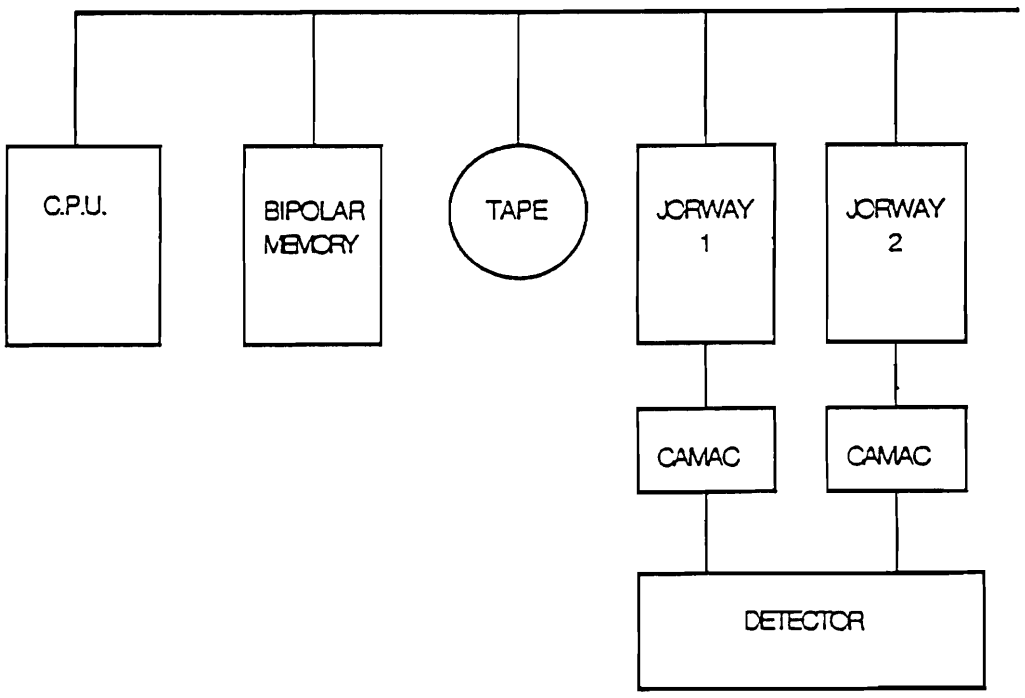

Figure 2.12: Logical Organization of the E691 DA System.

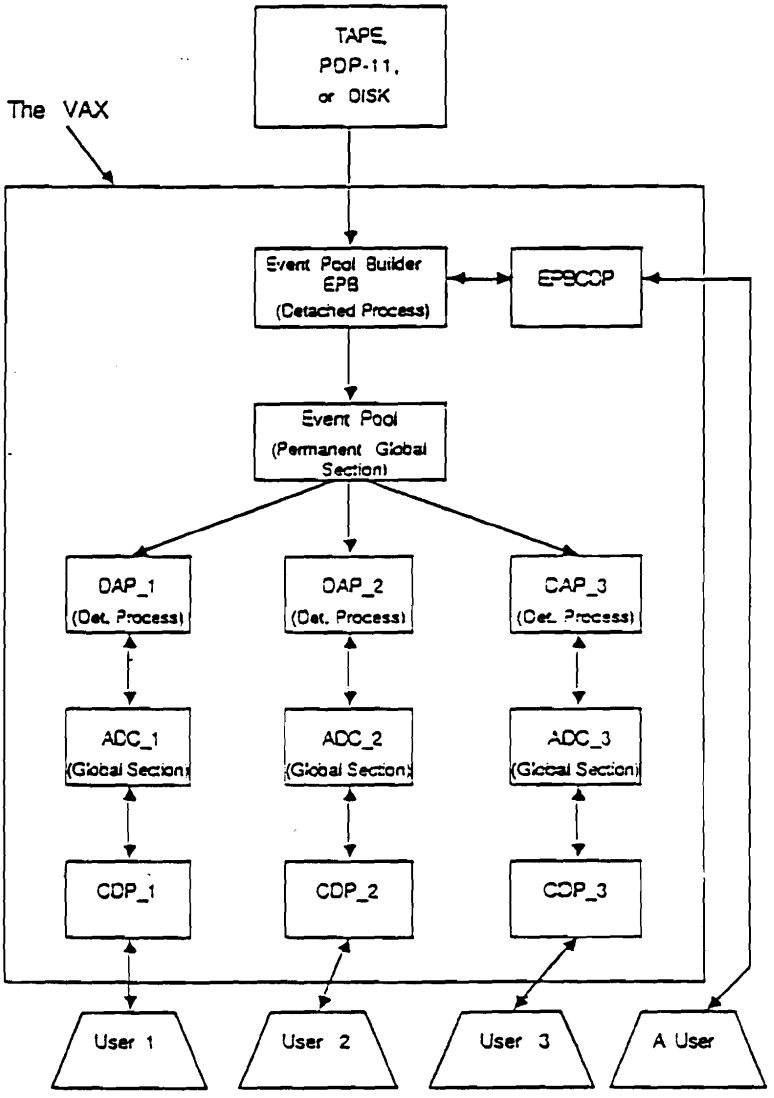

Figure 2.13: Logical Organization of the E691 Online Monitoring System.

Chapter 3 Reconstruction

After the E691 run was completed, the output totaled 10^8 events written onto roughly 2000 6250 bpi, 9-track tapes. The raw data stored in this manner consisted of the outputs from the detectors described in the last chapter from the physics triggers, or calibration events. In order to extract meaningful results, detector information had to be converted to physical quantities such as energy-momentum 4-vectors. This was accomplished by running the reconstruction algorithms detailed below.

3.1 Hardware

Initial reconstruction took place on the CYBER 175 at Fermilab. Complete reconstruction of an event on this machine took $\sim$ 1 s of CPU time, implying that the full data sample would require $\sim$ 3 years to analyze, with a dedicated CYBER. Since no practical (efficient) off-line filter could be devised, each and every event of the data set had to be treated. The fairly small memory available on the CDC, 300,000 octal words, also made coding an arduous task.

A solution to this problem was found in the form of the then-new Advanced Computer Program (ACP), then under development at FNAL. The ACP is one type of "parallel processor", where a microvax controls and directs the functions of a number of nodes, all of which work independently of each other. The nodes are composed of 32-bit Motorola 68020, or ATT 32100, CPUs, with co-processors for floating-point operations and two Mbytes of RAM chips, all loaded onto a VME board. Each node has 0.7 the processing power of a VAX 11-780. The nodes communicate to the microvax via a Q branch bus. Given that high energy interactions are mutually independent, the ACP is very well suited to event reconstruction. A

more detailed description of the ACP be found in [21].

With a 120 node ACP system dedicated to E691, reconstruction of the full data sample took about a year. The advent of the ACPs freed the CYBER for analysis purposes. All in all, about half of the CPU time taken up by the experiment was spent on the CDC machine.

3.2 Software

Originally due to space limitations on the CYBER, reconstruction was divided into two phases, or passes. The first phase, Pass 1, dealt with identifying tracks based on SMD and drift chamber information. Calorimetric and Čerenkov analysis, as well as vertexing, were done in Pass 2. On average, Pass 1 took 0.7 s of CYBER 175 CPU time per event, while Pass 2 took 0.25 s per event on the same machine.

3.2.1 Pass 1

The first pass of the reconstruction invokes two subroutines, S1234 and SESTR, in order to accomplish overall tracking. S1234 is called first and finds tracks based on hits in the SMD detector and projects them downstream through the spectrometer. The high resolution of the silicon planes, as well as the high redundancy of the x, y and v views (3 for each), permit greater track reconstruction efficiencies than by starting with drift chamber hits.

Tracks with six hits in two views are considered first. This "pre-track" is then projected into the third view. Thus, tracks with 3, 2 or 1 hits in the third view (9, 8, or 7 hits total) are selected. Tracks with fewer hits are then examined in the following order: 3-2-2, 3-2-1, 2-2-2. If a track candidate has less than three hits in a given view, it is projected into D1 for a match-up. Once all candidates have been defined with SMD and D1 hits, they are projected through M1 and M2,

using the single-bend approximation, into the D3 y view, as this chamber was less congested than D2. The y view was employed since there is not much appreciable bending in the y direction. At this stage, space triplets (x, u and v) are matched up. The x of the triplet is thus a measure of the magnetic deviation of the track.

Once the track had been projected through the entire spectrometer, and all the drift chamber triplets determined, a momentum fit was performed using these triplets, as well as the field maps for both magnets. This accomplished, quality cuts were applied: a track was discarded if it had too few SMD hits, a bad χ^2/d.o.f. from the momentum fit, or had too many hits in common with another track. The overall tracking efficiency was greater than 90%. S1234 took 0.5 CYBER cpu seconds on average per event.

The second routine to be called, SESTR, essentially did the same as S1234, except that it dealt only with left over drift chamber hits, forming tracks from triplets not used up by tracks having SMD hits. This enabled the detection of longer lived particles. SESTR took less time than S1234, only 0.2 s per event. Arrays containing hit position information are filled at this point.

The spectrometer as a whole was divided into four regions, characterized by the drift chambers. This is shown in Figure 3.1. After the tracks had been reconstructed, the data was stored in a common block (called TRACKS) in arrays detailing track parameters in x and y for each region. The tracking program filled a five-bit word: JCATSG. Depending on whether or not a track existed in region n, S1234 filled the n^{th} bit in JCATSG. The fifth bit was reserved for signaling bad tracks. For example, if a track had only gone through the SMDs, but not D2, one would have JCATSG = 1. A "perfect" track would thus have JCATSG = 15. A track would have to have $7 \leq$ JCATSG ≤ 15 in order to have Čerenkov information, etc. In this way, the quality of tracks could be checked during analysis.

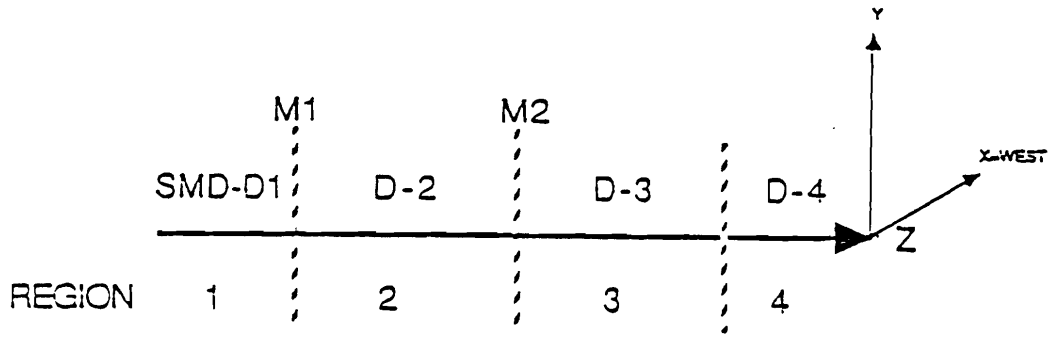

Figure 3.1: Track reconstruction regions at TPL.

3.2.2 Pass 2

SLIC Reconstruction

Data from the SLIC was reconstructed by means of a complex algorithm, in order to determine and properly assign particle energies. Details may be found in [24].

The first step was to find showers in the counters. Any group of contiguous counters in a given view having an energy deposition above 75 MeV were grouped together into "cells". Since the showers of several particles can overlap in one cell, "sectors" inside these cells were found by looking for counters that contained significantly more energy than their nearest neighbors. This did not preclude the possibility of a cell containing only one sector, although a maximum of 80 was allowed for. The centroid of each sector was calculated from three counters, taking into account the expected transverse shape of electromagnetic showers.

After a list of candidate sectors had been established, a fit was performed on the

counter energies to determine which were statistically significant. This also divided the total cell energy among the sectors in a meaningful way. The transverse energy distribution of each sector was fit to either a Monte Carlo electromagnetic shower shape, or a broader hadronic one to determine its origin.

At this point, a list of candidate particles was generated (among those uvy triplets whose v,y pairs predicted the u position) by another fit, as well as their energies and energy errors. Hadronic showers were handled by not only comparing shapes with Monte Carlo predictions, but by checking to see if there was any corresponding energy deposition in the Hadrometer.

After a suitable list of particles had been arrived at, π^0s were reconstructed from 2γ combinations. These had to have the correct mass, have $E_\gamma \geq 2$ GeV and pass a SLIC probability cut. The efficiency for reconstructing π^0s in the decay $D^0 \rightarrow K^-\pi^+\pi^0$ was on the order of 15%.

Čerenkov Reconstruction

Particle identification is supplied by reconstructed data from the Čerenkov counters. The algorithm responsible for this essentially correlates light seen in a counter phototube with particle tracking information [25].

The first step in this process is to determine the number of photons seen by a PMT in a given cell. The measured number of photoelectrons originating from each mirror, NMEAS, is obtained from the raw ADC count from the corresponding tube by subtracting the pedestal and dividing by the expected number of counts produced by a single photoelectron:

$$\text{NMEAS} = \frac{\text{ADC} - \text{PED}}{\text{SPEP}}$$

where SPEP is the single photoelectron peak value. The PEDs and SPEPs are obtained from calibration measurements involving a weak laser light source. Since

in reality more than one track can throw light on a mirror, a light sharing scheme was implemented. Reconstructed tracks are projected through both C1 and C2, taking into account the field inside the former. As the momentum is known, a prediction is made as to which mirrors will be hit by a track's radiation. Thus, a geometrical factor can be calculated for the fraction of light produced by the j^{th} track that will fall into the k^{th} mirror (F^{geo}). This factor also depends on what mass is hypothesized for the track. All sources of inefficiency (such as cracks between the mirrors, imperfect reflectivity, etc.) are taken into account when determining F^{geo}. The phototube output must also be modified by a factor $F^{rad}(\beta)$ to take into account the fact that the tracks do not have $\beta = 1$:

$$F^{rad}(\beta) = 1 - \left(\frac{p_{th}}{p}\right)^2$$

Note that for an infinite momentum track $F^{rad} = 1$, and is independent of the supposed mass of the particle. A final factor is the average number of photoelectrons expected from a cell for an infinite momentum track, $\overline{\mathrm{PE}}$. The predicted number of photoelectrons from a given cell for a given track with a certain mass hypothesis is thus:

$$\overline{\mathrm{NPRED}}_{mass,track,cell} = \mu_{i,j,k} = F^{geo}_{i,j,k} \times F^{rad}_{j,k} \times \overline{\mathrm{PE}}_k$$

Usually the light from a given track is distributed between one to four mirrors, and the outputs of the corresponding cells are summed over when calculating identification probabilities. In the event that one or more tracks share some set of mirrors, only mirrors uniquely associated with a given track are summed over. This procedure works for about 85% of cases. When two tracks are confused, an *a priori* probability, described below, is assigned.

The next step is to calculate and assign probabilities for an i^{th} mass hypothesis to the j^{th} track. Each phototube response is approximated by a compound Poisson

distribution [25]. The overall probability distribution function (PDF) for all the PMTs in a given mirror set is of the form:

$$P_{i,j}(N,\mu,b) = \frac{\mu^N}{N!}(1+b\mu)^{-N-1/b} \times \prod_{m=1}^{N-1}(1+mb)$$

where N is the measured number of photoelectrons in a given (non track-sharing) mirror set, μ is the mean predicted number of photoelectrons in this same set, and b is the mean width of the distributions for this set of phototubes:

$$N = N_j = \sum_k N_{j,k}$$

$$\mu = \mu_{i,j} = \sum_k \mu_{i,j,k}$$

$$b = \overline{b}_{i,j} = \sum_k b_k \mu_{i,j,k}^2 / \mu_{i,j}^2$$

From this PDF, a consistency probability is calculated, using the NMEAS relevant for a given track, as well as the predicted number of photoelectrons, from each counter:

$$\mathrm{PC1}_{i,j} = P_{i,j}(NMEAS_{C1}, \mu, b)$$

$$\mathrm{PC2}_{i,j} = P_{i,j}(NMEAS_{C2}, \mu, b)$$

The overall identification probability, $\mathrm{CPRB}_{i,j}$, is the product of these two functions, times an *a priori* probability APROB_i. This is just the likelihood that a given particle with mass i will be produced in an interaction and recorded by the spectrometer. Thus:

$$\mathrm{CPRB}_{i,j} = \mathrm{PC1}_{i,j} \times \mathrm{PC2}_{i,j} \times \mathrm{APROB}_i$$

The probabilities are normalized such that for a given track, the sum over all possible mass assignments equals unity:

$$\sum_{i=1}^{5} \mathrm{CPRB}_{i,j} = 1$$

Operationally, this identification probability is accessed via an array, CPRB2, where the first index is the track number, and the second is the mass hypothesis. These are ordered in the following way: 1) e, 2) μ, 3) π, 4) K, 5) p. Applying a separate probability cut on each track of a decay is an extremely powerful method of eliminating background, as will be shown in the next chapter.

Vertex Reconstruction

Reconstructing charm decays necessitates being able to resolve distances in the z-direction significantly smaller than $\gamma\beta c\tau$, where τ is the charm lifetime. Similarly, it has been shown that in directions perpendicular to the beam, the resolution must be significantly smaller than $c\tau$ [26]. For a two-body decay, this can be seen simply in the following way. The error on a vertex's z position is roughly given by $\sigma_z \simeq \sigma_0\theta \simeq \sigma_0/\gamma$, where σ_0 is the measurement error on a track's intercept, and $1/\gamma \simeq \theta$ is the half opening angle of the decay. The distance L a particle travels (from the interaction point to the decay vertex) before decaying is $L = \gamma c\tau$, assuming $\beta \simeq 1$. The significance of the detachment in z is thus $L/\sigma_z \simeq c\tau/\sigma_0$. Since this must be as large as possible in order to clearly separate decay from production vertices, the condition $\sigma_0 \ll c\tau$. If one takes $\tau = \tau_{D^0} = 0.44 \times 10^{-12}$ sec, then $c\tau \simeq 100$ μm, greater than the silicon resolution of 16 μm.

The capacity to resolve secondary decay vertices is perhaps the most important aspect of charm detection. This was made possible both by the fine resolution of the silicon microstrip planes and by the vertex finding routines developed to deal with tracks in the interaction region.

The first step in this process is a refitting of all tracks using only region 1 information. This meant simply using SMD hits to refit a track. Once this has been accomplished, all possible two-track combinations are fit to a vertex. If the resulting $\chi^2/d.o.f.$ is less than 3.0, the combination is kept as a "seed" and tracks

are added to it one at a time, forming an n-track vertex candidate. After the addition of a track, the new combination is once again fit to a vertex. As long as the $\chi^2/d.o.f.$ remains under 3.0, the n-track candidate is preserved. If the addition of an $(n+1)^{th}$ track causes the $\chi^2/d.o.f.$ to exceed 3.0, however, this new track is not added to the existing vertex candidate, and the next track on the track-list is used. When all tracks on the list have been used the algorithm ceases to add new tracks, and the combination is saved as an n-track vertex. The seed pairs in this combination are removed from the seed list, and the algorithm repeats itself for the remaining tracks.

The vertex fitting is accomplished using the least-squares method, where the tracks are constrained to pass through the vertex position. Once all vertices have been found, relevant parameters (x, y, z coordinates and errors, $\chi^2/d.o.f.$, etc.) are placed in arrays in a common block (VTXOUT) for access during analysis. Errors on the vertices, taking into account track errors and scattering, are typically:

$$\sigma_x \simeq 13 \ \ \mu\mathrm{m} + \frac{50}{p(\mathrm{GeV/c})} \ \ \mu\mathrm{m}$$

An example of a reconstructed charm event with two secondary vertices is shown in Figure 3.2. As with Čerenkov identification, vertex quality is a powerful method of eliminating background, as will be shown in the next chapter.

3.2.3 Data Summary Tapes

After the first two reconstruction passes, the raw and reconstructed data for each event were written together to 9-track tape. This doubled the length of an event and essentially doubled the number of tapes required to hold the entire data set. The PASS II output tapes were then condensed to Data Summary Tapes (DST). This was done by running a "DST-maker" program on the CYBER. For every input event in PASS II form, this program eliminated all the raw detector information

and packed the reconstructed data types (*i.e.* tracking and vertex information, calorimetry, Čerenkov identification) into a buffer according to a preset format. This had the advantage of compactifying the data by a factor of two. The Fermilab tape prefix assigned to E691 DSTs was XA.

Since the raw detector information was not required for most purposes, subsequent analysis done on the CYBER could be done straight from DST, permitting a significant decrease in unpacking time per event, as well as a decrease of the number of tape mounts required.

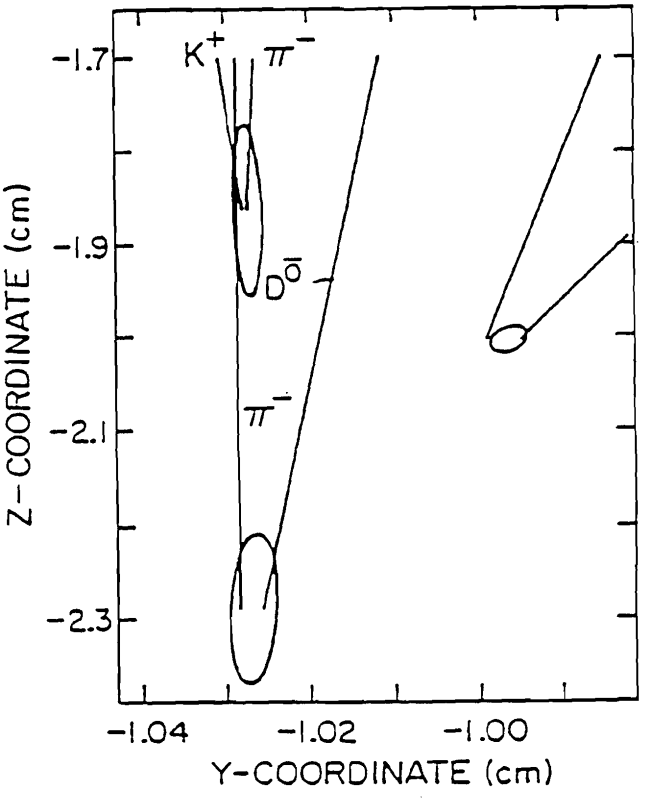

Figure 3.2: Vertices in a charm event.

Chapter 4 Analysis and Results

The following chapter details the analysis required to extract clean signals for the decays $D^0 \rightarrow K^-K^+$, $D^0 \rightarrow K^-\pi^+$ and $D^0 \rightarrow \pi^-\pi^+$.

4.1 Definitions of Fundamental Physical Parameters

Much of the ensuing analysis was carried out by considering events based on their topology and kinematics. There are several quantities worth defining at this stage, due to the frequency with which they form the basis for event selection criteria or "cuts".

SDZ

When analyzing events containing one primary vertex and one or more secondaries, it is useful to be able to select those where the interaction point and the secondary vertices are separated by a given amount. One possibility is to demand that the vertices be separated in z (since in charm events, the decay occurs downstream of the production point) by some minimum value. This does not take into account, however, the potentially large errors associated with the z-positions of both vertices, which may allow them to overlap. A better selection criterion is the quantity termed SDZ, for Significance of Detachment in Z, defined as:

$$SDZ = \frac{z_{secondary} - z_{primary}}{\sqrt{\sigma^2_{zpri} + \sigma^2_{zsec}}}$$

This is illustrated in Figure 4.1. With lifetimes $\sim 10^{-12}$ sec, charmed particles live long enough to travel several millimeters. At γ values of $\sim 15 - 20$, a D will cover $\gamma c\tau \sim 5$ mm before decaying. Thus, demanding that the SDZ between two vertices be high is a good way of eliminating background.

DIP

Another parameter used to select events is the DIP, or "Distance of Impact to a Point", shown in Figure 4.2. This is the transverse distance from a line to a point. Usually, the line is the trajectory of a known particle, either an individual track or the vector sum of tracks. The point is most often a vertex. This is very useful when an event has a secondary vertex candidate. By vectorially summing the tracks composing the secondary, and demanding that the sum "point back" to the primary, *i.e.* placing a maximum value of the sum's DIP with respect to the primary, the validity of the secondary can be established. Cutting on this variable is also a powerful way of determining if a track is part of the primary vertex or one of the secondary vertices.

Ratio

Once the DIP has been defined for a track, the idea can be extended by defining the Ratio parameter for a given track. This is simply the transverse distance of a given track to a secondary vertex divided by the transverse distance of the same track to the primary:

$$\text{Ratio} = \frac{\text{DIP}_{2nd}}{\text{DIP}_{primary}}$$

This parameter should be less than 1.0 for tracks making up a secondary vertex. Therefore, demanding that Ratio $\leq$ 1.0 for all tracks in a secondary vertex candidate is another way of eliminating background. This quantity is illustrated in Figure 4.3.

Setting limits on the allowable values of these quantities enabled successful identification of events containing charm from out of the total data sample.

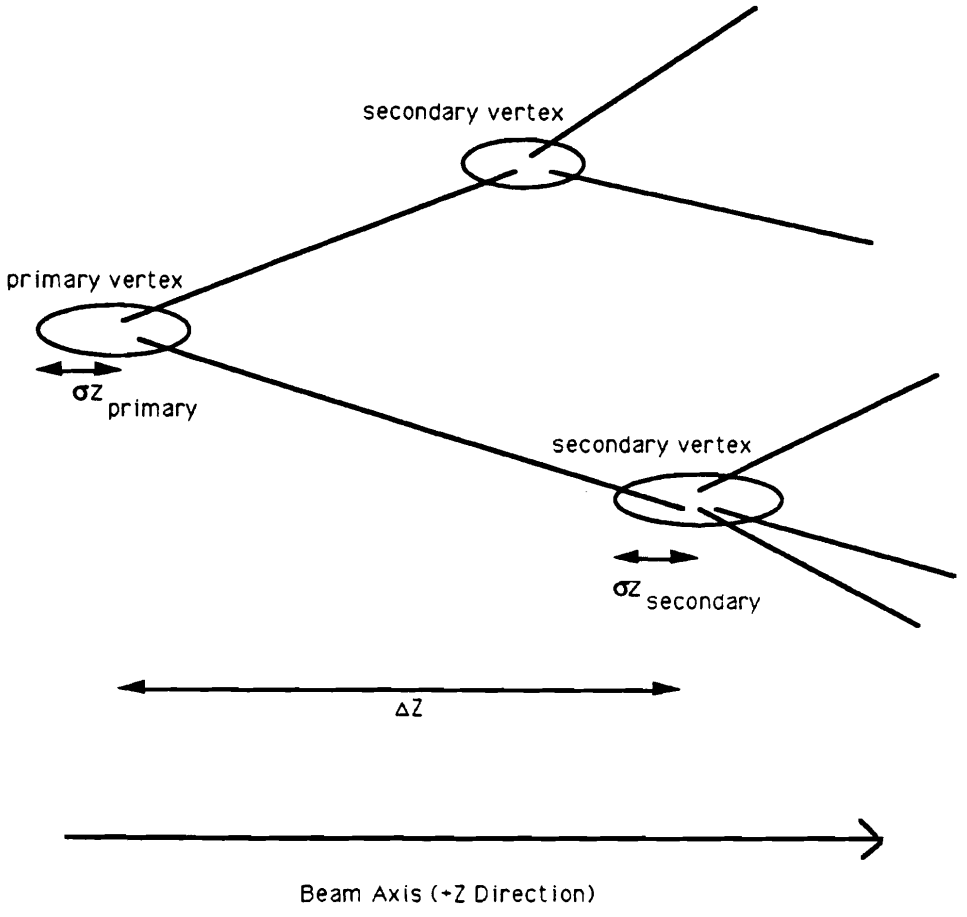

Figure 4.1: Illustration of Significance of Detachment in Z (SDZ).

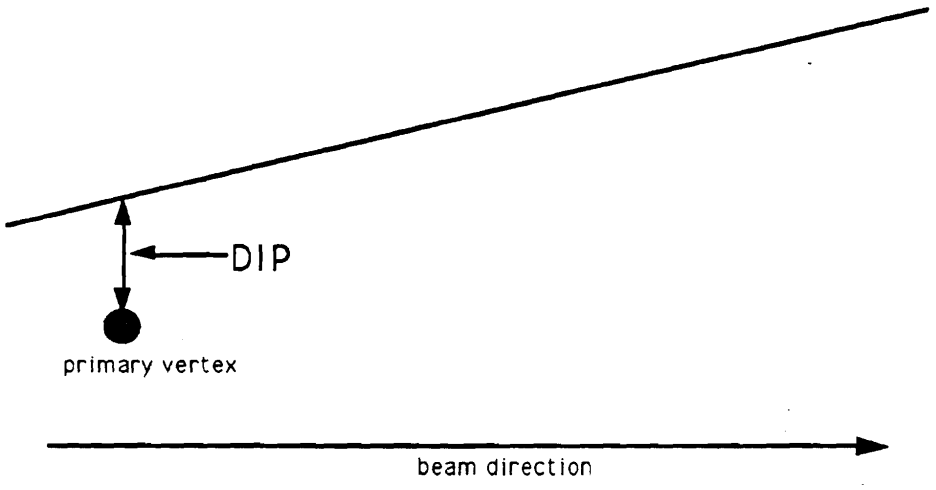

Figure 4.2: Illustration of Distance of Impact Parameter (DIP).

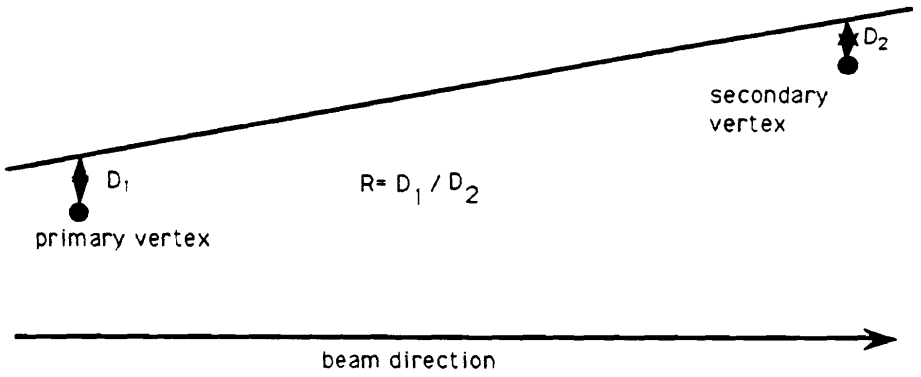

Figure 4.3: Illustration of Ratio.

4.2 The Monte Carlo

The E691 collaboration benefited from a flexible Monte Carlo (MC) package which allowed the simulation of various decay modes. The existence of such a package is crucial in determining the acceptances and efficiencies which affect a true physics signal when recorded by the spectrometer.

The MC is made up of two parts, run as separate batch jobs on the CYBER. The first is the event generator, normally chosen by the user. This subroutine generates the $c-\overline{c}$ pair according to the photon-gluon fusion model [19]. Then, the MC hadronizes the decays. This was accomplished using the Lund fragmentation Monte Carlo package [27]. The output of this section is a list of particle four-vectors, known as the Truth Table. The generator accomplished the following:

- Particle propagation through the spectrometer.
- Pair production.

- Secondary interactions.
- Multiple scattering.

In short, all effects that were the result of the spectrometer's having mass were simulated in the generator.

The next section of the MC, known as the digitizer, consists of simulating the spectrometer and the various detector outputs as the particles travel through them. This part dealt with the following [28]:

- SMD and drift chamber noise and cross-talk. The SMD and drift chamber resolutions were taken into account, as were dead regions.
- The magnetic fields of M1 and M2 were incorporated at first by the single bend point approximation. Later, field maps from the two magnets were used.
- All the regions (baffles) in the Čerenkov counters protected from beam photons and pairs were simulated.
- The Čerenkov counters, SLIC and Hadrometer were all modeled, as was the pair-plane and the muon wall.

The various efficiencies (SMD plane, drift chambers) needed to fully simulate the data were obtained by averaging the efficiencies from sixteen runs.

Once the tracks had been sent through the spectrometer, detector output was simulated. This fake raw data was then reconstructed using the same programs as the real data, discussed in the previous chapter. Monte Carlo output tapes for E691 were given the Fermilab tape prefix XB.

4.3 The Vertex Strip

Following the overall reconstruction of the E691 data and its subsequent storage in DST format, several strips were made in order to enhance the content of events satisfying particular requirements. One strip, for instance, required the presence of an electron among the final state particles (Electron Strip). The Vertex Strip's main requirement, on the other hand, was that there be at least one secondary vertex (presumably due to charm decay) per event. The existence of this secondary was based on information contained in the vertex common block. Furthermore, the strip requires that the secondary have SDZ $\geq$ 5.0. The vector sum of the three-momenta of the tracks composing the secondary vertex had to pass within 200 μ of the production point. The primary vertex was required to be within the target (-6.0 cm $\leq Z_{primary} \leq -1.0$ cm).

These cuts reduced the total number of events from approximately 10^8 to $\sim$ 1.2×10^7. The stripped events were stored on 70 9-track tapes, with each tape containing about 165,000 DST events. These provided the starting data sample for the ensuing analysis.

4.4 Analysis Cuts and Sub-Strips

4.4.1 All Combination Event Selection

In order to maximize the number of potential two-body D^0 decays, all events containing at least one combination of oppositely charged tracks were considered, whether or not such a two-track vertex was listed in the VTXOUT common block. The tracks for these pairs were chosen from the track list in the TRACKS common block. The tracks in the pair were required to have passed through at least one magnet (i.e. $3 \leq$ JCATSG ≤ 15). Once a pair had been selected, it was passed as an argument to a higher level analysis routine.

4.4.2 Higher Level Analysis Cuts

Invariant Mass Cut

The first cut placed on a given two-track combination was a range selection on invariant mass. For a two-body decay, this is calculated by taking the norm of the sum of the two 4-vectors involved in the decay. Since the decays under scrutiny involve only pions and kaons, whose masses are well known, this reduces to a simple 3-momentum scalar product:

$$M^2 = m_1^2 + m_2^2 + 2(\mathbf{p_1}, \mathbf{p_2})$$

In the above, m_1 and m_2 are the masses of the decay particles (in GeV/c^2) and $\mathbf{p_1}$, $\mathbf{p_2}$ are the particle 3-momenta (in GeV/c) as measured in the magnetic spectrometer. The limits on the reconstructed mass varied depending on the decay, but the range was $\sim$ 200 MeV/c^2 about the accepted D^0 mass of 1.865 GeV/c^2. The ranges were chosen in order to include various background features, such as "false peaks" caused by particle misidentification. The actual limits were:

$$1.75 \leq M(K^-\pi^+) \leq 2.00\ GeV/c^2$$

$$1.60 \leq M(\pi^-\pi^+) \leq 2.00\ GeV/c^2$$

$$1.75 \leq M(K^-K^+) \leq 2.05\ GeV/c^2$$

Invariant mass distributions for the decays $D^0 \rightarrow \pi^-\pi^+$, $D^0 \rightarrow K^-K^+$ and $D^0 \rightarrow K^-\pi^+$, with no cuts applied except those from the vertex strip, are shown in Figures 4.4, 4.5 and 4.6 respectively.

Čerenkov Cut

As can be seen from Figures 4.4, 4.5 and 4.6, the background completely obscures any signal peak in the mass distributions. In order to improve the statistical

significance of the signals for the Cabibbo-suppressed modes (defined as $S/\Delta S$, where S is the number of signal events and ΔS is the error on S), positive Čerenkov particle identification was required of both tracks forming the candidate D^0 for both $D^0 \rightarrow K^-K^+$ and $D^0 \rightarrow \pi^-\pi^+$ decays. This amounted to placing a cut on the Čerenkov probabilities calculated during the reconstruction, described in section 3.2.2, and stored in the CKVID common block. Positive identification required cutting above the *a priori* peaks in both the pion and kaon probability distributions:

$$Prob(\pi) \geq 0.84$$

$$Prob(K) \geq 0.40$$

These distributions are shown in Figures 4.7 and 4.8, respectively. Notice the large *a priori* peaks at 0.82 and 0.11 in the π and K distributions respectively. As was stated in the previous chapter, the *a priori* probability is simply the likelihood that a given particle type will be produced in a high energy collision, irrespective of the fact that a track may have radiated in a Čerenkov counter. For kaons, this *a priori* probability is $\sim 11\%$, for pions it is $\sim 80\%$. A continuum of probabilities is produced when tracks which actually do radiate are considered. Thus, cutting above the *a priori* value is equivalent to demanding that a track produce reconstructible signals in the Čerenkov counters consistent with a given mass hypothesis. Another interesting aspect of these distributions is the fact that many pions have an identification probability greater then 90% (hence the large peak at values close to 1.0), while few kaons are known to better than 80% (most are known to at best 75%).

No Čerenkov cut was placed on D^0 candidates for the Cabibbo-allowed $D^0 \rightarrow K^-\pi^+$ decay as it was possible to obtain a signal by just using the other cuts described in this section. The $D^0 \rightarrow K^-\pi^+$ mode was used to calculate the efficiency of the Čerenkov cut for both the $D^0 \rightarrow K^-K^+$ and $D^0 \rightarrow \pi^-\pi^+$ channels. How

this was done is described in the section on efficiencies.

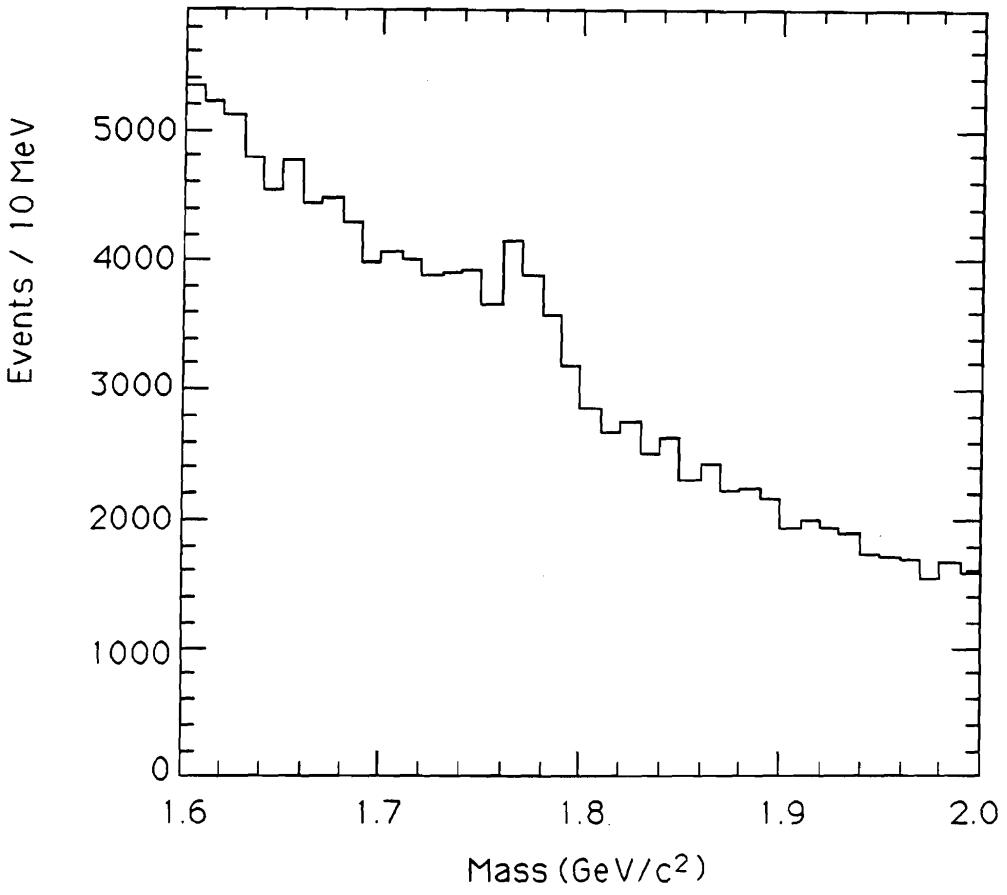

Figure 4.4: Invariant Mass distribution for $D^0 \rightarrow \pi^-\pi^+$ + Charge Conjugate for all two-track combinations from events in vertex strip.

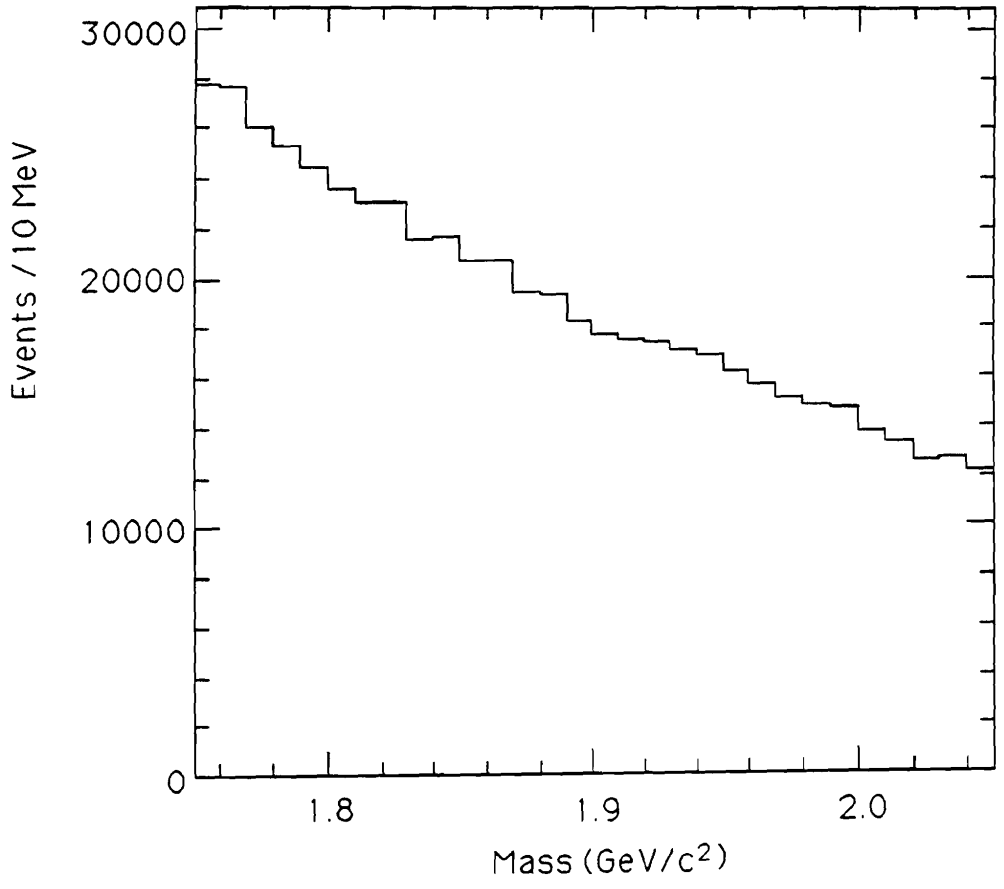

Figure 4.5: Invariant Mass distribution for $D^0 \to K^- K^+$ + C.C..

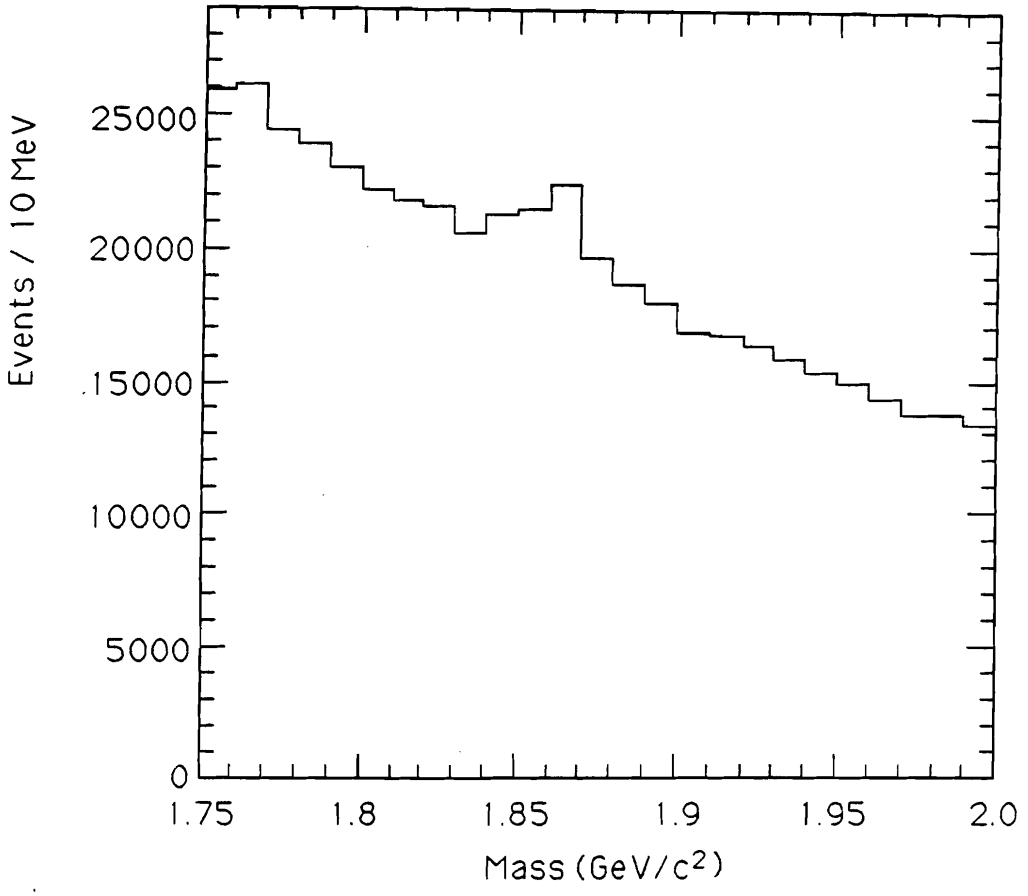

Figure 4.6: Invariant Mass distribution for $D^0 \rightarrow K^-\pi^+$ + C.C..

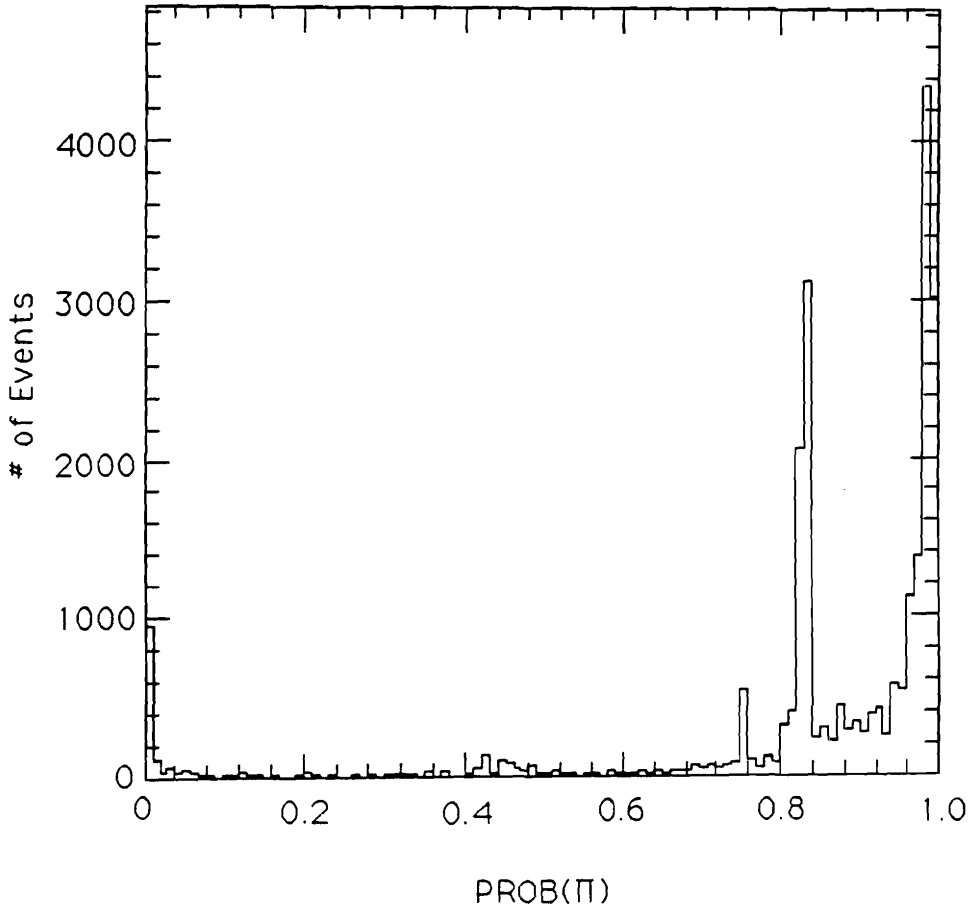

Figure 4.7: Čerenkov probability distributions for pions.

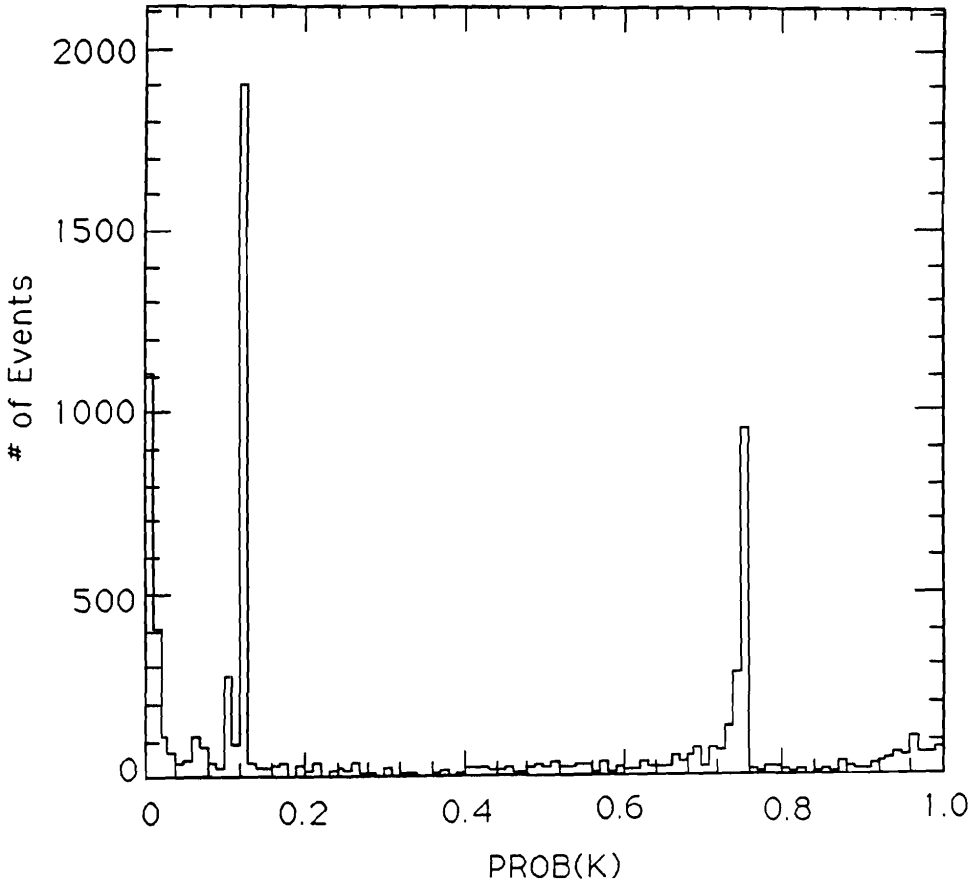

Figure 4.8: Čerenkov probability distribution for kaons.

Revertexing and cut on χ^2 of secondary

Once the decay tracks forming the neutral pair have been identified as kaons and pions to high probability, the combination is "re-vertexed" to determine whether or not the tracks form a good vertex. This is done by the same routine responsible for vertexing during the initial PASS II reconstruction (subroutine VFIT1). The quality of the vertex is judged by the χ^2/d.o.f. returned by the subroutine. A study using MC as well as real data in DST form revealed that the statistical significance of the signal was maximized by demanding that:

$$\chi^2/d.o.f.(secondary) \leq 1.7$$

In this case, the efficiency for this cut is $\simeq$ 90%, while the background rejection is $\simeq$ 35 %. Note that this is a more stringent requirement than that imposed upon vertices for inclusion in the vertex list (where a secondary is included if χ^2/d.o.f. $\leq$ 3.0).

Existence of Primary Vertex

Once the neutral two-track combination was determined to be a plausible D^0 candidate, the event's topology was examined more thoroughly. The 3-momenta of the decay tracks forming the candidate were summed in order to determine the impact parameter (DIP) from all other pre-existing vertices in the vertex list. If there is no vertex for which DIP $\leq$ 80 μm, then the event is rejected. If such a vertex does exist, it is designated the event's primary, and a further requirement is that $Z_{primary}$ be contained within the target boundaries (-6.0 cm $\leq z_{primary} \leq$ -1.0 cm in the E691 coordinate system). Note that this "primary" is not necessarily the same one determined from the PASS II reconstruction algorithm (although they are almost always the same). The efficiency of requiring the existence of such a primary was on the order of 95%.

SDZ Cut

In addition to all the cuts detailed above, a minimum SDZ value of 5.0 was required of the secondary vertex candidate, as this value maximized $S/\Delta S$.

DIP cut

Once the existence of a primary vertex had been established, the tracks composing the secondary were added vectorially, and the resulting sum was extrapolated back to the primary. The DIP between this sum and the primary vertex was then calculated. An event was accepted only if DIP ≤ 80 μm.

Ratio Cut

A cut was applied on the ratio of transverse distances to secondary and primary vertices for both tracks composing the decay vertex (after the existence of a production point had been verified). A study indicated that the statistical significance of the signal was maximized by demanding that the tracks pass at least as close to the secondary as to the primary:

$$Ratio \leq 1.0$$

The efficiency of this cut was on the order of 97%.

Momentum Cuts

Due to the nature of the Čerenkov cut described above, only those tracks were allowed whose momenta lay within the ranges where particle identification by the Čerenkov counters was possible. The efficiency for kaon identification was non-zero roughly for $6 \leq P(K) \leq 70$ GeV/c, while that for pion identification was non-zero for $6 \leq P(\pi) \leq 100$ GeV/c. Track momenta are roughly limited to these ranges.

The exact ranges are described in detail in the following section. On the average, though, momenta for both decay particles (be they pions or kaons) where almost always between 6 GeV/c and 70 GeV/c.

4.5 Efficiencies

The overall detection efficiency ϵ for a given mode was determined to be the product of two contributions:

$$\epsilon = \epsilon_G \, \epsilon_C$$

where ϵ_G is the geometrical, track reconstruction and vertexing efficiency, and ϵ_C is the efficiency due to the Čerenkov cuts.

4.5.1 Geometrical Acceptance and Reconstruction Efficiencies

The TPL spectrometer can be thought of, due to the geometry of the SMD planes and drift chambers/magnets, as instrumenting the inside of a cone of opening angle $\pm$ 100 mrad, the beam direction being coincident with the cone's axis. Strictly speaking, of course, this is not true, since the drift chambers, magnets and Čerenkov counters do not have circular apertures. Since this angular acceptance is fairly uniform over the length of the apparatus, tracks with angles greater than this value will not be accepted into the magnets. An estimate of the number of decays that are actually detected by the spectrometer can be obtained from the Monte Carlo truth table for the decays in question (reconstructed fake MC data will obviously always be composed of tracks with angles less than 100 mrad). Track angle (θ) distributions for pions and kaons are shown in Figures 4.9 and 4.10, respectively, for 1000 generated Monte Carlo events. One can estimate from the following plots that $\sim$ 25% of the decay products will not pass through the spectrometer.

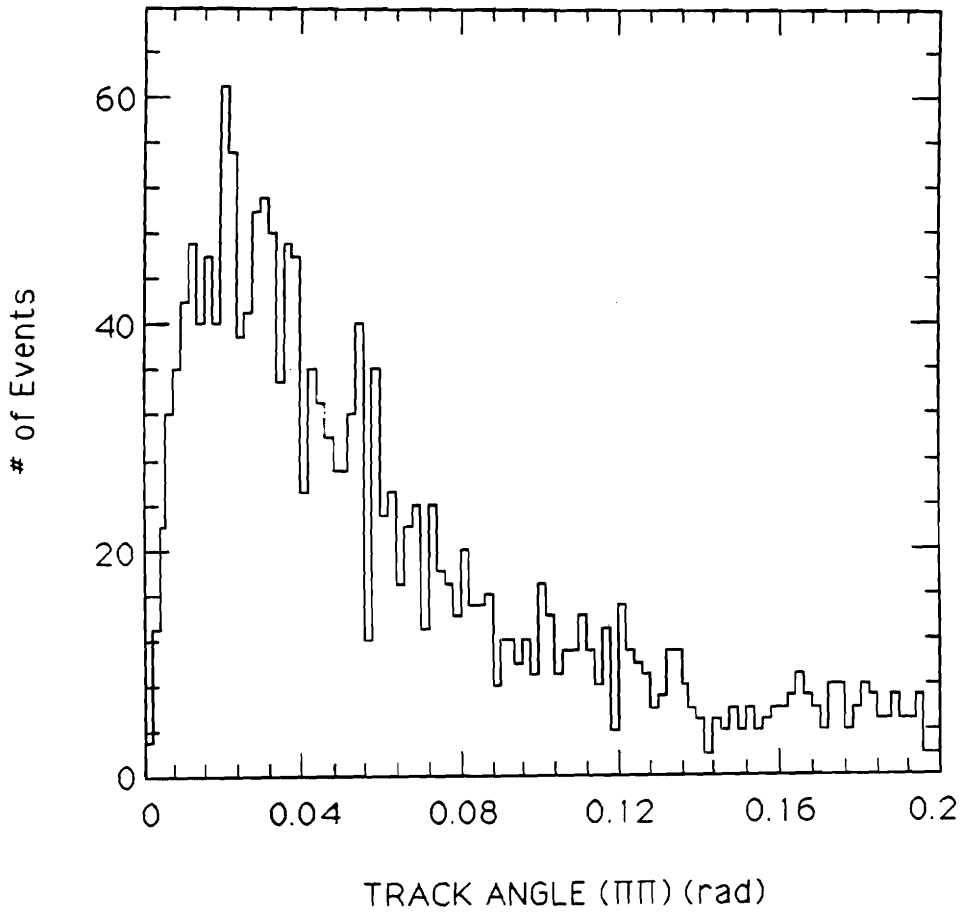

Figure 4.9: θ for pions in 1000 $D^0 \rightarrow \pi^-\pi^+$ + C.C. MC decays.

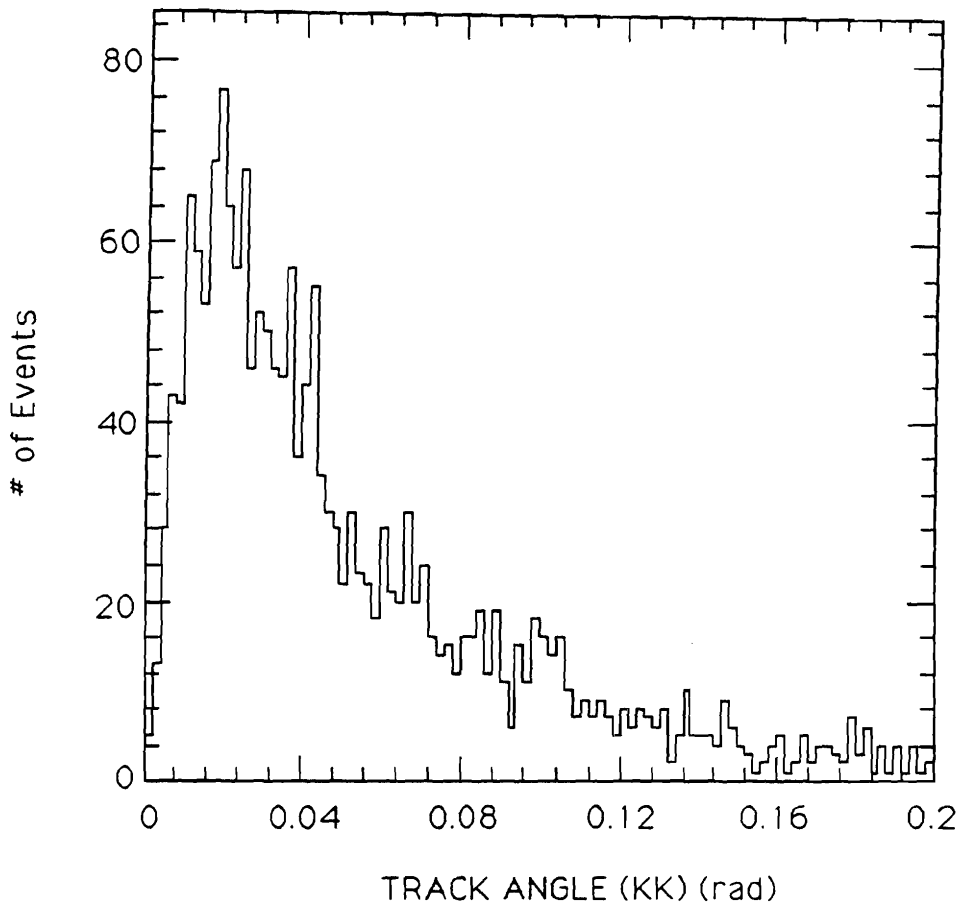

Figure 4.10: θ for kaons in 1000 $D^0 \rightarrow K^-K^+$ + C.C. MC decays.

The reconstruction efficiency ϵ_G was calculated as the product of three factors:

$$\epsilon_G = A_1 \, A_2 \, A_3$$

where A_1 is the geometrical and momentum acceptance for a given mode, A_2 is the efficiency for obtaining a primary vertex, and A_3 is the vertex reconstruction efficiency (this includes the effects of the ratio, χ^2 and SDZ cuts described above). The A_i were determined using fake Monte Carlo data in DST form in the following manner:

$$A_1 = \frac{N_{geo+p}}{N_g}$$

$$A_2 = \frac{N_{geo+p+vpri}}{N_{geo+p}}$$

$$A_3 = \frac{N_{geo+p+vpri+vtx}}{N_{geo+p+vpri}}$$

where the N_j are the numbers of events passing cuts j. In this case, N_g, the number of generated events, was set to 18,000 for all three decay modes.

The Monte Carlo fake data used was available in both DST and PASS II formats. DST formatted MC data was stored as disk files on the CYBER (before that machine's shutdown), while PASS II MC data was written to tape and archived in the Feynman Computing Center tape vault. A list of the MC tapes used for a given channel, as well as the format the data was stored in, is given in the following table. Note that these were the most recent tapes available for their respective modes. There was a gap of five months, however, between the production of the $D^0 \rightarrow K^-\pi^+$ tape and the other two.

Mode	Tape #	Format
$D^{*+} \to \pi^+ D^0 \to K^- K^+$	XB8299	DST
$D^{*+} \to \pi^+ D^0 \to \pi^- \pi^+$	XB8298	DST
$D^{*+} \to \pi^+ D^0 \to K^- \pi^+$	XB8244	DST

Table 4.1: MC data tapes used in the geometrical efficiency study.

Prior to calculating the A_i for all three modes, it was important to determine if all three Monte Carlo tapes had been produced under the same conditions. This refers to ensuring that the various parameters in the generator were kept constant from one tape to another, and that the same constants were used in describing the detector. This was necessary so as not to bias the acceptances towards one particular mode. A comparison of basic event parameters of all three files, however, yielded discrepancies in some characteristics of the MC events between the two Cabibbo-suppressed modes and the allowed channel. The quantities compared were the track multiplicity (contained in the variable IERPM2, in the TRACKS common block), the number of vertices (NVV, in the VTXOUT common block), and the number of tracks composing the primary vertex (NTKV(NPRI), also in the VTXOUT common block), averaged over 18,000 MC events. The results are shown in the following table.

Mode	Tape #	$\overline{IERPM2}$	$\overline{NVV}$	$\overline{NTKV(NPRI)}$
$D^{*+} \to \pi^+ D^0 \to K^- K^+$	XB8299	7.49 ± 0.02	3.50 ± 0.02	4.34 ± 0.015
$D^{*+} \to \pi^+ D^0 \to \pi^- \pi^+$	XB8298	7.38 ± 0.02	3.40 ± 0.02	4.30 ± 0.015
$D^{*+} \to \pi^+ D^0 \to K^- \pi^+$	XB8244	7.91 ± 0.02	3.70 ± 0.03	4.62 ± 0.015

Table 4.2: Comparison of Basic event parameters for MC tapes used.

It is clear that the average track multiplicity for the $D^0 \to K^-\pi^+$ Monte Carlo (and correspondingly, the number of vertices and the number of tracks in the primary as well) is greater than that for the $D^0 \to K^-K^+$ and $D^0 \to \pi^-\pi^+$ simulations. Given the large time gap between the production of the $D^0 \to K^-\pi^+$ tape and the other two, it is likely that an undocumented change was made to the Monte Carlo generator.

This had the effect of raising $A_2(D^0 \to K^-\pi^+)$ relative to $A_2(D^0 \to \pi^-\pi^+)$ and $A_2(D^0 \to K^-K^+)$. In order to correct for this discrepancy, $A_2(D^0 \to K^-\pi^+)$ was taken to be the weighted average of $A_2(D^0 \to \pi^-\pi^+)$ and $A_2(D^0 \to K^-K^+)$. The values for all three modes are shown in the following table.

	$D^0 \to \pi^-\pi^+$	$D^0 \to K^-K^+$	$D^0 \to K^-\pi^+$
A_1	0.299 ± 0.006	0.366 ± 0.007	0.349 ± 0.004
A_2	0.729 ± 0.003	0.729 ± 0.003	0.729 ± 0.002
A_3	0.411 ± 0.019	0.393 ± 0.016	0.381 ± 0.007

Table 4.3: Reconstruction efficiencies and acceptances for $D^0 \to \pi^-\pi^+$, $D^0 \to K^-K^+$ and $D^0 \to K^-\pi^+$.

Hence, the final geometrical efficiencies are:

$$\epsilon_G(K^-K^+) = 0.104 \pm 0.002$$

$$\epsilon_G(K^-\pi^+) = 0.097 \pm 0.002$$

$$\epsilon_G(\pi^-\pi^+) = 0.093 \pm 0.002$$

4.5.2 Čerenkov Efficiencies

Individual particle identification efficiencies

The first step in determining the overall efficiency for the Čerenkov cut is obtaining the individual (K or π) identification efficiencies. The product of the two must then be taken:

$$\epsilon(K^-K^+) = \epsilon(K^-) \times \epsilon(K^+)$$

The efficiencies ϵ_C for individual kaon or pion identification in $D^0 \rightarrow K^-K^+$ or $D^0 \rightarrow \pi^-\pi^+$ decays can be obtained from the respective Monte Carlo in the following manner:

$$\epsilon_C(K) = \frac{N_{K^-K^+}(Prob(K) > 0.4)}{N_{K^-K^+}(Prob(K) \geq 0.)}$$

$$\epsilon_C(\pi) = \frac{N_{\pi^-\pi^+}(Prob(\pi) > 0.84)}{N_{\pi^-\pi^+}(Prob(\pi) \geq 0.)}$$

The Čerenkov efficiencies for K or π can also be measured from the data by comparing the signals $N_{K^-\pi^+}$ for real $D^0 \rightarrow K^-\pi^+$ decays before and after requiring positive particle identification:

$$\epsilon_C(K) = \frac{N_{K^-\pi^+}(Prob(K) > 0.4)}{N_{K^-\pi^+}(Prob(K) \geq 0.)}$$

$$\epsilon_C(\pi) = \frac{N_{K^-\pi^+}(Prob(\pi) > 0.84)}{N_{K^-\pi^+}(Prob(\pi) \geq 0.)}$$

The $K\pi$ pairs come from the decay chain $D^{*+} \rightarrow \pi^+D^0 \rightarrow K^-\pi^+$ [29].

Another complication is the dependence of the Čerenkov identification efficiency on the momentum p of the particle to be identified.

$$\epsilon_C(K) = \epsilon_C(K, p_K)$$

$$\epsilon_C(\pi) = \epsilon_C(\pi, p_\pi)$$

The ϵ_C's can be measured in a set of momentum intervals. The efficiencies are given in the table below:

P range (GeV/c)	$\epsilon_C(\pi), P(\pi) \geq 0.84$	$\epsilon_C(K), P(K) \geq 0.40$
6 - 10	0.34 ± 0.07	0.51 ± 0.07
10 - 20	0.75 ± 0.03	0.83 ± 0.04
20 - 37	0.80 ± 0.02	0.82 ± 0.02
37 - 70	0.74 ± 0.03	0.47 ± 0.03
70 - 100	0.49 ± 0.13	$0. \pm 0.$
100 - 200	0.47 ± 0.25	$0. \pm 0.$

Table 4.4: Čerenkov efficiencies for various momenta for π and K.

Ultimately, the efficiencies obtained from real data were used in the ensuing analysis, as the Monte Carlo data was found to inaccurately model the efficiencies for individual particle identification. The degree to which the MC misrepresented these efficiencies for both pions and kaons varied as a function of particle momentum, but averaged around 10%. A comparison of MC and data efficiencies for pions and kaons for various momentum ranges are shown in Figures 4.11 and 4.12, respectively.

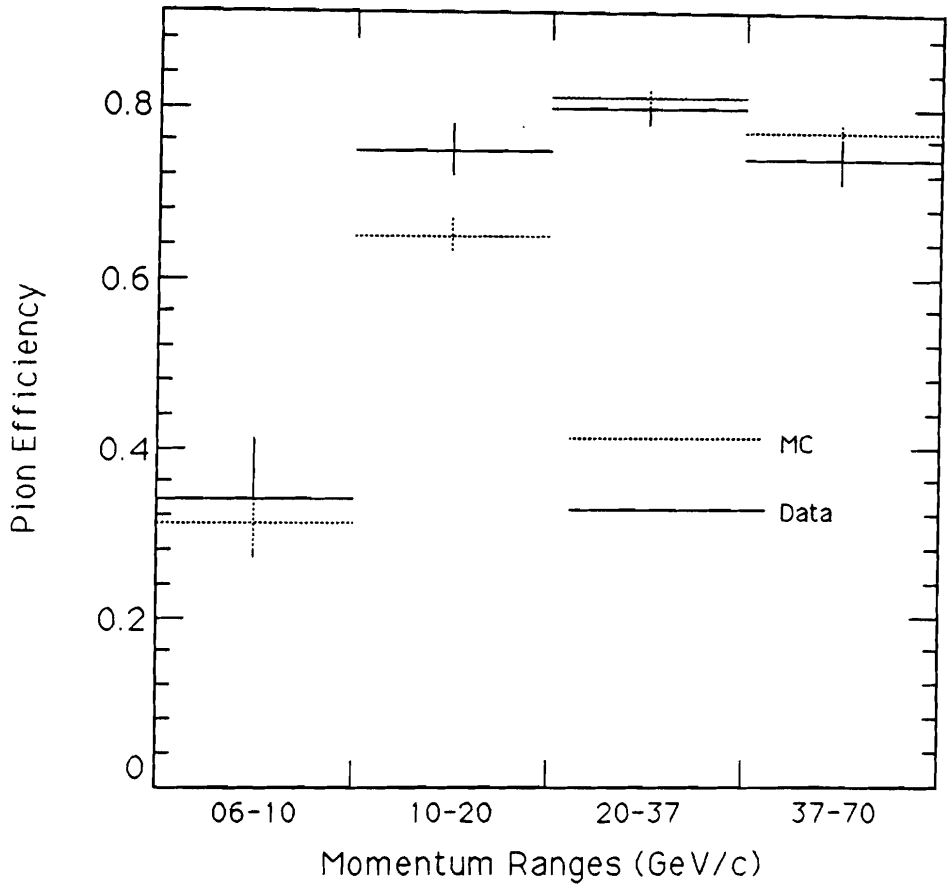

Figure 4.11: Comparison of Čerenkov ϵ for pions between MC and real data.

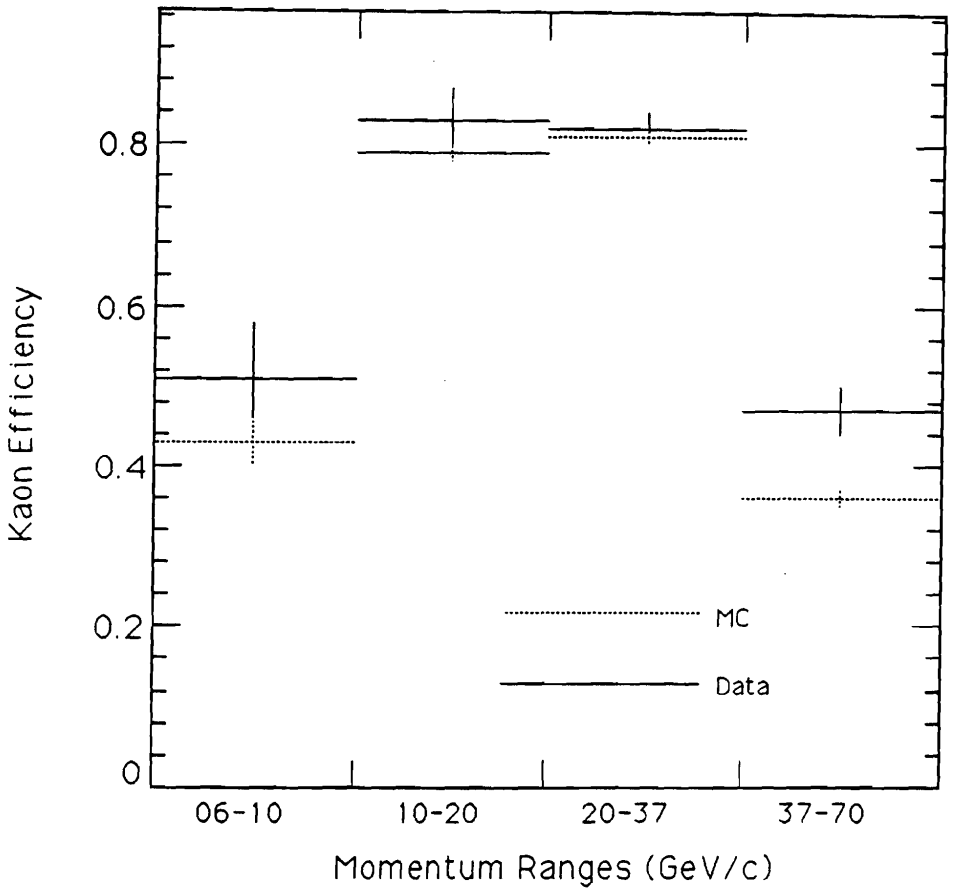

Figure 4.12: Comparison of Čerenkov ϵ for kaons between MC and real data.

Weight matrix formulation for the overall efficiency

Once the efficiencies were determined for K and π identification as a function of momentum, the data was analyzed with the same Čerenkov cut values:

$$Prob(K) \geq 0.4$$

$$Prob(\pi) \geq 0.84$$

As was stated before, the efficiency for identifying a pair of particles is simply the product of the individual efficiencies, e.g.

$$\epsilon(K^-K^+) = \epsilon(K, p^-) \times \epsilon(K, p^+)$$

where p^- and p^+ are the momenta of the K^- and K^+, respectively. In practice, the overall Čerenkov cut efficiency is a weighted average over the whole momentum range of both particles:

$$\epsilon_C(\pi^-\pi^+) = \frac{\sum N_{\pi\pi}(ij)\epsilon_i(\pi)\epsilon_j(\pi)}{\sum N_{\pi\pi}(ij)}$$

$$\epsilon_C(K^-K^+) = \frac{\sum N_{KK}(ij)\epsilon_i(K)\epsilon_j(K)}{\sum N_{KK}(ij)}$$

where the subscripts represent the three-momentum intervals defined above. This required determining the weighting factors $N(ij)$. These are simply the numbers of $D^0 \rightarrow \pi^-\pi^+$ or $D^0 \rightarrow K^-K^+$ decays where the pion and kaons have three-momenta in the intervals i and j respectively. In principle these could be obtained from the plentiful $D^0 \rightarrow K^-\pi^+$ data by fitting mass plots where the momenta of the entries were limited to the appropriate ranges. However, the background inherent in these plots represents an extra source of error. Also, the individual momentum distributions of the kaons and pions in $D^0 \rightarrow K^-\pi^+$ decays need not necessarily match those from $D^0 \rightarrow K^-K^+$ and $D^0 \rightarrow \pi^-\pi^+$ events. Using the

Monte Carlo would vitiate these concerns. In a preliminary comparison of data and simulation, however, it was found that the MC does not completely reproduce the D^0 momentum spectrum. In order to obtain the $N(i,j)$, the MC spectrum had to be corrected. This is discussed below.

Measurement of the D^0 momentum spectrum

The most economical solution was to check the Monte Carlo. The MC three-momentum distribution was compared with the momentum spectrum obtained from real $D^0 \rightarrow K^-\pi^+$ events. The true D^0 momentum distribution was extracted in the following way. With no Čerenkov cut, the $D^0 \rightarrow K^-\pi^+$ data was binned into 15 momentum intervals, the entire range being 6-156 GeV/c, and a mass plot produced for each. A fit yielded the number of signal events N_i in each bin. The geometrical acceptances ϵ_i for each bin were determined from the Monte Carlo. The parent population of each bin is therefore N_i/ϵ_i. A $cos(\theta)$ cut in the D^0 rest frame, discussed in detail below, was employed to reduce combinatoric and wrong-sign background. The cut value was $|cos(\theta)| < 0.8$. A sample mass plot (for D^0 momentum between 46 and 56 GeV/c) is shown in Figure 4.13. The true momentum spectrum is shown in Figure 4.14.

This experimental distribution was compared with the Monte Carlo Truth Table spectrum, where the MC data was binned in a similar manner. Normalizing each distribution (i.e. data and MC) to the contents of an arbitrary bin of high statistics (bin #4) and "dividing" the data spectrum by the MC spectrum bin by bin yielded 15 ratios shown in Figure 4.15. This distribution of ratios was fit by a straight line (limited to regions where there was high acceptance), thereby yielding a momentum dependent parametrization of the correction to be made to the MC momentum spectrum in order to force agreement with the data. As can be seen from Table 4.5, these ratios are all very close to 1.0. The equation obtained from

a straight line fit is

$$R = (0.002728 \times p) \; + \; 0.9263$$

It is evident from the above two parameters that this set of ratios is very weakly dependent on momentum. Moreover, the Monte Carlo spectrum is generally softer (by $\sim$ 10 %) than the data.

P range (GeV/c)	Ratio	Comment
6 - 16	0.0	No acceptance, Not used in fit
16 - 26	0.27 ± 0.73	Not used in fit
26 - 36	0.81 ± 0.17	
36 - 46	1.0 ± 0.13	
46 - 56	1.03 ± 0.09	
56 - 66	1.31 ± 0.11	
66 - 76	1.15 ± 0.11	
76 - 86	1.06 ± 0.11	
86 - 96	1.32 ± 0.15	
96 - 106	1.14 ± 0.16	
106 - 116	1.39 ± 0.22	
116 - 126	0.92 ± 0.21	
126 - 136	1.52 ± 0.48	Not used in fit
136 - 146	2.14 ± 0.92	Not used in fit
146 - 156	2.16 ± 2.25	Not used in fit

Table 4.5: Ratios for given p ranges between $D^0 \rightarrow K^-\pi^+$ data and MC populations.

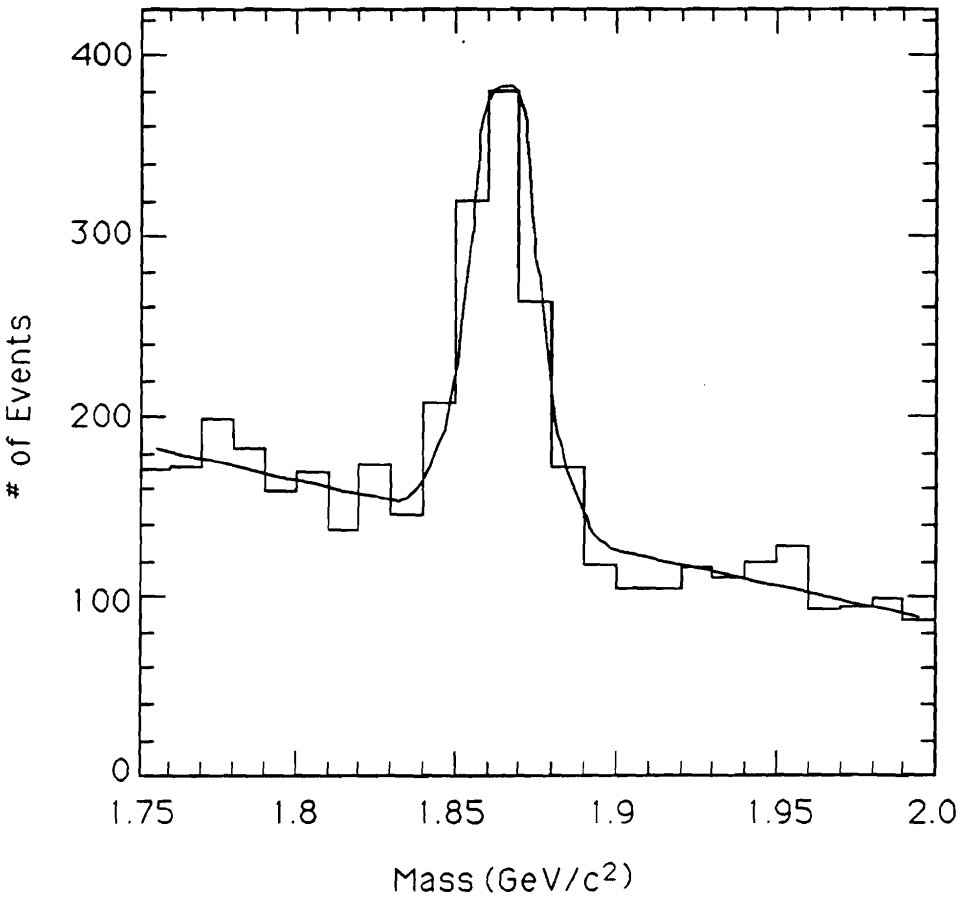

Figure 4.13: $D^0 \rightarrow K^-\pi^+$ + C.C. mass distribution for $56 \leq p(D^0) \leq 66$ GeV/c.

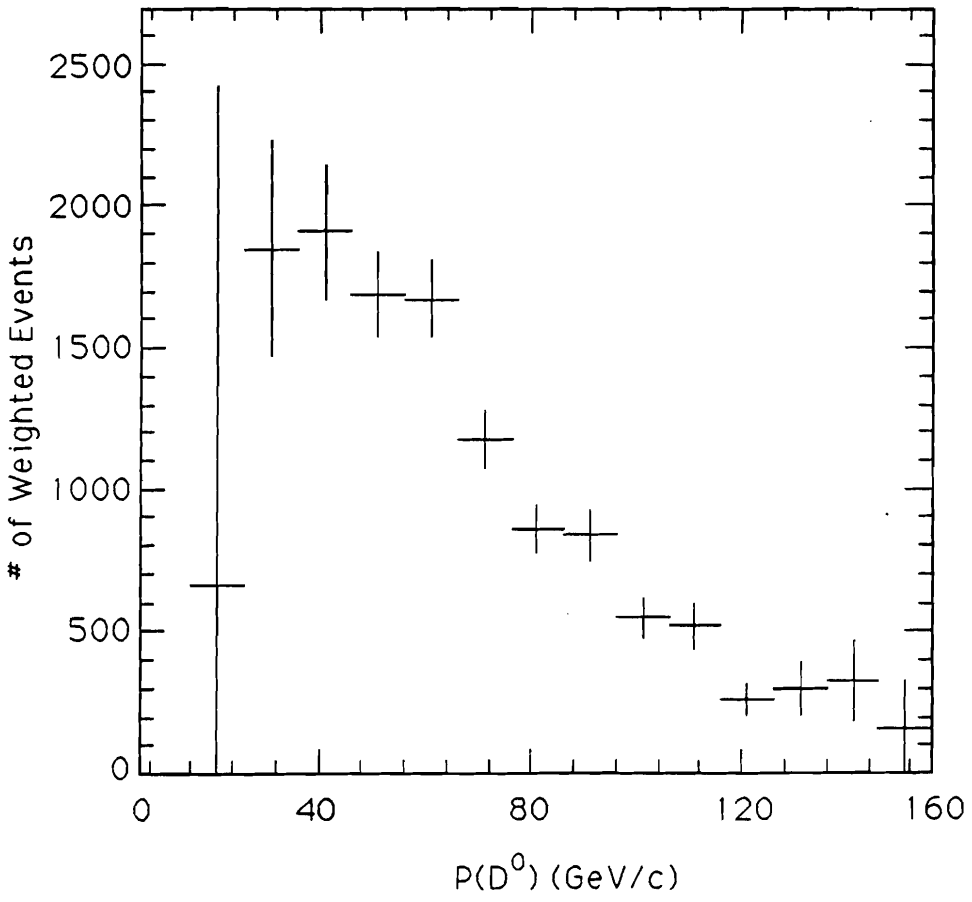

Figure 4.14: True P distribution for D^0 particles from $D^0 \rightarrow K^-\pi^+$ data.

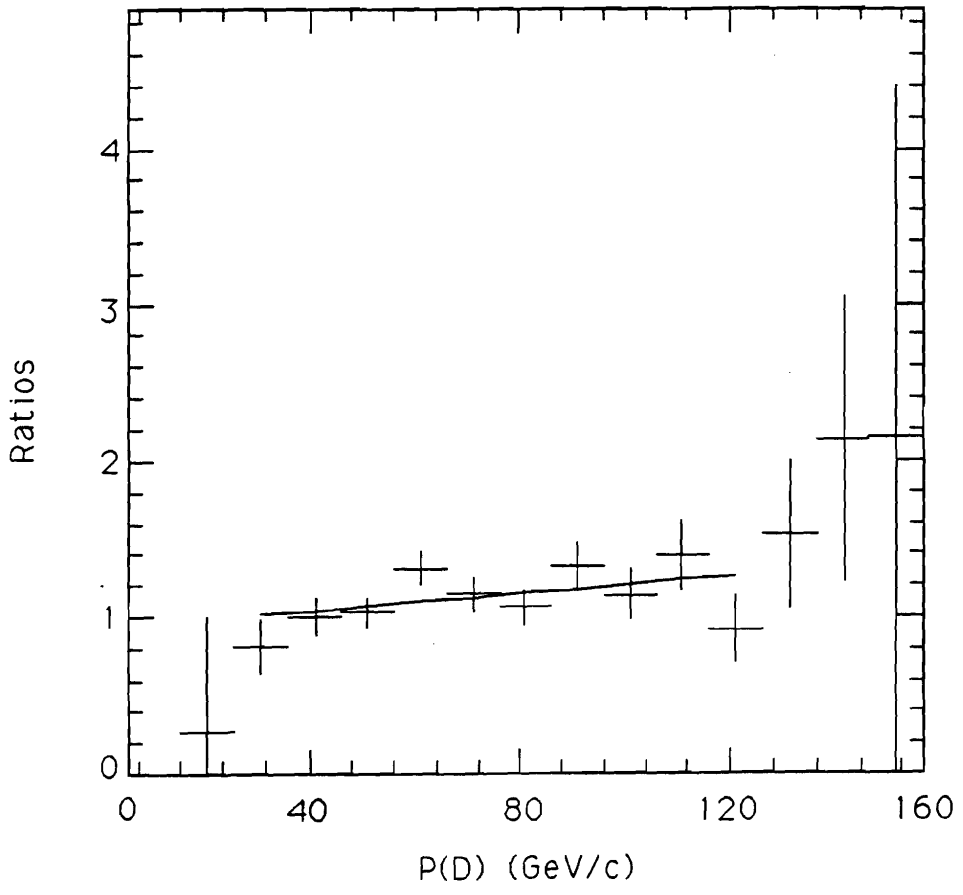

Figure 4.15: Ratios between $D^0 \to K^-\pi^+$ + C.C. and MC populations.

The $cos(\theta)$ cut

Given that the D^0 is a spin 0 meson, the trajectories of decay particles are uniformly distributed throughout a 4π solid angle in its rest frame. Hence, the $cos(\theta)$ distribution of the angle between a daughter particle's momentum vector and the boost direction of the D^0 is flat in this frame. In order to reduce wrong-sign and combinatoric background events from the $D^0 \rightarrow K^-\pi^+$ + C.C. mass plots produced to obtain the true D^0 momentum spectrum, $cos(\theta)$ was calculated for the angle between the boost direction (from rest to lab frame) and the kaon's momentum vector in the D^0 rest frame. This is illustrated in Figure 4.16. The distribution is shown in Figure 4.17, with only invariant mass cuts applied, and is not background subtracted. A corresponding distribution for Monte Carlo data is shown in Figure 4.18. As is evidenced by comparing the shape of these two plots, most of the background is located at the -1.0 extreme of the $cos(\theta)$ range. A cut at $|cos(\theta)| \leq 0.8$ eliminates $\simeq$ 70 % of the background and is approximately 70 % efficient.

Final efficiency results

Once the true p spectrum was obtained, determining the N_{ij} from the Monte Carlo data for both $D^0 \rightarrow K^-K^+$ and $D^0 \rightarrow \pi^-\pi^+$ modes became straightforward. Histograms of the reconstructed D^0 mass (M_D) were made for the 36 momentum "cells" defined by the 6 ranges for pion and kaon three-momenta described above. The reconstructed three-momentum of the D^0 (P_D) was also calculated. At filling time, M_D was weighted by the ratio appropriate to the value of P_D. In this way, the correct P_D spectrum was restored, while at the same time insuring correct momentum distributions for individual pions and kaons in $D^0 \rightarrow K^-K^+$ and $D^0 \rightarrow \pi^-\pi^+$ decays.

When calculating the overall efficiencies ϵ_C, only cells having a prominent $D^0 \rightarrow K^-\pi^+$ signal with good statistical significance ($N/\Delta N \geq 4.0$) were included in the weighted sum. These cells are shown in the following table:

	K momentum (GeV/c)					
π momentum (GeV/c)	6 - 10	10 - 20	20 - 37	37 - 70	70 - 100	100 - 200
6 - 10	no	no	yes	yes	no	no
10 - 20	no	yes	yes	yes	yes	no
20 - 37	yes	yes	yes	yes	yes	no
37 - 70	yes	yes	yes	yes	yes	no
70 - 100	no	yes	yes	yes	no	no
100 - 200	no	no	no	no	no	no

Table 4.6: Momentum "cells" used in weighted efficiency calculation.

These mass plots were fit using the least-squares method by a Gaussian of σ = 0.0104 GeV/c^2 and mean 1.865 GeV/c^2 for the signal. The background was a straight line. The final efficiencies are:

$$\epsilon_C(KK) = 0.389 \pm 0.0149$$

$$\epsilon_C(\pi\pi) = 0.526 \pm 0.0208$$

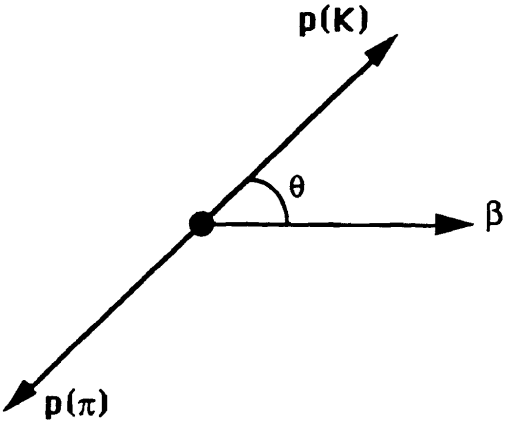

Figure 4.16: Illustration of $cos(\theta)$ in the D^0 rest frame.

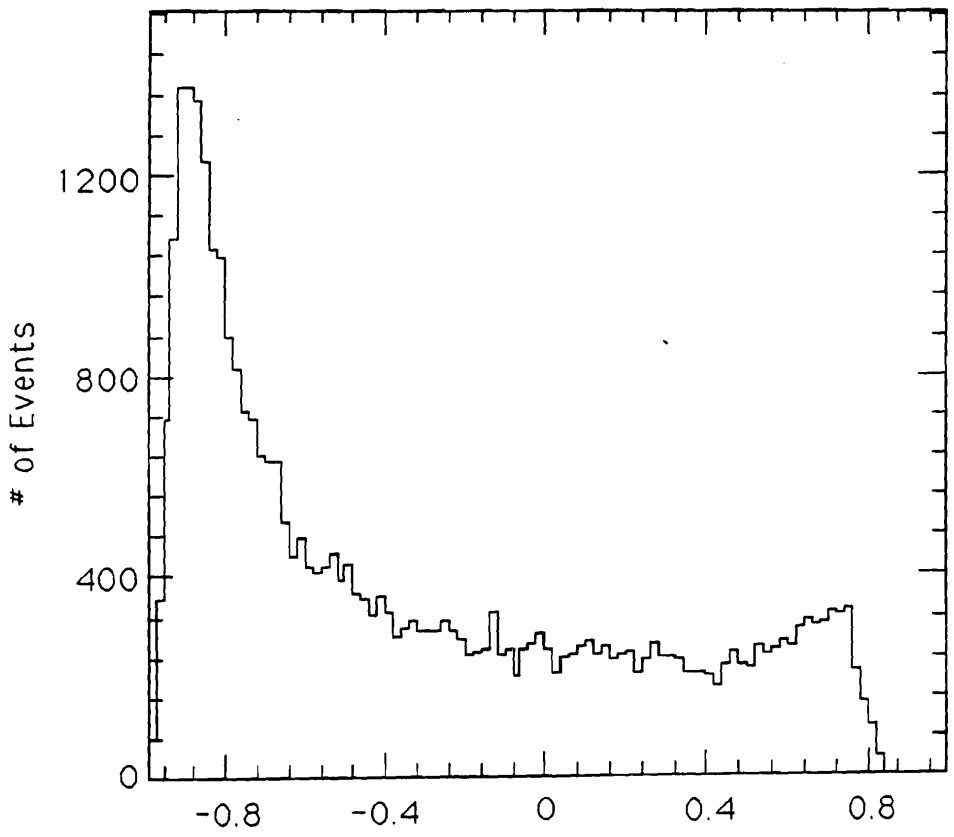

Figure 4.17: $cos(\theta)$ distribution for $D^0 \rightarrow K^-\pi^+$ + C.C. events.

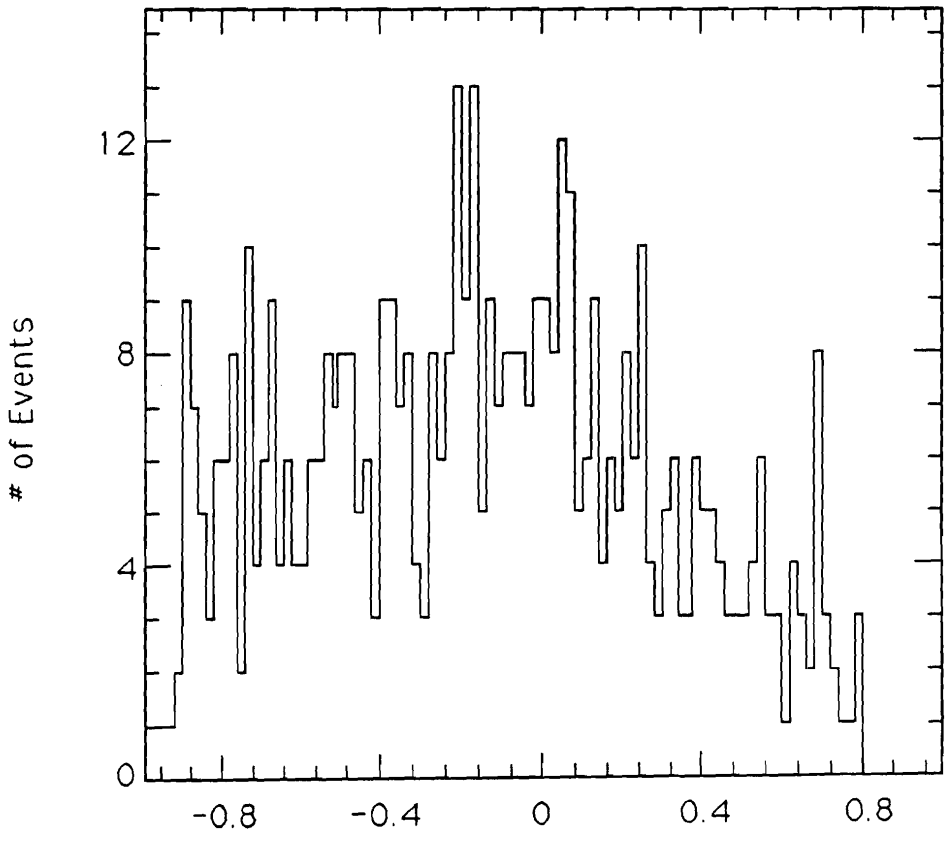

Figure 4.18: $cos(\theta)$ distribution for MC $D^0 \rightarrow K^-\pi^+$ + C.C. events.

4.6 Analysis for Relative Branching Fractions

Accurately measuring the ratio of branching fractions between the Cabibbo-suppressed decays $D^0 \rightarrow K^-K^+$ and $D^0 \rightarrow \pi^-\pi^+$ required obtaining mass plots of these signals with as little combinatoric background and contamination from other modes as possible. In order to further reduce the background, all the cuts described in the section on higher analysis cuts were applied. Furthermore, the SDZ requirement was made more stringent by demanding that SDZ > 9.0. The resulting mass plots for $D^0 \rightarrow \pi^-\pi^+$ and $D^0 \rightarrow K^-K^+$ are shown in Figures 4.19 and 4.20 respectively.

4.6.1 $D^0 \rightarrow \pi^-\pi^+$ Analysis

$D^0 \rightarrow K^-\pi^+$ feedthroughs

In the $\pi\pi$ mass plot, besides the signal, there is a broad peak at 1.77 GeV/c^2, due to $D^0 \rightarrow K^-\pi^+$ decays where the kaon is misidentified as a pion. A parametrization of this "false peak" is found from the Monte Carlo simulation. A mass plot containing MC $D^0 \rightarrow K^-\pi^+$ events analyzed as $\pi\pi$ events is shown in Figure 4.21. Given that the pion has a lower mass than the kaon, the reconstructed invariant mass peaks somewhat lower than the D^0 mass of 1.865 GeV/c^2. The entries above the kinematic limit of 1.82 GeV/c^2 are just random combinations of tracks from the track list, and are not true $D^0 \rightarrow K^-\pi^+$ decays. Due to the asymmetrical shape of this peak, this distribution was fit by a function of the form:

$$F(m) = N_{fp}[(\frac{\Gamma}{\pi(\Gamma^2 + (m - m_0)^2)}\theta(m - m_0)) + (\frac{1}{\sqrt{2\pi}\sigma_{fp}}e^{-\frac{(m-m_0)^2}{2\sigma_{fp}^2}}\theta(m_0 - m))]$$

where the mass range below the peak is a Breit-Wigner of width $\Gamma = 0.0190$ GeV/c^2 and the range above is a Gaussian of width $\sigma_{fp} = 0.0178$ GeV/c^2. In the above equation, θ is the Heavyside step function. Fitting the $D^0 \rightarrow \pi^-\pi^+$ mass plot with the above form for N_{fp} and other terms discussed below yielded $N_{fp} = 381 \pm 42$

events if a polynomial background form (*i.e.* $Am^2 + Bm + C$) was assumed, and $N_{fp} = 401 \pm 50$ events if an exponentiated polynomial (*i.e.* $\exp(Am^2 + Bm + C)$) was used. As a rough check, Monte Carlo data was used to compute the number of $D^0 \rightarrow K^-\pi^+$ events that should fall into the false peak of the $D^0 \rightarrow \pi^-\pi^+$ mass plot. This is given by:

$$N_{K\pi \rightarrow \pi\pi} = N_{K\pi} \times \frac{\epsilon(K\pi \rightarrow \pi\pi)}{\epsilon(K\pi \rightarrow K\pi)}$$

where $N_{K\pi}$ is the number of data events in the $D^0 \rightarrow K^-\pi^+$ mass plot and $\epsilon(K\pi \rightarrow \pi\pi)$ is the efficiency for finding a $D^0 \rightarrow K^-\pi^+$ MC event in the $D^0 \rightarrow \pi^-\pi^+$ mass plot. This last number was found to be

$$\epsilon(K\pi \rightarrow \pi\pi) = 1.505 \times 10^{-2} \pm 0.10 \times 10^{-2}$$

The result is $N_{K\pi \rightarrow \pi\pi} = 616 \pm 45$ events. The discrepancy between the experimental number and the predicted one is most likely due to the fact that the Monte Carlo Čerenkov efficiencies do not accurately reflect the data. Another cause of the discrepancy is the existence in the data of a large combinatoric background both at the same mass (the false peak "sits" on combinatoric background) and at lower masses than the false peak, which may force the fit to undercount the number of events in the false peak itself.

Combinatoric Background

A term of the form $Am^2 + Bm + C$ is used for the combinatoric background, other than the false peak. This consists of random pairs of tracks, chosen by the analysis algorithm from the track list, which pass the cuts described in section 4.3.2. A variety of other functional forms were tested in order to determine the effect of the background form on signal strength. A more detailed discussion of the systematic error involved follows below.

Signal Strength

The signal term in the fit is a Gaussian with mean fixed at the established value of 1.865 GeV/c^2 and σ fixed at $\sigma = 0.0121$ GeV/c^2. The later was determined by performing a fit to a mass plot consisting of 18,000 Monte Carlo events. The MC signal peak is shown in Figure 4.22. A Gaussian of floating width but fixed mean (at the D^0 mass) was fit to this distribution in order to obtain the signal width for real data. A fit to data yielded 120 $\pm$ 18 events.

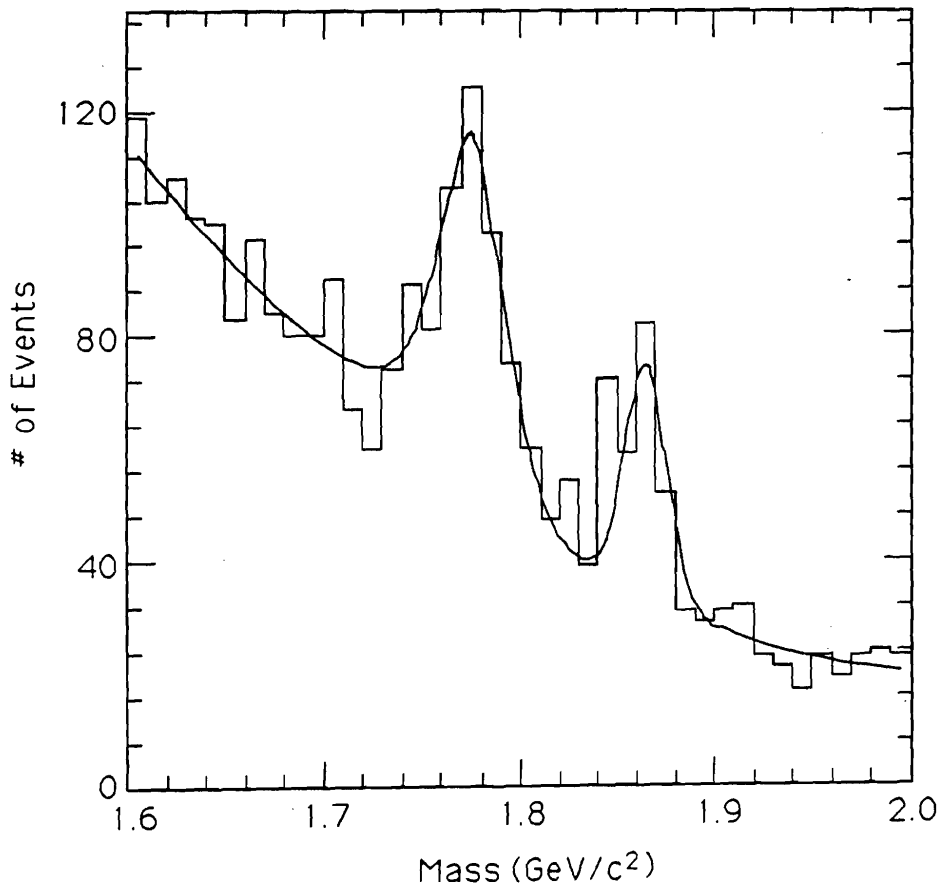

Figure 4.19: $D^0 \rightarrow \pi^-\pi^+$ + C.C. mass distribution.

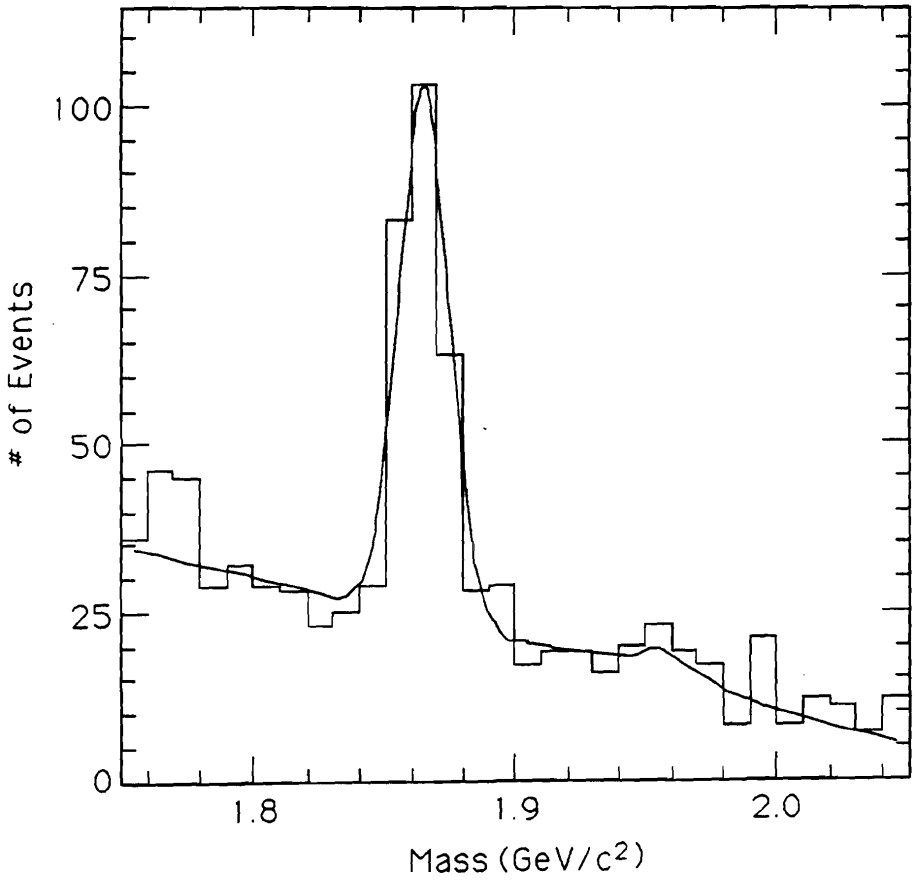

Figure 4.20: $D^0 \rightarrow K^- K^+$ + C.C. mass distribution.

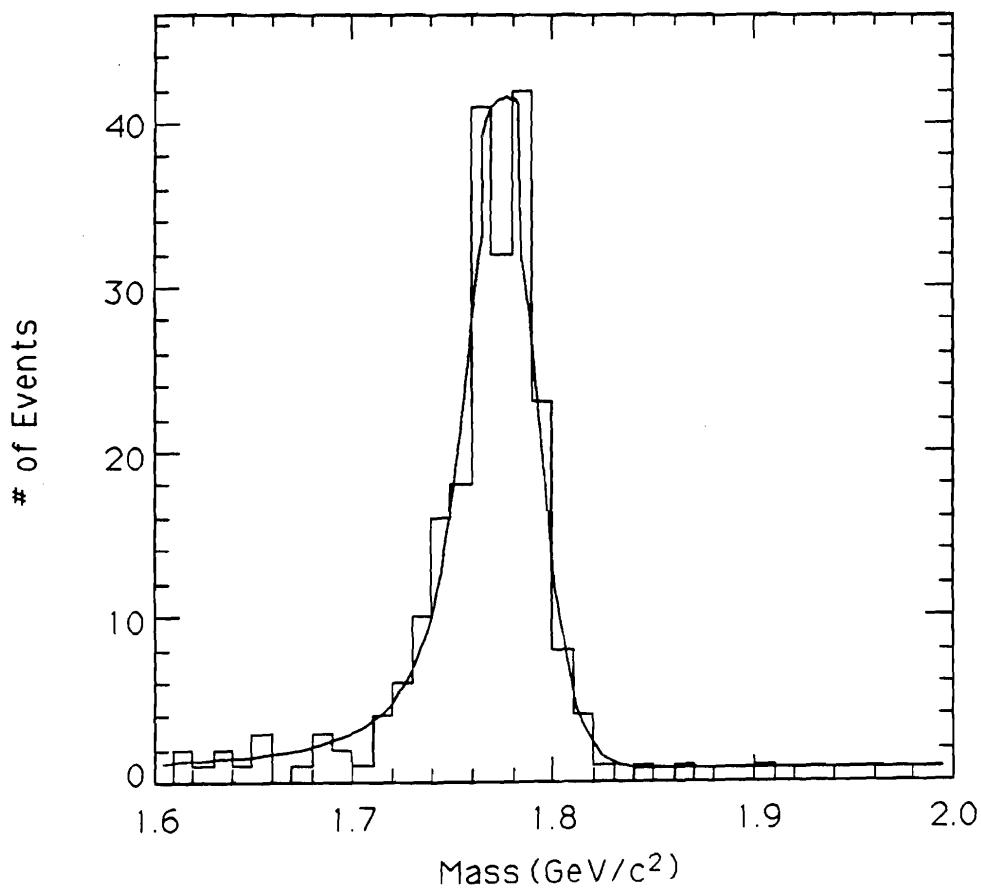

Figure 4.21: $D^0 \to K^-\pi^+$ + C.C. analyzed as $D^0 \to \pi^-\pi^+$ decays from 18,000 MC events.

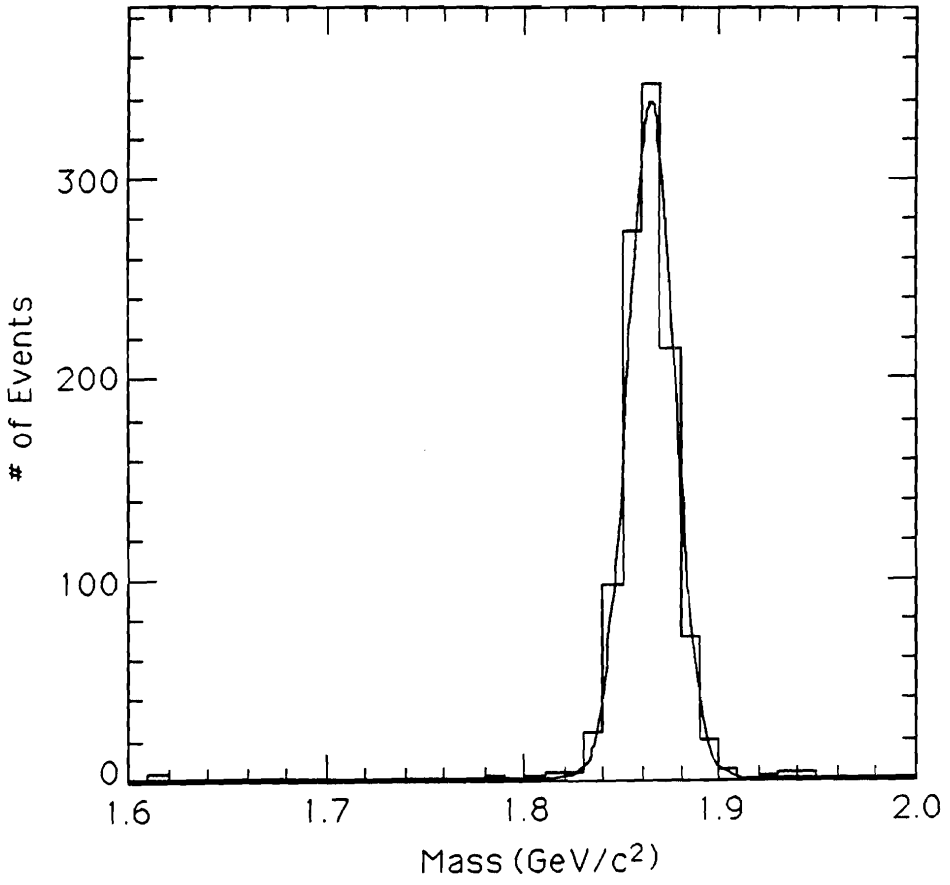

Figure 4.22: $D^0 \rightarrow \pi^-\pi^+$ + C.C. mass distribution from 18,000 MC events.

Backgrounds involving π^0s

The background due to the decays $D^0 \to K^-\pi^+\pi^0$ and $D^0 \to K^-\pi^+\pi^0\pi^0$ were studied using the MC simulation. The feedthroughs are shown in Figures 4.23 and 4.24 for the $D^0 \to K^-\pi^+\pi^0$ and $D^0 \to K^-\pi^+\pi^0\pi^0$ modes, respectively. The number of π^0 feedthroughs was calculated in the following manner:

$$N_{D^0\to K^-\pi^+\pi^0} = N_{D^0\to K^-\pi^+} \times \frac{\epsilon_{D^0\to K^-\pi^+\pi^0}}{\epsilon_{D^0\to K^-\pi^+}} \times \frac{BR(D^0 \to K^-\pi^+\pi^0)}{BR(D^0 \to K^-\pi^+)}$$

and similarly for $D^0 \to K^-\pi^+\pi^0\pi^0$ decays. In the above expression, $N_{D^0\to K^-\pi^+}$ is the number of $D^0 \to K^-\pi^+ + \text{C.C.}$ feedthroughs in the $D^0 \to \pi^-\pi^+$ mass plot, and the ϵ are the overall efficiencies for these modes appearing in the $D^0 \to \pi^-\pi^+$ mass plot. The ratio of branching fractions was taken from the Particle Data Tables. The results are:

$$\epsilon_{D^0\to K^-\pi^+\pi^0} = 3.3 \times 10^{-4} \pm 0.1 \times 10^{-4}$$

$$\epsilon_{D^0\to K^-\pi^+\pi^0\pi^0} = 6.1 \times 10^{-4} \pm 0.2 \times 10^{-4}$$

$$N_{D^0\to K^-\pi^+} = 343 \pm 36$$

$$N_{D^0\to K^-\pi^+\pi^0} = 30 \pm 6$$

$$N_{D^0\to K^-\pi^+\pi^0\pi^0} = 58 \pm 21$$

In both cases, the contribution is about 1% of the contents of the $D^0 \to \pi^-\pi^+$ mass plot, and therefore no explicit term for these modes was included.

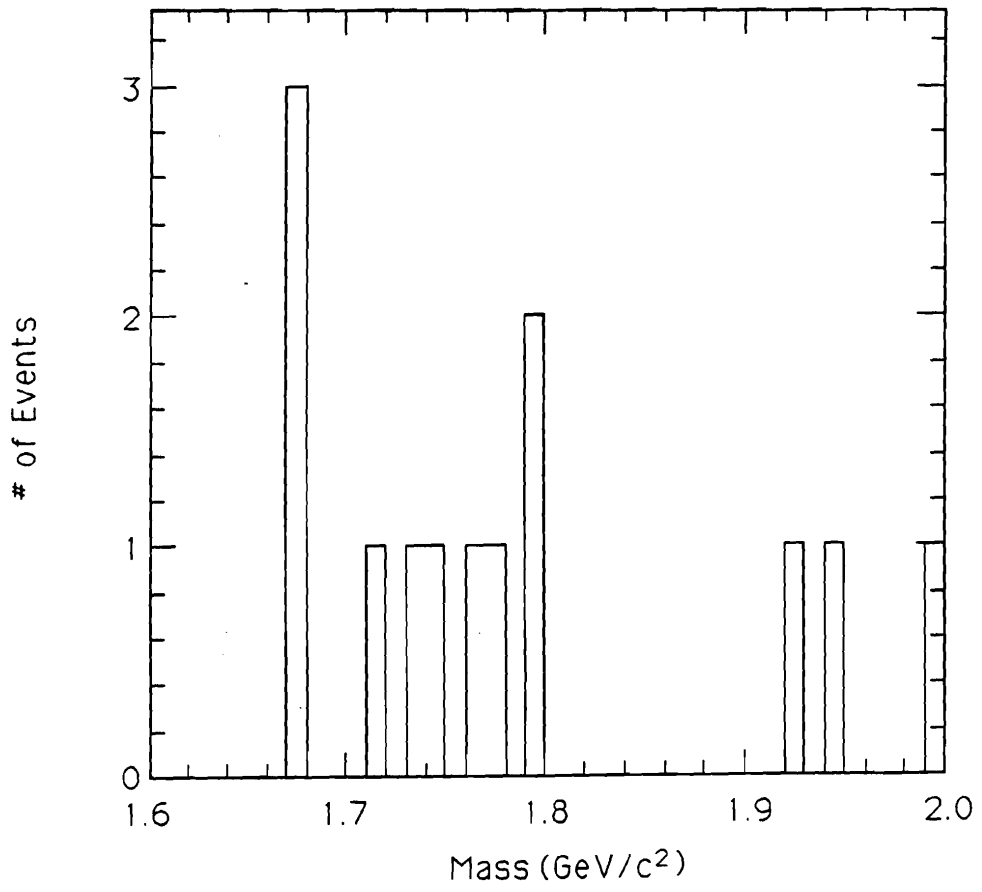

Figure 4.23: $D^0 \to K^-\pi^+\pi^0$ + C.C. analyzed as $D^0 \to \pi^-\pi^+$ decays from 18,000 MC events.

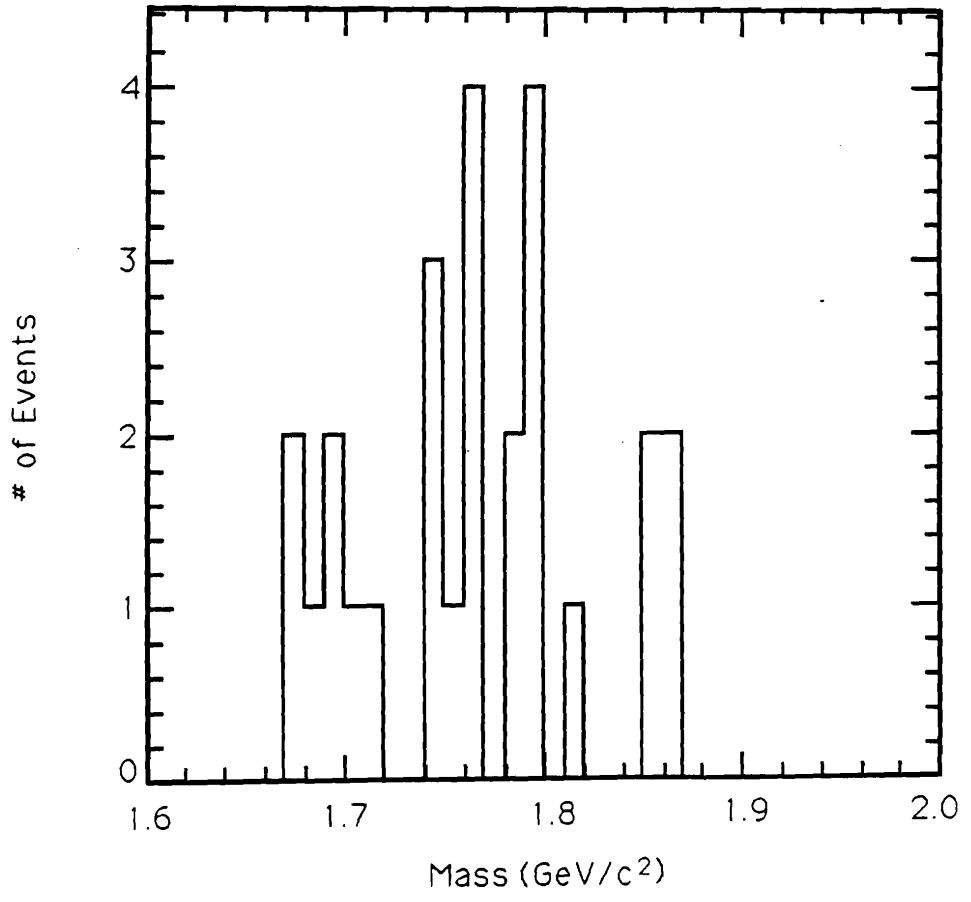

Figure 4.24: $D^0 \rightarrow K^-\pi^+\pi^0\pi^0$ + C.C. analyzed as $D^0 \rightarrow \pi^-\pi^+$ decays from 18,000 MC events.

4.6.2 $D^0 \rightarrow K^-K^+$ Analysis

As can be seen from Figures 4.19 and 4.20, the structure of the $D^0 \rightarrow K^-K^+$ mass distribution is simpler than that of the $D^0 \rightarrow \pi^-\pi^+$ mass plot. There is no prominent $D^0 \rightarrow K^-\pi^+$ feedthrough peak, and the combinatoric background is, in general, much lower.

$D^0 \rightarrow K^-\pi^+$ feedthroughs

Monte Carlo studies similar to those performed for $D^0 \rightarrow \pi^-\pi^+$ decays demonstrated the existence of a "false peak" at 1.95 GeV/c^2 due to misidentified $D^0 \rightarrow K^-\pi^+$ decays. That this peak is located at a higher mass than that of the D^0 is due to the misidentification of a pion as a kaon, thereby producing a higher effective mass than 1.865 GeV/c^2. The Monte Carlo false peak, produced from 18,000 $D^0 \rightarrow K^-\pi^+$ events, is shown in Figure 4.25. Note that in order to obtain sufficient statistics for this plot, no Čerenkov cut was applied. As in the $D^0 \rightarrow \pi^-\pi^+$ case, the asymmetry of this peak required the use of a functional form involving θ-functions in the fit:

$$F(m) = N_{fp}[(\frac{1}{\sqrt{2\pi}\sigma_{fp}} e^{-\frac{(m-m_0)^2}{2\sigma_{fp}^2}} \theta(m-m_0)) + ((\frac{\Gamma}{\pi(\Gamma^2+(m-m_0)^2)} + C)\theta(m_0-m))]$$

In this case, however, the "order" of Gaussian and Breit-Wigner is reversed, in that the Gaussian covers the mass region below the peak, while the Breit-Wigner covers that above. A fit to MC data yielded σ_{fp} = 0.0164 GeV/c^2 and Γ =0.0214 GeV/c^2.

Signal Strength

The number of signal events was determined by a least-squares fit of the type described above for $D^0 \rightarrow \pi^-\pi^+$ decays, but with σ = 0.0091 GeV/c^2 for the

Gaussian signal. The signal width for $D^0 \to K^-K^+$ is slightly smaller than that for $D^0 \to \pi^-\pi^+$, where $\sigma = 0.0121$ GeV/c^2, because of the difference in Q-values of these decays. The fit for $D^0 \to K^-K^+$ gives 193 ± 18 signal events. A straight line was fit to the combinatoric background.

4.6.3 $D^0 \to K^-\pi^+$ analysis

The analysis for the decay $D^0 \to K^-\pi^+$ is straightforward because the only significant background is combinatoric. The $D^0 \to K^-\pi^+$ mass distribution is shown in Figure 4.26. All the cuts described in section 4.3.2 were applied, except a cut on Čerenkov identification probability (the reasons for this were given beforehand). This mass plot was fit using techniques similar to those described above. The signal was fit using a Gaussian of width $\sigma = 0.0104$ GeV/c^2. The difference between this width and that of the other decays is due to the difference in their Q-values. The combinatoric background was fit using a straight line. The signal strength is estimated to be 4322 ± 97 signal events.

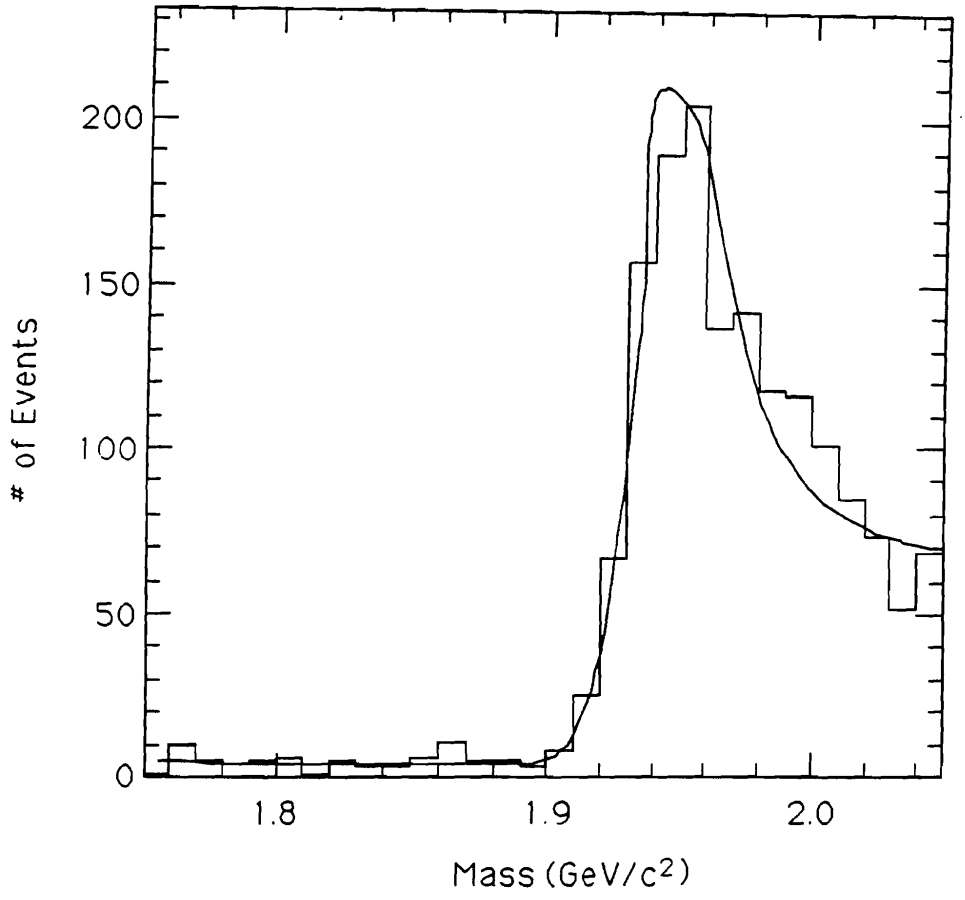

Figure 4.25: $D^0 \rightarrow K^-\pi^+$ + C.C. decays analyzed as $D^0 \rightarrow K^-K^+$ decays, from 18,000 MC events. There is no Čerenkov cut applied.

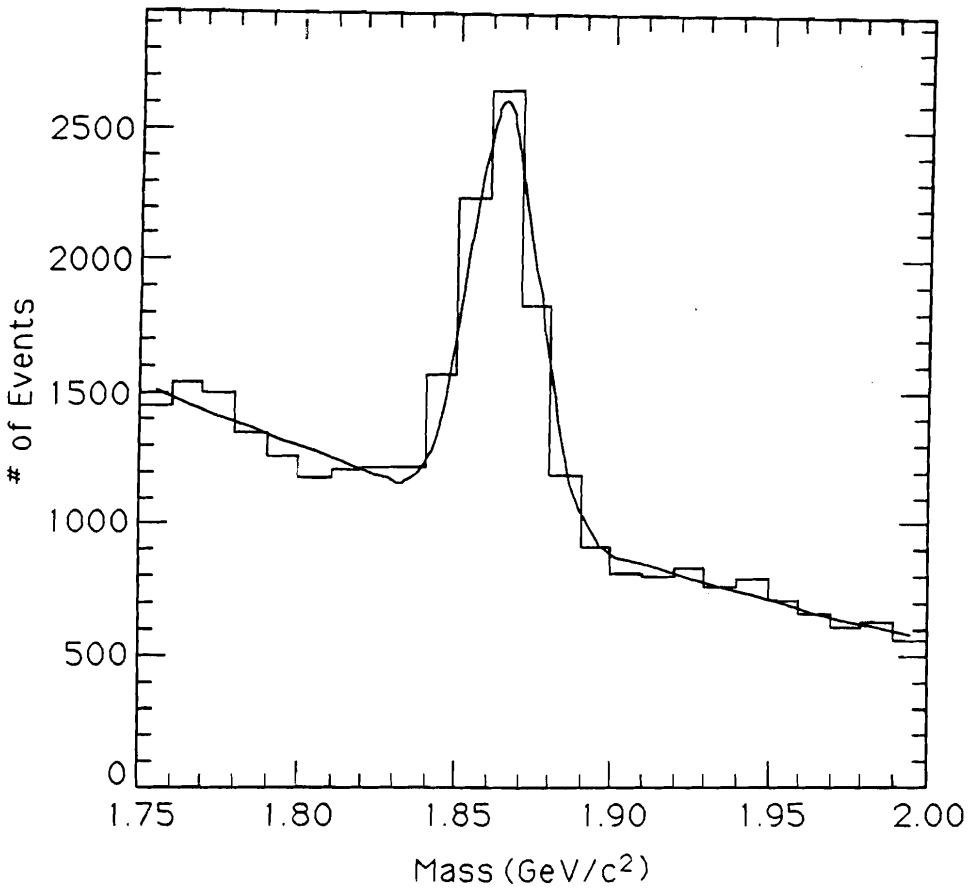

Figure 4.26: $D^0 \rightarrow K^-\pi^+$ + C.C. mass distribution.

4.7 Results on Branching Ratio Fractions

4.7.1 Study of Systematic Effects

Systematic error due to the uncertainty in $D^0 \rightarrow \pi^-\pi^+$ mass resolution

The sensitivity of $N_{\pi\pi}$ to slight changes in the fixed width used to fit the signal peak (i.e. σ_D) was studied. From the Monte Carlo, $\Gamma_{\pi\pi}$ was determined to be 12.1 $\pm$ 0.43 MeV/c^2. When $\Gamma_{\pi\pi}$ was increased by one σ (i.e.by 0.43 MeV/c^2), the result for $N_{\pi\pi}$ was 167 $\pm$ 25 events. When $\Gamma_{\pi\pi}$ was decreased by one σ, the fit yielded a signal of 162 $\pm$ 23 events. The variation is less than 20 % of the error attached to $N_{\pi\pi}$ in either case, leading to the conclusion that the signal is stable under small changes in signal width. Given this, no systematic error was included for this effect.

Uncertainty due to background parametrization for $D^0 \rightarrow \pi^-\pi^+$

In order to determine the best fit to this combinatoric background , various functional forms were used to fit the background of the $D^0 \rightarrow \pi^-\pi^+$ mass plot: a second-order polynomial, an exponential multiplied by a polynomial, and an exponentiated polynomial of the form $\exp(Am^2 + Bm + C)$. In addition, the last three bins of the mass plot were chopped off, and the background was once again fit by an exponentiated polynomial, and by a second order polynomial. This produced five principle values, which are shown in the following table.

Mass Range	Background Parametrization	$N_{\pi\pi}$
1.60 - 2.00 GeV/c^2	$Am^2 + Bm + C$	168 $\pm$ 23
1.60 - 2.00 GeV/c^2	$e^{-Am} \times (Bm + C)$	171 $\pm$ 27
1.60 - 2.00 GeV/c^2	$\exp(Am^2 + Bm + C)$	165 $\pm$ 23
1.63 - 2.00 GeV/c^2	$Am^2 + Bm + C$	172 $\pm$ 24
1.63 - 2.00 GeV/c^2	$\exp(Am^2 + Bm + C)$	157 $\pm$ 23

Table 4.7: Effect of different background parametrizations on $D^0 \rightarrow \pi^-\pi^+$ signal strength.

all within at most 1 σ of each other. The systematic error due to this effect can be estimated by the dispersion of these values about their mean. The r.m.s. dispersion is $\pm$ 6.

Systematic errors due to efficiencies

The systematic error due to the Čerenkov efficiencies was derived through straightforward error propagation through the ratio of efficiencies

$$R_\epsilon = \frac{\epsilon_C(\pi^+\pi^-)}{\epsilon_C(K^+K^-)}.$$

As a reminder, the overall Čerenkov efficiency (for, say, $D^0 \rightarrow K^-K^+$) is given by

$$\epsilon_C(K^-K^+) = \frac{\sum_{ij} N^{ij}_{KK} \epsilon^i_K \epsilon^j_K}{\sum_{ij} N^{ij}_{KK}}$$

where N^{ij}_{KK} is the number of $D^0 \rightarrow K^-K^+$ Monte Carlo events contained in momentum cell (ij). Similarly, the Čerenkov efficiency for $D^0 \rightarrow \pi^-\pi^+$ is given by

$$\epsilon_C(\pi^-\pi^+) = \frac{\sum_{ij} N^{ij}_{\pi\pi} \epsilon^i_\pi \epsilon^j_\pi}{\sum_{ij} N^{ij}_{\pi\pi}}.$$

Thus:

$$R_\epsilon = \frac{\sum_{ij} N^{ij}_{\pi\pi} \epsilon^i_\pi \epsilon^j_\pi}{\sum_{ij} N^{ij}_{KK} \epsilon^i_K \epsilon^j_K}$$

Note that the numerator and denominator are not correlated. For other relative branching ratios, the situation is analogous. Explicitly, when calculating $B(D^0 \to K^-K^+)$ / $B(D^0 \to K^-\pi^+)$, one would have a term of the sort:

$$R_\epsilon = \frac{\epsilon_C(K^-\pi^+)}{\epsilon_C(K^-K^+)}.$$

However, since no Čerenkov cut was applied to the $D^0 \to K^-\pi^+$ sample, one simply has $\epsilon_C(K^-\pi^+) = 1$ and, in this case,

$$R_\epsilon = \frac{\sum_{ij} N^{ij}_{KK}}{\sum_{ij} N^{ij}_{KK} \epsilon^i_K \epsilon^j_K}.$$

Once again, the numerator and denominator are not correlated. Obviously, the previous argument holds for $B(D^0 \to \pi^-\pi^+)$ / $B(D^0 \to K^-\pi^+)$ as well.

Note that one expects a larger error for $B(D^0 \to K^-K^+)$ / $B(D^0 \to \pi^-\pi^+)$ than for relative branching ratios involving $D^0 \to K^-\pi^+$, because in the former case, the numerator of R_ϵ contributes to the error, whereas in the latter case the numerator is a constant.

4.7.2 Ratios of Branching Fractions

Combining the results for efficiency and the number of signal events, the relative branching fractions are obtained in the following manner:

$$\frac{B(D^0 \to \pi^-\pi^+)}{B(D^0 \to K^-\pi^+)} = \frac{N(D^0 \to \pi^-\pi^+)}{\epsilon(\pi\pi)} \times \frac{\epsilon(K\pi)}{N(D^0 \to K^-\pi^+)}$$

$$\frac{B(D^0 \to K^-K^+)}{B(D^0 \to K^-\pi^+)} = \frac{N(D^0 \to K^-K^+)}{\epsilon(KK)} \times \frac{\epsilon(K\pi)}{N(D^0 \to K^-\pi^+)}$$

$$\frac{B(D^0 \to K^-K^+)}{B(D^0 \to \pi^-\pi^+)} = \frac{N(D^0 \to K^-K^+)}{\epsilon(KK)} \times \frac{\epsilon(\pi\pi)}{N(D^0 \to \pi^-\pi^+)}$$

Given the values for Čerenkov and geometrical efficiencies obtained above, the branching fractions from E691 data are shown below:

$$R(K^-K^+/K^-\pi^+) = 0.107 \pm 0.010 \pm 0.009$$

$$R(\pi^-\pi^+/K^-\pi^+) = 0.055 \pm 0.008 \pm 0.005$$

$$R(K^-K^+/\pi^-\pi^+) = 1.95 \pm 0.34 \pm 0.22$$

where the first error quoted is statistical. The second error quoted is the combined systematic error due to ϵ_C, ϵ_G and from the different parametrizations of the background.

4.8 Analysis for CP violation study

The possibility of CP violation in the D^0 - $\overline{D^0}$ system was investigated. As explained previously, such would lead to a difference in the decay rates of particle and antiparticle and is characterized by the asymmetry

$$A = \frac{\Gamma - \overline{\Gamma}}{\Gamma + \overline{\Gamma}} = \frac{N - \overline{N}}{N + \overline{N}}$$

where N and $\overline{N}$ are the number of particles and antiparticles, respectively, for the case where particle and antiparticle are produced in equal numbers. For the decays $D^0 \to K^-K^+$ and $D^0 \to \pi^-\pi^+$, Bigi [10] has estimated that CP asymmetries are at most a few $\times 10^{-3}$ within the standard model. Since the signal for $D^0 \to K^-K^+$ is both cleaner and provides better statistics, this channel was chosen for analysis. In this case, the decay rates are given by:

$$Rate(D^0 \to K^-K^+) = |T_{KK}|^2 e^{-\Gamma_D t}(1 - a_{KK}\sin(\Delta m\, t))$$

$$Rate(\overline{D^0} \to K^- K^+) = |\overline{T}_{KK}|^2 \, e^{-\Gamma_D t}(1 + a_{KK} \sin(\Delta m \, t))$$

where Δm is the mass difference between the mass eigenstates, a_{KK} is the CP violating decay parameter due to mixing, $|T_{KK}|^2$ and $|\overline{T}_{KK}|^2$ are the decay amplitudes for particle and antiparticle, respectively.

4.8.1 The D^* Cut

In order to obtain clean $D^0 \to K^- K^+$ samples, and to tag the flavor of the heavy quark as charm or anticharm, a D^* cut was applied to the data sample. This cut requires that all neutral D particles stem from the strong decay of charged charmed mesons, following the decay chain:

$$D^{*+} \to D^0 \pi^+, \;\; D^0 \to K^- K^+$$

$$D^{*-} \to \overline{D^0} \pi^-, \;\; \overline{D^0} \to K^- K^+$$

The difference between the invariant masses of the D^* and the D is slightly more than the pion mass of 139.6 MeV/c^2. Hence, the strong decay $D^* \to D\pi$ has a very small Q-value, and the pion is produced with little three-momentum in the D^* rest frame.

Operationally, once a two-body D decay had been identified and the D mass m_D calculated, a third track was added and the invariant mass $m(D, \pi)$ determined. The difference between these quantities was required to be:

$$143 \text{ MeV/c}^2 \;\leq\; m_D - m(D, \pi) \;\leq 151 \text{ MeV/c}^2$$

The $\Delta m = m_D - m(D, \pi)$ distribution is shown in Figure 4.27 for both D^0 and $\overline{D^0}$ candidates. All the cuts described in section 4.3.2 were applied, and the data is not background -subtracted. If such a pion exists, the D under consideration is deemed to come from D^* decay. The charm is tagged by the charge of this "bachelor" pion.

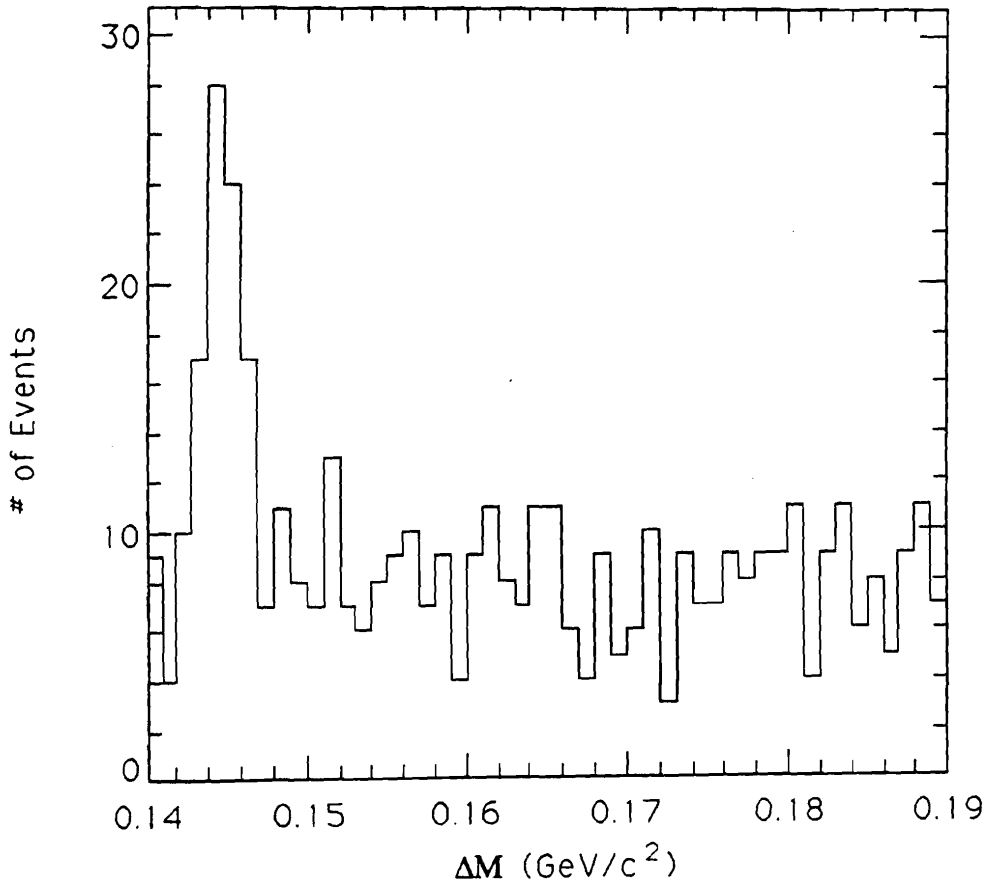

Figure 4.27: $\Delta m = m_D - m(D, \pi)$ distribution.

4.8.2 Mass and Lifetime analysis: a_{KK}

In order to measure the CP violating parameter a_{KK}, $D^0 \rightarrow K^-K^+$ events tagged by the D^* cut detailed above were stripped off the K^-K^+ sample obtained for the branching fraction analysis, except that in this case the SDZ requirement was loosened to SDZ ≥ 5.0. This yielded clean signals for both charm and anticharm. The invariant mass of the selected K^-K^+ decays was histogrammed versus the lifetime of the Ds beyond five standard deviations from the secondary vertex. The $D^0 \rightarrow K^-K^+$ and $\overline{D^0} \rightarrow K^-K^+$ mass distributions are shown in Figures 4.28 and 4.29 respectively, while the corresponding τ distributions for $m_D \pm 3\sigma$ are shown in Figures 4.30 and 4.31.

In an effort to determine if forcing a_{KK} to certain values made a sensible difference in χ^2 or in visual appearance of the fit, 10 curves were plotted on the lifetime distribution, with values of a_{KK} ranging from 0.0 to 2.0, with Δm fixed at the E691 limit of $\Delta m = 1.5 \times 10^{-4}$ eV/c^2 [16]. These are shown in Figure 4.32. As can be seen, almost no difference in either χ^2 or appearance is discernible. Given the size of the D^0 and $\overline{D^0}$ samples, no final value of a_{KK} was determinable, and no statistically significant deviation from exponential decay is observed.

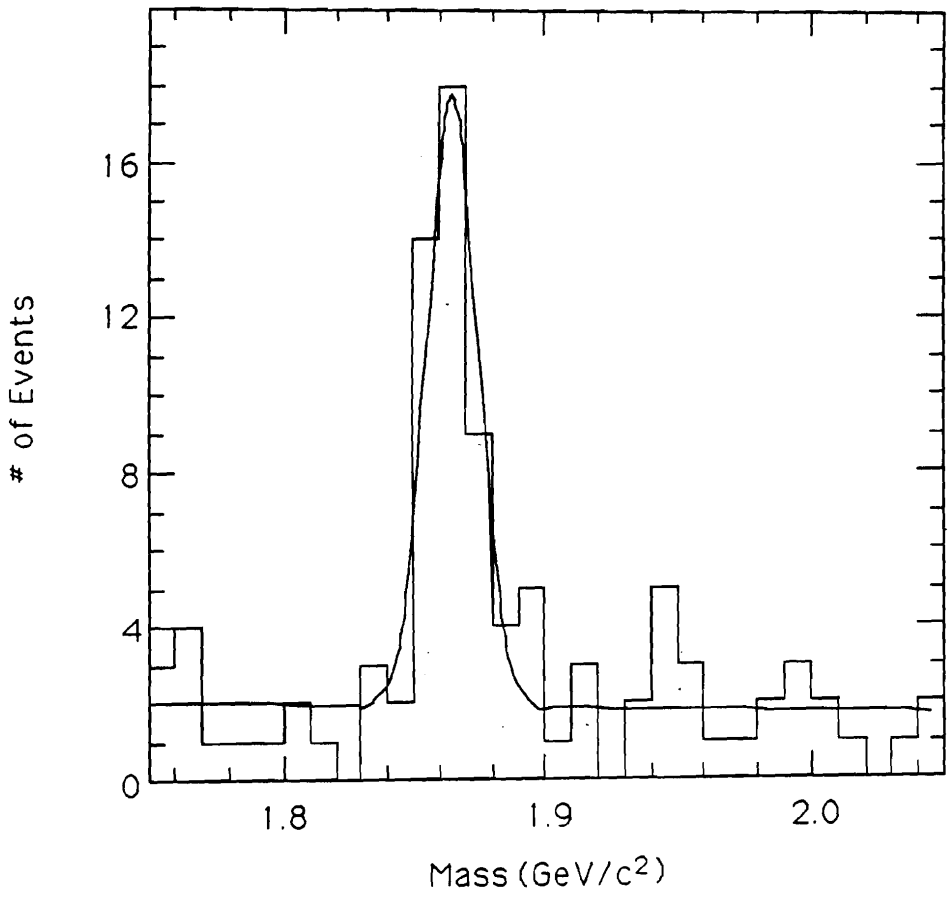

Figure 4.28: $D^0 \rightarrow K^- K^+$ invariant mass distribution at SDZ ≥ 5.0.

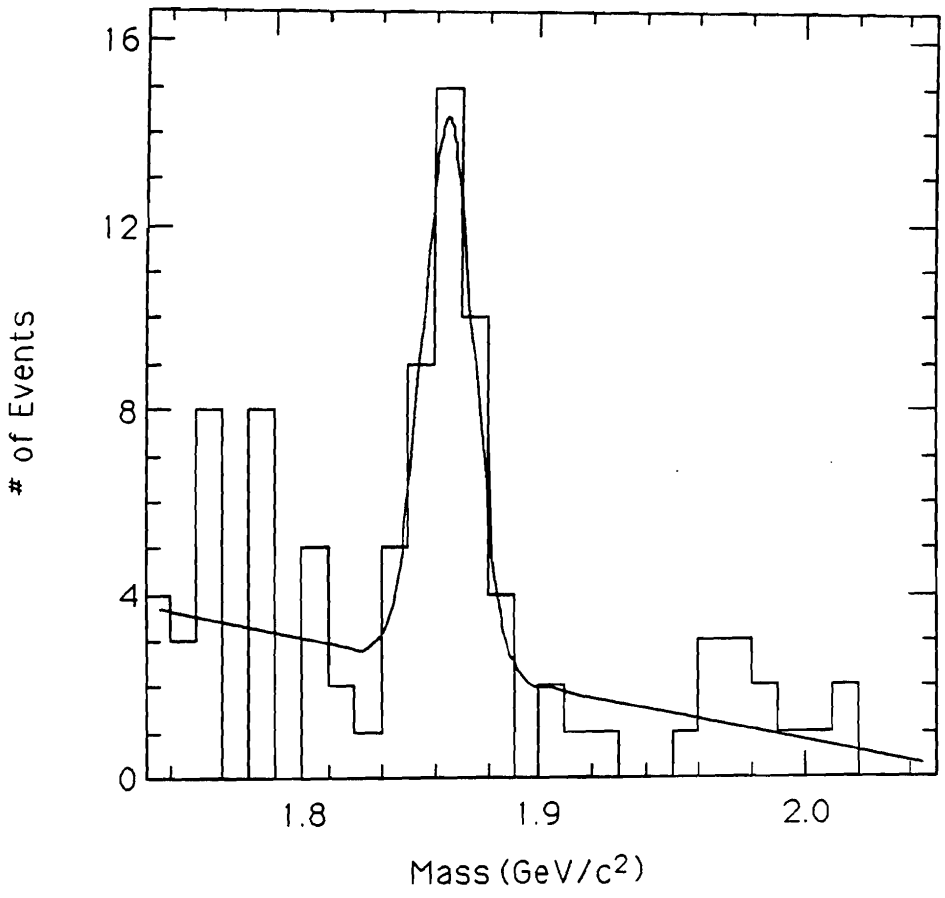

Figure 4.29: $\overline{D^0} \rightarrow K^- K^+$ invariant mass distribution at SDZ ≥ 5.0.

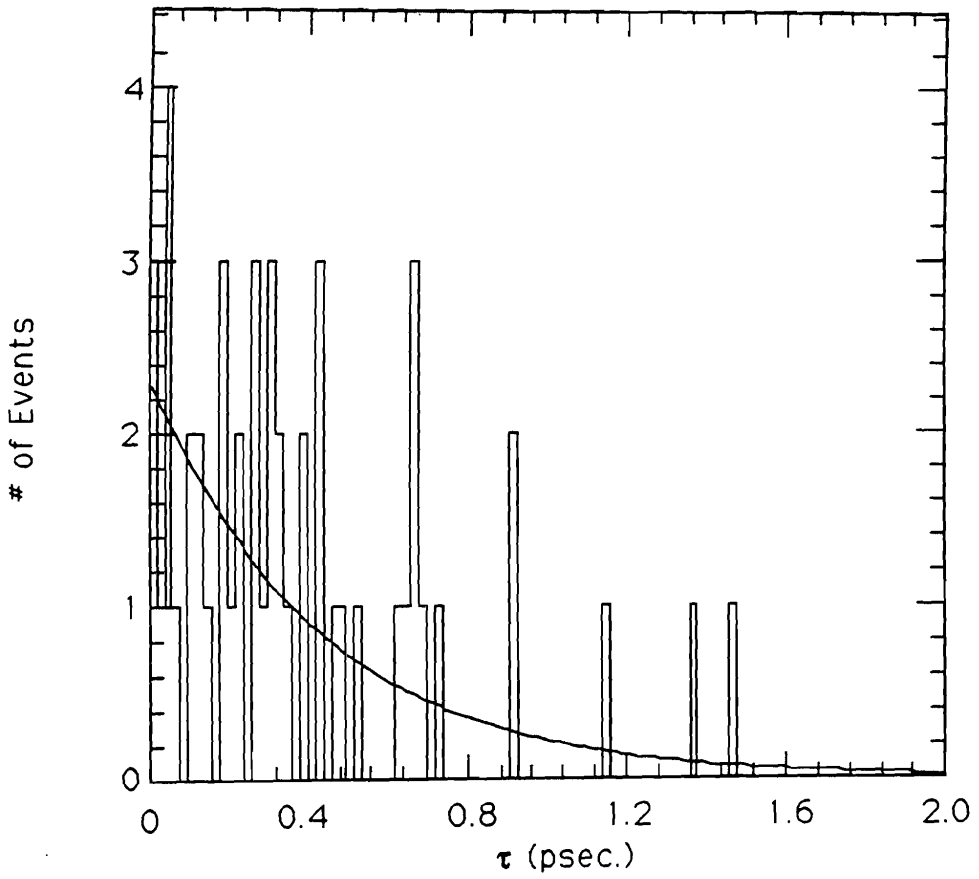

Figure 4.30: $D^0 \rightarrow K^- K^+$ lifetime distribution for $(m_D - 1.865) \leq 28.8\, MeV/c^2$.

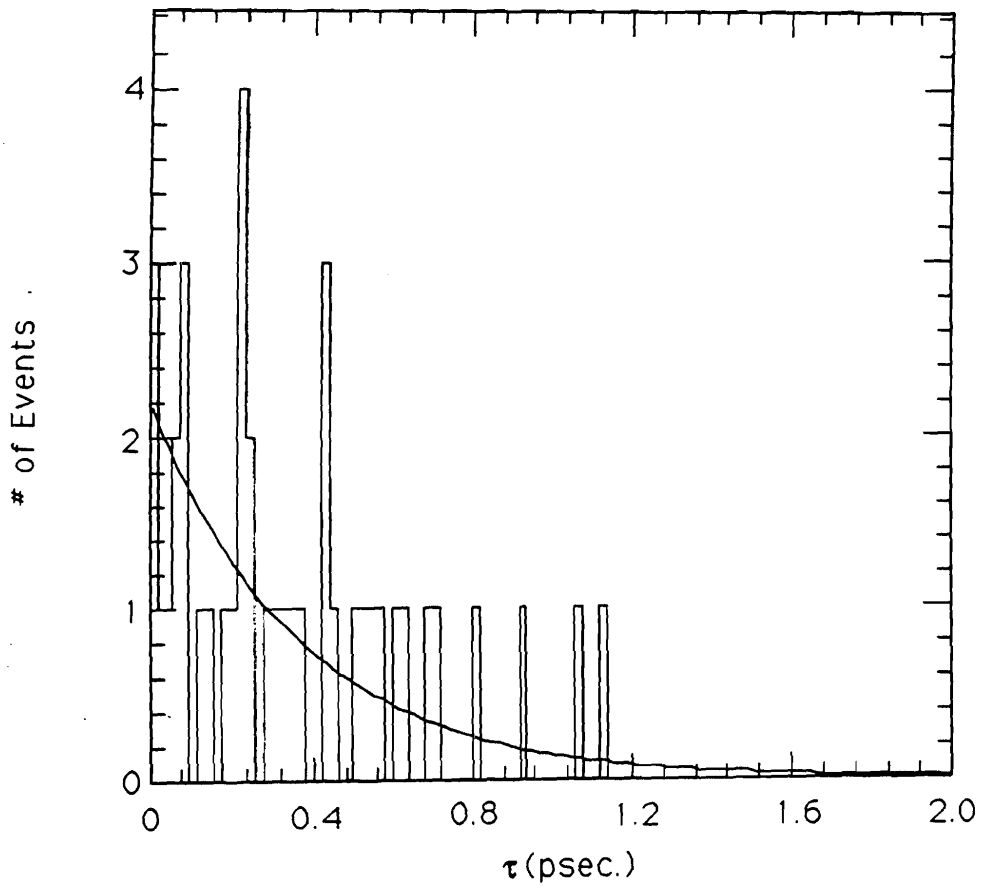

Figure 4.31: $\overline{D^0} \to K^- K^+$ lifetime distribution for $(m_D - 1.865) \leq 28.8\, MeV/c^2$.

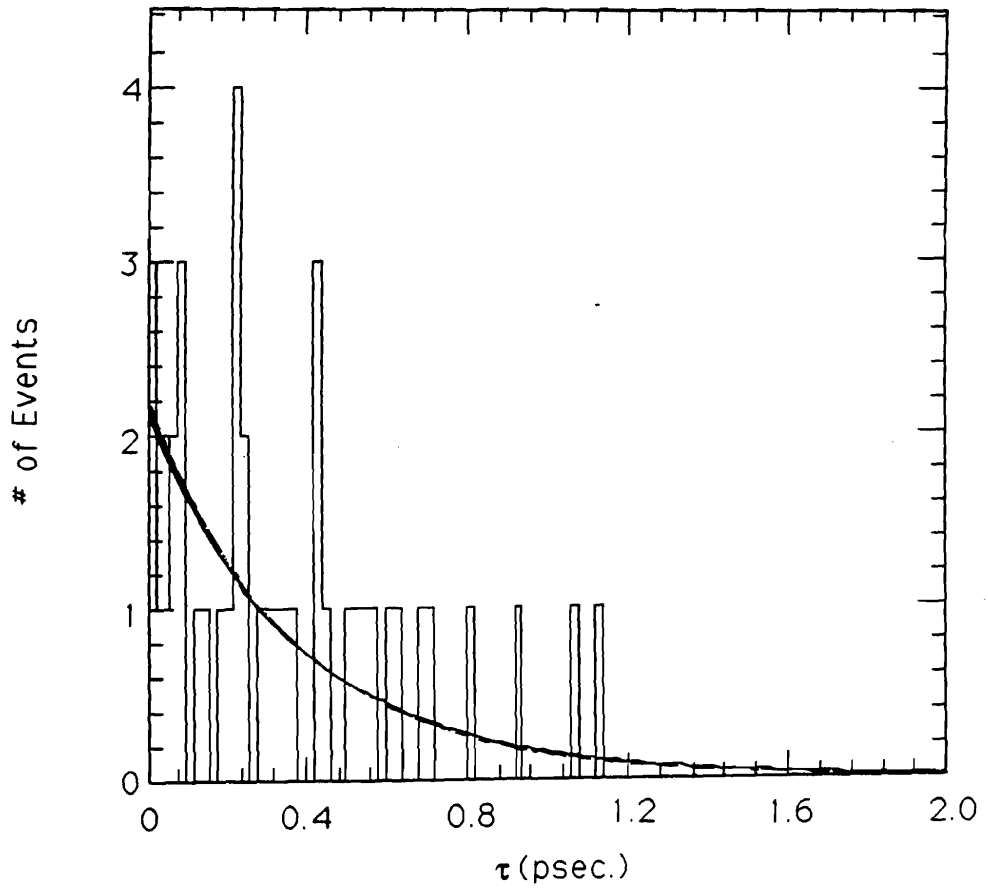

Figure 4.32: $\overline{D^0} \to K^- K^+$ lifetime distribution. There are 10 curves plotted for a_{KK} ranging from 0.0 to 2.0.

4.8.3 Time-Integrated Asymmetry: A'

Even though no CP violation due to mixing was discernible for reasons detailed in the previous section, the time-integrated CP asymmetry A' can nevertheless be determined from the $D^0 \to K^-K^+$ and $\overline{D^0} \to K^-K^+$ signal strengths:

$$A' = \frac{\int \text{Rate}(D^0 \to K^-K^+) - \int \text{Rate}(\overline{D^0} \to K^-K^+)}{\int \text{Rate}(D^0 \to K^-K^+) - \int \text{Rate}(\overline{D^0} \to K^-K^+)}$$

The signal strengths for both $D^0 \to K^-K^+$ and $\overline{D^0} \to K^-K^+$ modes were obtained by performing a maximum-likelihood fit to the mass plots shown in Figures 4.28 and 4.29, respectively. Gaussians of fixed width $\sigma = 0.0091$ GeV/c^2 were used to fit the signal peaks, while the backgrounds in both cases were fit with a straight line. Even though the background fits are different in the two cases, the average background level in the two plots is approximately the same. The fits yield N_{KK} $= 39 \pm 8$ events and $\overline{N_{KK}} = 30 \pm 7$ events. Based on these values, the asymmetry A' was calculated in the following way:

$$A' = \frac{N_{KK} - \overline{N_{KK}}/\epsilon_p}{N_{KK} + \overline{N_{KK}}/\epsilon_p}$$

where ϵ_p is the particle-antiparticle production asymmetry, measured by E691 to be 1.15 ± 0.07 [30]. Such an asymmetry exists because there is a slight overabundance of positive matter in the target (the beam being neutral). Using the signals quoted above, A $= 0.20 \pm 0.15$, or A ≤ 0.45 at the 90% confidence level. This limit is on the time-independent asymmetry for the case of direct CP violation. In the case of CP violation via mixing the limit is on the combination ax where $x = \Delta m/\Gamma$. Since the limit on x from E691 is 0.09, it is not possible to restrict the allowed region for a from this measurement.

Chapter 5 Conclusions

5.1 Comments on Branching Fraction Ratios

The branching fractions calculated here from E691 data, as well as from other experiments [31, 32, 8, 7], are shown in the table below:

	$K^-K^+/K^-\pi^+$	$\pi^-\pi^+/K^-\pi^+$	$K^-K^+/\pi^-\pi^+$
E691	$.107 \pm .010 \pm .009$	$.055 \pm .008 \pm .005$	$1.95 \pm 0.34 \pm 0.22$
CLEO	$.117 \pm .010 \pm .007$	$.050 \pm .007 \pm .005$	$2.35 \pm 0.37 \pm 0.28$
ARGUS	$.10 \pm .02 \pm .01$	$.040 \pm .007 \pm .006$	2.5 ± 0.7
Mark III	$.122 \pm .018$	$.033 \pm .010$	3.7 ± 1.4
Mark II	$.113 \pm .030$	$.033 \pm .015$	3.4 ± 1.8

Table 5.1: Comparison of ratios of branching fractions.

The MARK II result is from 1979, MARK III from 1985, both ARGUS and CLEO from 1990. An important trend is the decrease over time of the principal value as well as the error quotes on the $K^-K^+/\pi^-\pi^+$ measurement, with the E691 value being the smallest yet. On the other hand, both the $K^-K^+/K^-\pi^+$ and $\pi^-\pi^+/K^-\pi^+$ measurements have remained fairly stable over the years. This is due to the increasing precision with which the $D^0 \rightarrow \pi^-\pi^+$ branching ratio is known.

The E691 value for the ratio of Cabibbo-suppressed modes is the first, however, to be in agreement with theoretical predictions to within 1 σ, lending support to the model promulgated by Bauer, Stech and Wirbel [4] discussed in the first chapter. The results detailed here, both on the ratio of branching fractions and the limit on CP violation, have been accepted for publication and can be found in [33].

5.2 Comments on CP Violation

The limit on the time-independent asymmetry for the case of direct CP violation in the $D^0 - \overline{D^0}$ system is found here to be:

$$A = 0.20 \pm 0.15$$

or

$$A \leq 0.45$$

at the 90% confidence level. Although not very stringent, this result is the first such on CP violation in the D system. The greatest problem in determining such a quantity is the lack of statistics, making precise (*i.e.* low σ/N) measurements of signal strengths difficult, even with very little background. It is hoped that future, or even present, experiments will be able to provide charm in sufficient quantity to alleviate this condition. Included in the above are fixed-target γ- and/or hadro-production charm experiments (such as E791 at Fermilab). Another possibility are collider-detectors operating at e^+e^- Υ machines, where charm is copiously produced.

Appendix A Decay Rate Calculations

Included in section 1.2.1 of the first chapter were expressions for rates for the decays $D^0 \to f$ and $\overline{D^0} \to f$. This result can be obtained from the time evolution functions for the weak states $|\psi\rangle$ and $|\overline{\psi}\rangle$ fairly easily. As a reminder:

$$|\psi(t)\rangle = a(t)|D^0\rangle + b(t)|\overline{D^0}\rangle$$

$$|\overline{\psi}(t)\rangle = \overline{a}(t)|D^0\rangle + \overline{b}(t)|\overline{D^0}\rangle$$

where

$$a(t) = e^{im_\alpha t - \gamma_\alpha t/2} + e^{im_\beta t - \gamma_\beta t/2}$$

$$\overline{a}(t) = e^{im_\alpha t - \gamma_\alpha t/2} - e^{im_\beta t - \gamma_\beta t/2}$$

$$b(t) = \frac{1-\delta}{1+\delta}[-e^{im_\alpha t - \gamma_\alpha t/2} + e^{im_\beta t - \gamma_\beta t/2}]$$

$$\overline{b}(t) = \frac{1-\delta}{1+\delta}[-e^{im_\alpha t - \gamma_\alpha t/2} - e^{im_\beta t - \gamma_\beta t/2}].$$

The decay rates to be obtained are again given as:

$$Rate(D^0 \to f) \propto e^{-\Gamma t}[(1+\cos(\Delta m t)|A|^2 + (1-\cos(\Delta m t)|\phi|^2|\overline{A}|^2 - 2\sin(\Delta m t)\mathrm{Im}(\phi\overline{A}A^*)]$$

and

$$Rate(\overline{D^0} \to f) \propto e^{-\Gamma t}[(1+\cos(\Delta m t)|\overline{A}|^2 + (1-\cos(\Delta m t)|\phi|^2|A|^2 + 2\sin(\Delta m t)\mathrm{Im}(\phi\overline{A}A^*)]$$

where

$$\frac{1-\delta}{1+\delta} \equiv \phi$$

In order to calculate the rate for the decay $D^0 \to f$, the following quantity must be calculated:

$$|\langle f|\psi\rangle|^2$$

Denoting the amplitudes $\langle f|D^0\rangle = A$ and $\langle f|\overline{D^0}\rangle = \overline{A}$, this becomes:

$$|\langle f|\psi\rangle|^2 = |(Aa) + (\overline{A}b)|^2 =$$

$$((A^*a^*) + (\overline{A}^*b^*)) \times ((Aa) + (\overline{A}b)) =$$

$$|A|^2|a|^2 + \overline{A}^*Ab^*a + A^*\overline{A}a^*b + |\overline{A}|^2|b|^2.$$

It is worth noting that Aa is the amplitude for the direct decay $D^0 \to f$, whereas $\overline{A}b$ is the amplitude for decay with mixing $D^0 \to \overline{D^0} \to f$. It is the quantum interference of these two amplitudes which is responsible for the non-exponential behavior evidenced in the decay rates. There are thus four terms in this expression to be calculated. Starting at the left-hand side, one has:

$$|A|^2|a|^2 = |A|^2a^*a =$$

$$|A|^2\{(e^{-im_\alpha t-\gamma_\alpha t/2} + e^{-im_\beta t-\gamma_\beta t/2}) \times (e^{im_\alpha t-\gamma_\alpha t/2} + e^{im_\beta t-\gamma_\beta t/2})\} =$$

$$|A|^2\{e^{-\gamma_\alpha t} + e^{-i\Delta mt-\overline{\Gamma}t} + e^{i\Delta mt-\overline{\Gamma}t} + e^{-\gamma_\beta t}\} =$$

$$|A|^2\{e^{-\gamma_\alpha t} + 2e^{-\overline{\Gamma}t}\cos(\Delta mt) + e^{-\gamma_\beta t}\}$$

where $\overline{\Gamma} = (\gamma_\alpha + \gamma_\beta)/2$. If one assumes that $\Delta\Gamma = 0$, then $\gamma_\alpha = \gamma_\beta = \Gamma$ and $\overline{\Gamma} = \Gamma$. Thus:

$$|A|^2|a|^2 = |A|^2a^*a =$$

$$2|A|^2e^{-\Gamma t}\{1 + \cos(\Delta mt)\}$$

The fourth term becomes, with the previous assumptions:

$$|\overline{A}|^2|b|^2 = |\overline{A}|^2b^*b =$$

$$|\overline{A}|^2\phi^*\phi\{(-e^{-im_\alpha t-\gamma_\alpha t/2}+e^{-im_\beta t-\gamma_\beta t/2})\times(-e^{im_\alpha t-\gamma_\alpha t/2}+e^{im_\beta t-\gamma_\beta t/2})\}=$$

$$|\overline{A}|^2|\phi|^2\{e^{-\gamma_\alpha t}-e^{-i\Delta mt-\overline{\Gamma}t}-e^{i\Delta mt-\overline{\Gamma}t}+e^{-\gamma_\beta t}\}=$$

$$|\overline{A}|^2|\phi|^2\{e^{-\gamma_\alpha t}-2e^{-\overline{\Gamma}t}\cos(\Delta mt)+e^{-\gamma_\beta t}\}=$$

$$2|\phi|^2|\overline{A}|^2e^{-\Gamma t}\{1-\cos(\Delta mt)\}$$

The second term can now be dealt with:

$$\overline{A}^*Ab^*a=$$

$$\overline{A}^*A\phi^*\{(-e^{-im_\alpha t-\gamma_\alpha t/2}+e^{-im_\beta t-\gamma_\beta t/2})\times(e^{im_\alpha t-\gamma_\alpha t/2}+e^{im_\beta t-\gamma_\beta t/2})\}=$$

$$\overline{A}^*A\phi^*\{-e^{-\gamma_\alpha t}-e^{-i\Delta mt-\overline{\Gamma}t}+e^{i\Delta mt-\overline{\Gamma}t}+e^{-\gamma_\beta t}\}=$$

$$\overline{A}^*A\phi^*\{-e^{-\gamma_\alpha t}-e^{-\Gamma t}2i\sin(\Delta mt)+e^{-\gamma_\beta t}\}=$$

$$\overline{A}^*A\phi^*\{e^{-\Gamma t}2i\sin(\Delta mt)\}$$

since $\Delta\Gamma=0$. Similarly, the third term is:

$$A^*\overline{A}a^*b=$$

$$A^*\overline{A}\phi\{(e^{-im_\alpha t-\gamma_\alpha t/2}+e^{-im_\beta t-\gamma_\beta t/2}\times(-e^{im_\alpha t-\gamma_\alpha t/2}+e^{im_\beta t-\gamma_\beta t/2})\}=$$

$$A^*\overline{A}\phi\{-e^{-\gamma_\alpha t}+e^{-i\Delta mt-\overline{\Gamma}t}-e^{i\Delta mt-\overline{\Gamma}t}+e^{-\gamma_\beta t}\}=$$

$$A^*\overline{A}\phi\{-e^{-\Gamma t}2i\sin(\Delta mt)\}$$

The sum of the second and third terms is thus:

$$\text{term\#1}+\text{term\#2}=$$

$$\{\overline{A}^*A\phi^*+A^*\overline{A}\phi\}(e^{-\gamma_\alpha t}-e^{-\gamma_\beta t})+2ie^{-\Gamma t}\sin(\Delta mt)\{\overline{A}^*A\phi^*-A^*\overline{A}\phi\}=$$

$$-4e^{-\Gamma t}\sin(\Delta mt)\,\mathrm{Im}(A^*\overline{A}\phi).$$

Summing the four terms yields:

$$\Sigma\text{AllTerms} =$$

$$2|A|^2 e^{-\Gamma t}\{1+\cos(\Delta m t)\} + 2|\phi|^2|\overline{A}|^2 e^{-\Gamma t}\{1-\cos(\Delta m t)\}$$
$$-4e^{-\Gamma t}\sin(\Delta m t)\,\mathrm{Im}(A^*\overline{A}\phi)$$

Factoring out the exponential, this leaves:

$$2e^{-\Gamma t}\{(1+\cos(\Delta m t))|A|^2 + (1-\cos(\Delta m t))|\phi|^2|\overline{A}|^2$$
$$-2\sin(\Delta m t)\,\mathrm{Im}(A^*\overline{A}\phi)\}$$

which is seen to be the functional form of the rate, up to a factor of two, for the decay $D^0 \to f$. The rate for the decay $\overline{D^0} \to f$ is obtained in an analogous manner.

Bibliography

[1] R. Rückl, "Weak Decays of Heavy Mesons", Proc. XXII int. Conf. on High Energy Physics, Leipzig, ed. by A. Meyer and E. Wieczorek (Akad. der Wissenschaften der DDR, Institut für Hochenergiephysik, Zeuthen, GDR, 1984), p. 135.

[2] Particle Data Group, "Review of Particle Properties", Phys. Lett. B, **170**, 1986.

[3] A. J. Buras, J. M. Gérard and R. Rückl, "1/N Expansion for Exclusive and Inclusive Charm Decays", Nucl. Phys. B **268**, 1986, p.16.

[4] M. Bauer, B. Stech and M. Wirbel, "Exclusive Non-Leptonic Decays of D-, D_s- and B-Mesons", Z. Phys. C, **34**, 1987, p.103.

[5] M. Bauer and B. Stech, "Exclusive D-Decays", Phys. Lett. B, **152**, 1985, p.380.

[6] K. Terasaki and S. Oneida, "Solution to the Puzzle of $\Gamma(D^0 \to K^-K^+)/\Gamma(D^0 \to \pi^-\pi^+)$ in a unified approach to $D \to \pi\overline{K}$, $K\overline{K}$, and $\pi\pi$ and $K \to \pi\pi$ Decays", Phys. Rev. D, **38**, 1988, p.132.

[7] MARK II collaboration, G. S. Abrams *et al.*, Phys. Rev. Lett., **43**, 1979, p. 481.

[8] MARK III collaboration, R.M. Baltrusaitis *et al.*, Phys. Rev. Lett., **55**, 1985.

[9] L. L. Chau, "Quark Mixing in Weak Interactions", Phys. Rep., **95**, 1983, p.1.

[10] I. I. Bigi, "$D^0 - \overline{D^0}$ Mixing and CP Violation in D Decays - Can There Be High Impact Physics in Charm Decays?", in Proceedings of the Tau-Charm Factory Workshop, Stanford, May 23-27, 1989, SLAC Report 343, p. 169.

[11] I. I. Bigi, "On the Prospects of Observing CP Violation in Bottom and Charm Decays", in Proceedings of the XXIII International Conference on High Energy Physics, Berkeley, July 1986, S. Loken (ed.), World Scientific, Vol. II, p. 857.

[12] I. I. Bigi and A. I. Sanda, "CP VIolation in Heavy Flavor Decays: Predictions and Search Strategies", Nucl. Phys. B, **281**, 1987, p.41.

[13] L. Wolfenstein, "$D^0 - \overline{D^0}$ Mixing", Phys. Lett. B, **164**, 1985, p.170.

[14] L. Wolfenstein, "Final-State Interactions and CP Violation in Weak Decays", Phys. Rev. D, **43**, 1991, p.151.

[15] J. F. Donoghue *et al.*, "Dispersive Effects in $D^0 - \overline{D^0}$ Mixing", Phys. Rev. D, **33**, 1985, p.179.

[16] E691 collaboration, J. C. Anjos *et al.*, "Study of $D^0 - \overline{D^0}$ Mixing", Phys. Rev. Lett., **60**, 1988, p. 1239.

[17] A. Datta and D. Kumbhakar, "$D^0 - \overline{D^0}$ Mixing: A Possible Test of Physics Beyond the Standard Model", Z. Phys. C., **27**, 1985, p.515.

[18] S. Holmes, W. Lee, J. Wiss, "High Energy Photoproduction of Charmed States"; Ann. Rev. Nucl. Part. Sci., **35**, 1985, p.397.

[19] L.M. Jones and H.W. Wyld, Phys. Rev. D, **17**, 1978, p. 759. M.A. Shifman, A.I. Vainstein and V.I. Zakharov, Phys. Lett. B, **65**, 1976, p.255.

[20] J. Raab, "Lifetime Measurements of the Three Pseudoscalar D-Mesons", Ph.D. Thesis, UC Santa Barbara, 1987.

[21] T. Browder, "A Study of $D^0 - \overline{D^0}$ Mixing", Ph.D. Thesis, UC Santa Barbara, 1988.

[22] M. C. Gibney, "Photoproduction of Charmed Baryons", Ph.D. Thesis, University of Colorado at Boulder, 1989.

[23] P. Jarron and M. Goyot, Nucl. Inst. Meth., **226**, 1980, p. 156.

[24] D. Summers, "Reconstruction of a Strip Geometry Calorimeter using Stepwise Regression", Nucl. Inst. Meth., **228**, 1985, p.290.

[25] D. Bartlett *et al.*, "Performance of the Cherenkov Counters in the Fermilab Tagged Photon Spectrometer Facility", Nucl. Inst. Meth., **A260**, 1987, p. 55.

[26] S. Petrera and G. Romano, "A Method to Evaluate the Detection Efficiency and the Mean Lifetime of Short Lived Particles", Nucl. Inst. Meth., **174**, 1980, p. 61.

[27] T. Sjöstrand, "The Lund Monte Carlo for Jet Fragmentation and e^+e^- Physics- JETSET version 6.2", LU TP 85-10, University of Lund, Sölvegatan 14A, S-223 62, Lund, Sweden.

[28] S. Menary, "A Study of the Transverse Momentum Distributions of Photo-produced Charged and Neutral D Mesons", Master's thesis, University of Toronto, 1986.

[29] M. D. Sokoloff, private communication.

[30] E691 collaboration, J. C. Anjos *et al.*, "Charm Photoproduction", Phys. Rev. Lett., **62**, 1989, p. 513.

[31] CLEO collaboration. J. Alexander *et al.*, Phys. Rev. Lett., **65**, 1990, p. 1184.

[32] ARGUS collaboration, H. Albrecht *et al.*, Z. Phys. C, **C 46**, 1990, p. 9.

[33] J.C. Anjos *et al.*, "Measurement of the Decays $D^0 \rightarrow \pi^-\pi^+$ and $D^0 \rightarrow K^-K^+$", to be published as a Rapid Communication in Phys. Rev. D.